NASA Contractor Report 4472

Microcracking, Microcrack-Induced Delamination, and Longitudinal Splitting of Advanced Composite Structures

John A. Nairn
University of Utah
Salt Lake City, Utah

Prepared for
Langley Research Center
under Contract NAS1-18833

National Aeronautics and
Space Administration
Office of Management
Scientific and Technical
Information Program
1992

Contents

Chapter 1

SUMMARY

Composites are often treated as "materials," but it is perhaps more realistic to treat them as "engineered structures." Unlike conventional materials, which on some relatively small scale are homogeneous bodies, composite structures are heterogeneous bodies. For advanced, aerospace composites, which are comprised of fibers and a matrix, the heterogeneous nature is revealed by observations on the scale of a fiber diameter—8 μm. Such heterogeneity has numerous consequences. First, the mechanical properties of composite structures are generally anisotropic. This anisotropy complicates any detailed stress analysis of composites. Second, and perhaps more importantly, heterogeneity leads to a variety of failure modes. Some examples include fiber fracture, matrix fracture, interfacial failure, delamination, and *intralaminar* fracture. Because of the variety of failure modes, the analysis and prediction of composite failure is a difficult and multifaceted problem. The theme of this research project, as indicated by the title, was to develop new methods for characterizing the fracture toughness of advanced composite structures. The new methods were used to study microcracking, microcrack-induced delamination, and longitudinal splitting of polymeric matrix composites.

We view the analysis of each composite failure mode (fiber fracture, matrix fracture, *etc.*) as a separate fracture mechanics problem. In this research project we approached each failure mode with a five step micromechanics of damage analysis. Those five steps are:

1. Observe the damage process
2. Analyze the stresses in a damaged laminate
3. Propose failure criteria and make predictions
4. Verify the analysis with experiments
5. Use the analysis to study or design composite structures.

The first step is to determine the type of damage observed in representative composite laminates. This step should be obvious but, surprisingly, is skipped by many investigators. The goal of this step is to understand what type of cracks form, where the cracks form, and what causes them to form. Some typical questions to ask are: Is the damage matrix cracking, fiber breakage, interfacial debonding, or ply delamination? How is the damage process affected by laminate structure and material properties? It is necessary to obtain a large data base of experimental observations before it is possible to develop a meaningful analysis of any particular composite failure mode.

The second step is to undertake a stress analysis in the presence of damage. If the first step was done correctly the stress analysis will be carried out for stress and strain distributions in the presence of the observed damage. Unlike isotropic, homogeneous materials for which it is often possible to obtain exact linear elastic solutions, analysis of stresses in composites almost always requires approximate stress analyses. The key to a successful failure analysis is the development of a mechanics model that leads to a sufficiently accurate stress analysis. For very complex problems involving complex damage states or significant three-dimensional effects, it may be necessary to turn to numerical stress analyses such as finite element analysis. The overuse of numerical analysis, however, tends to limit practical utility, limit model generality without additional costly numerical calculations, and limit physical insights gained from closed form, but approximate stress analyses.

Armed with information about the effect of observed damage on the stresses, the third step is to postulate failure criteria and predict initiation and growth of damage. Failure criteria are usually maximum stress or strain criteria, or fracture mechanics criteria such as stress intensity factor or strain energy release rate. An important feature, often missed in criticism of the literature, is that steps two and three are totally independent. Any available stress analysis can be used with any failure criterion. If experimental results reveal that a particular model for micromechanics of damage is inadequate, it may be the result of the inadequacy of only one step. For example, a good stress analysis coupled with an inappropriate failure criterion will give poor results as will an over simplified stress analysis coupled with a good failure criterion.

Step four is to compare the predictions of steps two and three to the experimental observations in step one. A good micromechanics of damage analysis is defined as one that correlates and explains most or all of the experimental observations.

Step five is the application phase. Once a micromechanics of damage analysis for any particular composite failure mode has been proposed and verified, it becomes available for use. It can be used to characterize the toughness of various composites and thereby rank them according that failure mode. To completely characterize the toughness of a composite, however, one must study many failure modes and not just one failure mode such as delamination. The toughest composite will generally be the one with the best overall balance of properties. Besides ranking materials, failure analysis models can be used to design composite structures. The can be used to avoid damage, to predict the effect of damage, and to predict fatigue lifetimes.

The first form of failure in composites which have off-axis plies is matrix fracture or matrix microcracking in those off-axis plies. Although matrix microcracking has been studied since the 1970's, we found that as of 1988 (the start of this contract), no microcracking theory could explain all microcracking results. Chapter 1 describes a new analysis of microcracking developed during this contract. That chapter begins with a review of the stress analysis techniques used to study microcracking. We concluded that Hashin's [1–4] variational analysis is the best stress analysis method. Before we could use his analysis to study microcracking, however, we had to extend to include thermal stresses [5–7], to include general cross-ply stacking sequences [8, 9], and to account for antisymmetric damage states observed when the microcracking plies are on the free-surface of the laminate [10]. We assumed that microcracking occurs when the energy release rate due to the formation of the microcrack exceeds the microcracking toughness, G_{mc}, of that composite material. The best way to verify the stress analysis and the energy release rate failure criterion is to compare the predictions to experimental results using a master plot approach. We found that the new analysis can correlate our large body of new experimental data. We also derived master plot analyses for previous microcracking models. We found that many models previously believed to be qualitatively correct are, in fact, complete failures. Our new microcracking model is unique in its ability to explain experimental observations. Chapter 1 closes with an application phase of composite failure analysis by comparing the microcracking toughness of a variety of composite materials.

The success of the variational analysis and the energy release rate failure criterion described in Chapter 1, led us to consider additional failure problems. In Chapter 2, we use the energy release rate calculation to derive a modified Paris-Law for microcracking fatigue experiments. By plotting the microcrack density growth rate as a function of energy release rate amplitude, ΔG_m, we were able to correlate experimental data from a many different laminates of one composite material system an a single master plot. The fatigue characterization worked for both for mechanical fatigue and thermal cycling fatigue.

An important detrimental effect of microcracks is that they can nucleate further forms of damage such as delaminations. In Chapter 3, we describe an extension of the variational analysis to account for delaminations emanating from the microcrack tips [9]. The analysis was used to make several predictions about the process of microcrack induced delaminations. All predictions agree well with available experimental observations.

Chapter 4 is an abstract chapter that discusses ways in which the variational stress analysis techniques can be generalized to handle new fracture problems. In particular we discuss an analysis of curved microcracks, a completely general variational analysis of composite plates, and a variational analysis of stresses around breaks in single embedded fibers. The discussion in Chapter 4 suggests many possibilities for future work.

Another matrix failure mode is longitudinal splitting. Longitudinal splitting is usually defined as *intralaminar* crack propagation parallel to the fibers in unidirectional composites. Longitudinal splitting can also be observed in 0° plies of multi-axial laminates. Chapter 5 discusses a new analysis of longitudinal splitting in unidirectional composites. We found that many experimental results are influenced by fibers bridging across the longitudinal split. If the experimental observation of fiber bridging is ignored, it is easy to misinterpret composite fracture tests and thereby incorrectly characterize the longitudinal splitting fracture toughness. We developed new ways to account for fiber bridging and clarified the definition of *true* fracture toughness for *intralaminar* crack propagation.

In this research project, we worked on micromechanics of damage analyses for various failure modes including microcracking, delamination, and longitudinal splitting. In the process, we arrived at two litmus tests that can be used to judge our own or anyone else's failure analysis models:

1. The stress analysis must be realistic and sufficiently accurate.

2. The failure criterion must be realistic and rooted in fracture mechanics.

The first litmus test considers the stress analysis in the presence of damage. Most people would agree that unless the stress analysis is accurate, the fracture predictions cannot be accurate. A more subtle point is that the requirements of a stress analysis for fracture predictions is more severe than the requirements of a stress analysis for other properties. Fracture should be viewed as an instability event. As such, the predictions can be very sensitive to small differences in stress analyses. Other laminate properties such as stiffness, plates displacements, thermal expansion coefficients, *etc.*, are not instability events, but rather global plate properties. It is much easier to derive a stress analysis to predict global properties than it is to derive one to predict instability events. In the microcracking analysis, for example, we found that approximate stress analyses based on shear-lag approximations do a good job at predicting plate stiffness and in-plane displacements, but a very poor job at predicting fracture. Before we were able to derive an acceptable microcracking model, we had to use improved stress analysis methods. When evaluating literature fracture models, the stress analysis parts of those models should always be questioned. No stress analysis should be accepted unless it can be demonstrated that it can be used in conjunction with failure criteria to predict *fracture* properties.

The second litmus test involves the failure criterion. There is a disturbing tendency of composite failure models to concentrate of sophisticated stress analyses, damage mechanics, or finite element analyses, while giving too little thought to choosing an appropriate failure criterion. As a result, one often finds complex failure models that are based on simplistic failure criteria such as maximum stress, maximum strain, average stress, point stress, or quadratic stress functions. We found that such simplistic failure criteria could not explain our experimental observations. In all our analyses we turned instead to fracture mechanics and predicted failure in terms of energy release rate for crack propagation. The failure modes we studied are not unique in being controlled by energy release rate. We suggest that fracture mechanics is a fundamental tool for predicting failure and should be used for all composite failure modes.

A good way to judge the failure criterion in a composite failure model is to imagine applying the model to an isotropic, homogeneous material. After all, isotropic, homogeneous materials are a special case of a composite material in which the fiber and matrix have identical properties and the interface is perfect. If a failure model cannot handle the simple special case of an isotropic, homogeneous material, then it should not be expected to be realistic for more complex cases (*e.g.* composites). For example consider crack propagation from a notch. No one would consider using maximum stress, maximum strain, average stress, point stress, or quadratic stress functions to predict the conditions that lead to crack propagation in isotropic, homogeneous materials. Likewise, no one should propose a composite failure model based in these unrealistic failure criteria. We recommend that all serious composite failure models should make use of the principles of fracture mechanics.

Chapter 2

MICROCRACKING UNDER STATIC LOADS

2.1 Introduction

Many observations have confirmed that the first form of damage in general angle-ply laminates loaded in tension is matrix cracking or microcracking in the off-axis plies [6, 10–47]. Microcracks are readily observed in 90° plies in which they are logically termed transverse cracks. Even if 90° plies are not present, however, microcracks can still form in the plies with the highest angle with respect to the loading direction (*e.g.* the θ plies in a $[0/\theta/-\theta]_s$ laminate [48]). Microcracks may be observed during static loading, fatigue loading, thermal loading, or any combination of these loadings.

The initial effects of a few microcracks in 90° plies are relatively minor. Microcracks cause changes in mechanical properties of the laminate including a reduction in longitudinal stiffness [23] and a change in thermal expansion coefficients [49, 50]. Microcracks introduce pathways through which corrosive agents can penetrate into the interior of the laminate. The mere presence of microcracks and the above minor effects may cause a technical failure [17]. If small changes in mechanical properties cannot be tolerated or if leakage is crucial (e.g. for pressure vessels), the presence of the first microcrack causes structural failure. For these critical applications the microcracking analysis must be able to predict the initiation of microcracking.

Many composite applications are not affected by a few microcracks and it is tempting to consider microcracking damage to be tolerable as long as the microcrack density is low. Unfortunately there is much evidence suggesting that microcracks act as nuclei for further and potentially more deleterious forms of damage [17]. Microcracks can promote delamination between the off-axis ply (*e.g.* the 90° ply) and the adjacent ply. These delaminations initiate along the line where the edge of the microcrack meets the ply interface. When 0° plies are adjacent to 90° plies, the microcrack can induce longitudinal splitting in the 0° plies. The intersection of the microcrack and the longitudinal split is an area of intense stress concentration that can cause delamination [34]. At late stages of microcracking damage, curved or oblique microcracks may appear near existing straight microcracks [34]. Delamination appears to proceed easily from the tips of curved microcracks [34]. Matrix microcracks in 90° plies and the types of damage induced by matrix microcracks are shown in Fig. 2.1. A successful microcracking analysis should be capable of predicting not only microcracking, but also the nucleation of other forms of damage.

This chapter describes a new analysis of microcracking in the 90° plies of $[90_n/(S)]_s$ and $[(S)/90_n]_s$ laminates where (S) is any orthotropic supporting sublaminate. We can list some goals or objectives for a successful analysis:

1. Predict microcrack initiation.
2. Predict the increase in density of microcracks on continued loading.
3. Predict the conditions that lead to related forms of damage such as delamination, longitudinal splitting, and curved microcracks.

90° plies in $[90_n/(S)]_s$ laminates [10], and to handle delaminations emanating from microcrack tips [9]. The second step was to use the new stress analyses to predict failure. We assumed that microcracks from when the total energy release rate associated with their formation exceeds some critical value or microcracking toughness of the composite materials system.

This chapter begins by reviewing microcracking stress analysis techniques that have appeared in the literature. We give reasons for believing that the variational analysis is currently the best analysis and therefore the preferred analysis for any analysis of microcracking. We next discuss various microcracking failure criterion and show that the energy release rate criterion does the best job of correlating all experimental data. The best way to evaluate microcracking theories is to construct a master plot that can be used to compare predictions of those theories. The master plot section of this chapter shows that the energy release rate criterion coupled with the the variational stress analysis is the only one capable of predicting all experimental results. A surprising finding is that previous literature theories that many people believe to be at least qualitatively correct are better characterized as complete failures. This chapter closes with a discussion of the microcracking toughness of various composite materials.

2.2 Stress Analysis

The first step in any microcracking analysis is to obtain the stress state for laminates with microcracks in the 90° plies. For now we ignore other damage modes, such as delamination and curved microcracks. They will be considered in later chapters. The laminate coordinate system is defined in Fig. 2.2. The x direction is the loading direction; the y direction is the width direction; the z direction is the thickness direction. The sample length (L), width (W), and thickness (B) are also shown in Fig. 2.2.

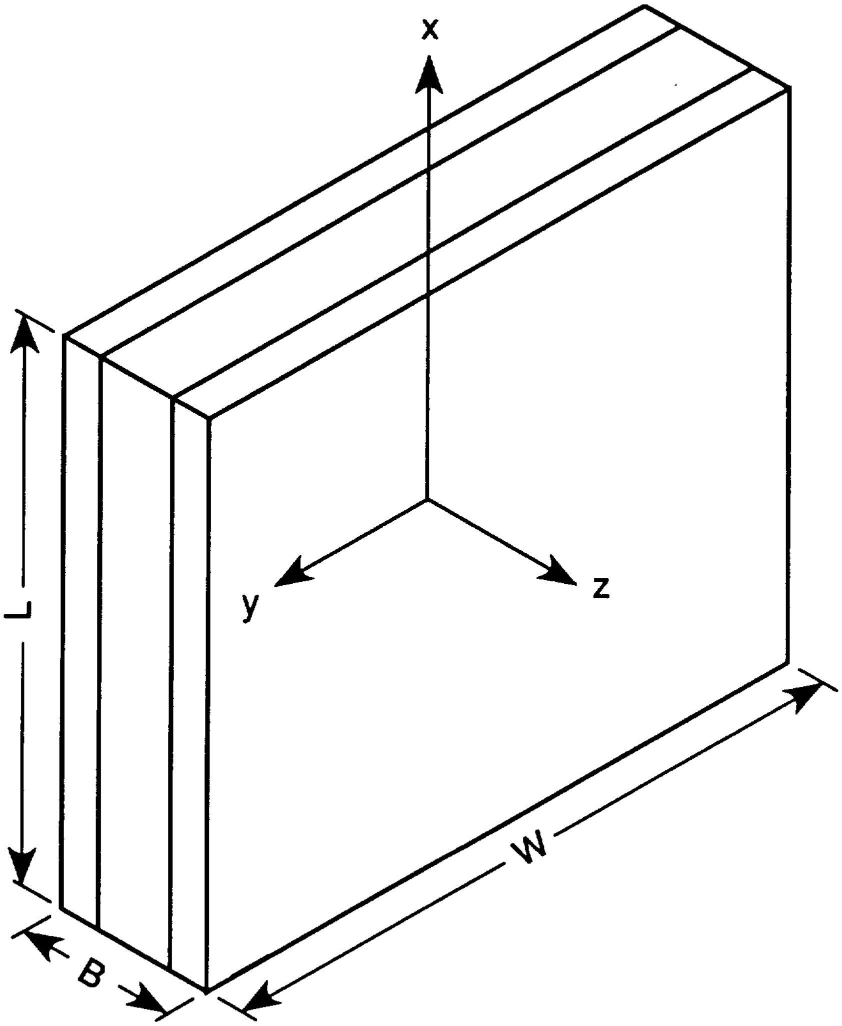

Figure 2.2: The coordinate system for the stress analysis of $[(S)/90_n]_s$ and $[90_n/(S)]_s$ laminates. L, W, and B are the length, width, and thickness of the laminate plate.

[illegible] 19

PAGE INTENTIONAL

PAGE 19 INTENTIONALLY BLANK

2.2.1 Statement of the Problem

We define a component of the stress tensor by $\sigma_{jk}^{(i)}$ where j and k are x, y, or z and superscript (i) denotes the ply group ($i = 1$ for the 90° ply group and $i = 2$ for the (S) sublaminate). In the $x - z$ plane of an undamaged laminate, only $\sigma_{xx}^{(i)}$ is non-zero. Defining $\sigma_{x0}^{(i)}$ as the initial x-axis stress in ply group i, the stresses in the undamaged laminate are

$$\sigma_{xx}^{(i)} = \sigma_{x0}^{(i)} \qquad \sigma_{zz}^{(i)} = \sigma_{xz}^{(i)} = 0 \tag{2.1}$$

Because microcracking occurs at very low strains, a linear thermoelastic analysis is appropriate. Linearity allows us to rewrite the initial stresses as

$$\sigma_{x0}^{(i)} = k_m^{(i)}\sigma_0 + k_{th}^{(i)}T \tag{2.2}$$

where σ_0 is the total applied stress in the x direction and $T = T_s - T_0$ is the difference between the specimen temperature, T_s, and the stress free temperature, T_0. $k_m^{(i)}$ and $k_{th}^{(i)}$ are mechanical and thermal stiffnesses for ply group i.

There are some minor differences in the various microcracking analyses regarding the evaluation of $k_m^{(i)}$ and $k_{th}^{(i)}$. If the third dimension (the y dimension) is ignored, the stress state of an undamaged laminate reduces to a one-dimensional problem. Assuming that the x-direction displacements of all ply groups are identical, one quickly derives

$$\begin{aligned} k_m^{(1)} &= \frac{E_x^{(1)}}{E_c^0} & \qquad k_m^{(2)} &= \frac{E_x^{(2)}}{E_c^0} \\ k_{th}^{(1)} &= -\frac{\Delta\alpha}{C_1} & \qquad k_{th}^{(2)} &= \frac{\Delta\alpha}{\lambda C_1} \end{aligned} \tag{2.3}$$

where $E_x^{(i)}$ is the x-direction Young's modulus of ply group i,

$$E_c^0 = \frac{t_1 E_x^{(1)} + t_2 E_x^{(2)}}{t_1 + t_2} \tag{2.4}$$

is the rule-of-mixtures x-direction modulus of the undamaged laminate, $\Delta\alpha = \alpha_x^{(1)} - \alpha_x^{(2)}$ is the difference between the x-direction thermal expansion coefficients of the two ply groups,

$$C_1 = \frac{1}{E_x^{(1)}} + \frac{1}{\lambda E_x^{(2)}} \tag{2.5}$$

and $\lambda = \frac{t_2}{t_1}$.

Alternatively, one may analyze the undamaged laminate using laminated plate theory [51]. The mechanical load and thermal stiffnesses obtained either by simple one-dimensional analysis or by laminated plate theory are identical if the Poisson ratios, $\nu_{xy}^{(i)}$, are set equal to zero. Therefore, for laminates under unidirectional tension, laminated plate theory is a correction of the one-dimensional analysis to account for transverse Poisson's contraction. In cross-ply laminates, the correction is generally small. For a homologous series of $[0/90_n]_s$ laminates with $n = \frac{1}{2}$ to 8, the Poisson correction to $k_m^{(i)}$ is always less than 2% and the Poisson correction to $k_{th}^{(i)}$ is always less than 6.5%. Because these correction factors are small, we regard consideration of Poisson's contraction as an insignificant aspect or any microcracking analysis. In other words, if the only feature distinguishing two analyses is the inclusion of Poisson's contraction we regard those analyses as identical.

When microcracks form in an undamaged laminate, the stresses change. In general all stress components, $\sigma_{xx}^{(i)}$, $\sigma_{xz}^{(i)}$, and $\sigma_{zz}^{(i)}$, become non-zero. In terms of boundary conditions, it is normally assumed that microcrack surfaces are stress free. Thus the normal and shear stresses in the 90° plies are zero on the microcrack surfaces. The load no longer carried by the 90° plies is transferred to the adjacent unbroken plies. For $[(S)/90_n]_s$ laminates these requirements and symmetry in shear stresses lead to the following boundary conditions

$$\left\langle \sigma_{xx}^{(2)}(\pm a) \right\rangle = \sigma_{x0}^{(2)} + \frac{\sigma_{x0}^{(1)}}{\lambda} \tag{2.6}$$

$$\sigma_{xx}^{(1)}(\pm a) = 0 \tag{2.7}$$

$$\sigma_{xz}^{(1)}(\pm a) = \sigma_{xz}^{(2)}(\pm a) = 0 \tag{2.8}$$

where $\left\langle \sigma_{xx}^{(2)}(x) \right\rangle$ is the average x-direction stress in the (S) sublaminate at position x. In the

22 INTENTIONALLY BLANK

PAGE 23 INTENTIONALLY BLANK

Equation (2.11) is easily solved to give

$$\Delta\sigma = -\frac{\omega}{\phi^2} + \left(\frac{\sigma_{x0}^{(1)}}{\lambda} + \frac{\omega}{\phi^2}\right)\frac{\cosh\phi\xi}{\cosh\phi\rho} \tag{2.13}$$

The average stress in the (S) sublaminate is

$$\left\langle\sigma_{xx}^{(2)}\right\rangle = \sigma_{x0}^{(2)} - \frac{\omega}{\phi^2} + \left(\frac{\sigma_{x0}^{(1)}}{\lambda} + \frac{\omega}{\phi^2}\right)\frac{\cosh\phi\xi}{\cosh\phi\rho} \tag{2.14}$$

By force balance, the average stress in the 90° plies is

$$\left\langle\sigma_{xx}^{(1)}\right\rangle = \left(\sigma_{x0}^{(1)} + \frac{\lambda\omega}{\phi^2}\right)\left(1 - \frac{\cosh\phi\xi}{\cosh\phi\rho}\right) \tag{2.15}$$

Integrating the equations of equilibrium, the load transfer from the 90° plies to the (S) sublaminate by shear at the interface is described by

$$\frac{d\Delta\sigma}{d\xi} = \frac{\tau_i}{\lambda} \tag{2.16}$$

where τ_i is the interfacial shear stress [12]. With the aid Eqs. (2.13) and (2.16), the one-dimensional analyses give the interfacial shear stress as

$$\tau_i = \phi\left(\sigma_{x0}^{(1)} + \frac{\lambda\omega}{\phi^2}\right)\frac{\sinh\phi\xi}{\cosh\phi\rho} \tag{2.17}$$

The average x-direction tensile stress in the 90° plies and the interfacial shear stress derived from the one-dimensional analysis are plotted in Fig. 2.5. The plots are for a $[0/90_2]_s$ carbon/epoxy laminate. As required by boundary conditions, $\sigma_{xx}^{(1)}$ is zero on the microcrack surfaces. Away from the microcrack, $\sigma_{xx}^{(1)}$ increases as stress is transferred from the (S) sublaminate back into the 90° plies. The shear stress has a maximum at the microcrack surfaces and decays towards zero. The non-zero shear stress on the microcrack surfaces is a violation of boundary conditions and a deficiency of all one-dimensional analyses.

Having solved the general one dimensional analysis equation (Eq. (2.11)), the only things that distinguishes the numerous one-dimensional theories are the procedures used to evaluate ϕ and

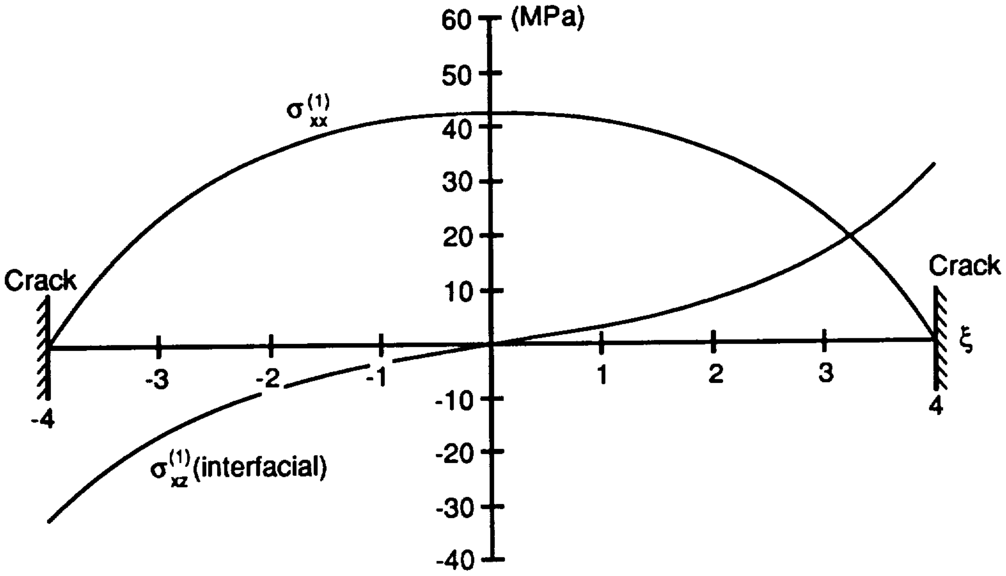

Figure 2.5: Stresses between two microcracks in a $[0/90_2]_s$ carbon/epoxy laminate from a one-dimensional analysis. The applied stress is 100 MPa, thermal load is $T = -125°\mathrm{C}$, and the microcrack spacing is $\rho = 4$. The normal stress ($\sigma^{(1)}_{xx}$) is the average tensile stress in the 90° ply group. The plotted shear stress ($\sigma^{(1)}_{xz}$) is the shear stress at the 90/0 interface

ω. Garrett and Bailey *et. al.* [12, 16] described the first one-dimensional analysis. They used shear-lag approximations and assumed that the displacement in the 90° plies is a function of x but is independent of z. They found

$$\phi^2 = G^{(1)}_{xz} C_1 \qquad \text{and} \qquad \omega = 0 \tag{2.18}$$

where $G^{(1)}_{xz}$ is the shear modulus of the 90° plies in the $x-z$ plane and C_1 is defined in Eq. (2.5). We show later that this first calculation of ϕ^2 is nearly optimal for calculating the effect of microcracks on longitudinal laminate modulus. We note that Garrett and Bailey [12] only solved for stresses around an isolated microcrack. For an isolated microcrack solution, we simply place the microcrack at the origin and solve Eq. (2.11) with new boundary conditions

$$\Delta\sigma(0) = \frac{\sigma^{(1)}_{x0}}{\lambda} \qquad \text{and} \qquad \Delta\sigma(\infty) = 0 \tag{2.19}$$

Manders *et. al.* [21] repeated Garrett and Bailey's analysis [12] with the same value of ϕ^2 and ω but extended it to account for neighboring microcracks.

PAGE 26 INTENTIONALLY BLANK

analysis with a minor correction for Poisson contraction. If we set $\nu_{xy}^{(i)}$ to zero, ϕ^2 reduces to

$$\phi^2 = \frac{C_1}{C_4} \tag{2.27}$$

which differs only by a numerical prefactor from the reduced Flaggs' result (see Eq. (2.23)). The fact that Nuismer and Tan's [57] analysis is the only one-dimensional analysis with a non-zero ω sets it apart from all other one-dimensional analyses. The consequence of a non-zero ω is discussed briefly later.

2.2.3 Variational Mechanics of $[(S)/90_n]_s$ Laminates

The first two-dimensional analysis for the $x-z$ plane was derived by Hashin [1–4]. Hashin made one and only one assumption—that the x-axis tensile stresses in each ply group depend only on x and are independent of z. Under this assumption and force balance, the x-direction tensile stresses of a microcracked laminate, with the inclusion of thermal stresses, are [5]:

$$\sigma_{xx}^{(1)} = k_m^{(1)}\sigma_0 - \psi(x) \qquad \text{and} \qquad \sigma_{xx}^{(2)} = k_m^{(2)}\sigma_0 + \frac{\psi(x)}{\lambda} \tag{2.28}$$

where $\psi(x)$ is an undetermined function of x. By integrating the stress equilibrium equations and making use of boundary conditions, it is possible to express the shear and transverse stresses in terms of $\psi(x)$ [1, 2, 5]:

$$\begin{aligned} \sigma_{xz}^{(1)} &= \psi'(x)z & \qquad \sigma_{xz}^{(2)} &= \frac{\psi'(x)}{\lambda}(h-z) \\ \sigma_{zz}^{(1)} &= \frac{\psi''(x)}{2}(ht_1 - z^2) & \qquad \sigma_{zz}^{(2)} &= \frac{\psi''(x)}{2\lambda}(h-z)^2 \end{aligned} \tag{2.29}$$

where $h = t_1 + t_2$, $z = 0$ is at the midplane of the laminate, and Eq. (2.29) applies for $z \geq 0$ (the stresses for $z < 0$ follow by symmetry). As can be verified by substitution, the above stress state satisfies equilibrium, traction boundary conditions, and interface stress continuity, and is therefore an admissible stress state. By the principle of minimum complementary energy, the function $\psi(x)$

27 INTENTIONALLY BLANK

that minimizes the complementary energy gives the best approximation to the microcracked cross-ply laminate stress state. The complementary energy is minimized using the calculus of variations. Hashin solved the elastic problem [1, 2] and Nairn extended his result to include thermal stresses and more general mechanical properties [5, 9, 51]. The governing Euler equation for finding $\psi(\xi)$ is [5]:

$$\frac{d^4\psi}{d\xi^4} + p\frac{d^2\psi}{d\xi^2} + q\psi = -k_{th}^{(1)}T \tag{2.30}$$

where $p = \frac{C_2 - C_4}{C_3}$, $q = \frac{C_1}{C_3}$, C_1 and C_4 are defined in Eqs. (2.5) and (2.24), and

$$C_2 = \frac{\nu_{xz}^{(1)}}{E_x^{(1)}}\left(\lambda + \frac{2}{3}\right) - \frac{\lambda\nu_{xz}^{(2)}}{3E_x^{(2)}} \tag{2.31}$$

$$C_3 = \frac{1}{60E_z^{(1)}}\left(15\lambda^2 + 20\lambda + 8\right) + \frac{\lambda^3}{20E_z^{(2)}} \tag{2.32}$$

The solution to Eq. (2.30) for the most common case of $4q/p^2 > 1$ is quoted from Ref. [5]:

$$\psi = \sigma_{x0}^{(1)}\phi(\xi) - k_{th}^{(1)}T \tag{2.33}$$

and

$$\sigma_{xx}^{(1)} = \sigma_{x0}^{(1)}(1 - \phi(\xi)) \tag{2.34}$$

where

$$\begin{aligned}\phi(\xi) = {} & \frac{2(\beta\sinh\alpha\rho\cos\beta\rho + \alpha\cosh\alpha\rho\sin\beta\rho)}{\beta\sinh 2\alpha\rho + \alpha\sin 2\beta\rho}\cosh\alpha\xi\cos\beta\xi \\ & + \frac{2(\beta\cosh\alpha\rho\sin\beta\rho - \alpha\sinh\alpha\rho\cos\beta\rho)}{\beta\sinh 2\alpha\rho + \alpha\sin 2\beta\rho}\sinh\alpha\xi\sin\beta\xi\end{aligned} \tag{2.35}$$

and

$$\alpha = \frac{1}{2}\sqrt{2\sqrt{q} - p} \qquad \text{and} \qquad \beta = \frac{1}{2}\sqrt{2\sqrt{q} + p} \tag{2.36}$$

The solution for $4q/p^2 < 1$ can be found in Ref. [5].

The x-axis tensile stress in the 90° plies and the interfacial shear and transverse stresses for a $[0/90_2]_s$ carbon/epoxy laminate are plotted in Fig. 2.6. The tensile stress ($\sigma_{xx}^{(1)}$) is qualitatively

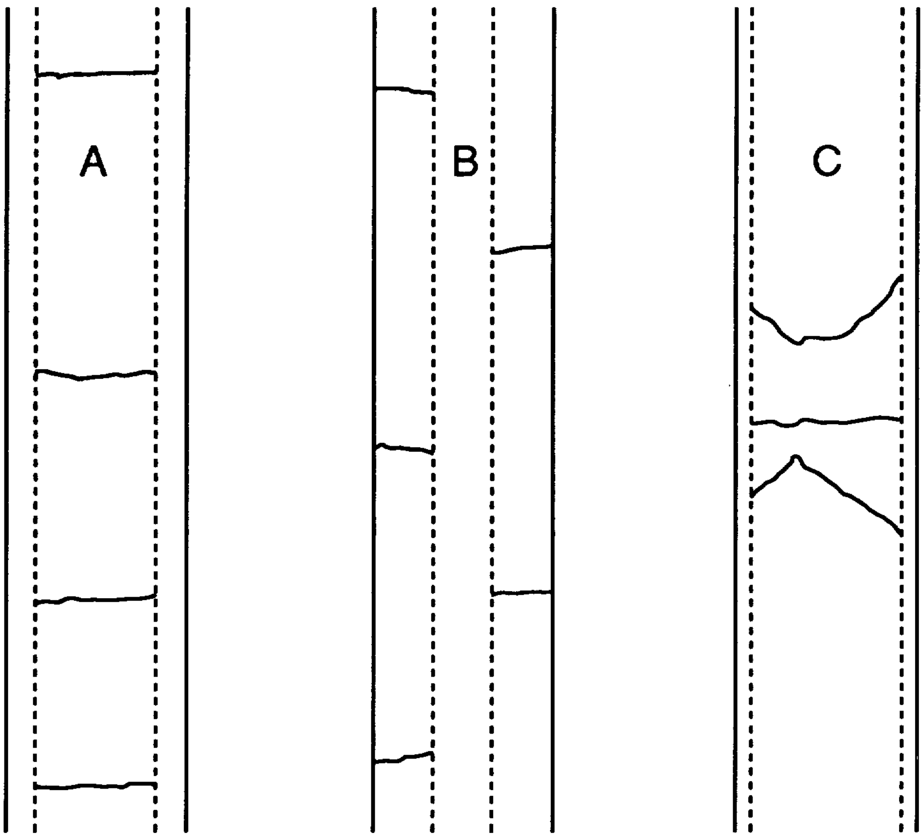

Figure 2.7: Sketches of actual edge views of typically damaged cross-ply laminates. A. Roughly periodic array of microcracks in a $[0/90_4]_s$ laminate. B. Antisymmetric or staggered microcracks in a $[90_4/0_2]_s$ laminate. C. Two curved or oblique microcracks near one straight microcrack in a $[0/90_8]_s$ laminate

a one-dimensional analysis. Although a direct comparison of their results to other one-dimensional analyses is difficult, their stress solutions, containing single $\sinh\phi\xi$ and $\cosh\phi\xi$ terms, are characteristic of one-dimensional solutions.

2.2.4 $[90_n/(S)]_s$ Laminates

The stress analysis of $[90_n/(S)]_s$ laminates is more complicated than the stress analysis of $[(S)/90_n]_s$ laminates. The major complicating feature arises from the observation of a staggered microcracking pattern in the two 90° ply groups [8, 10, 23] (see Fig. 2.7B).

Because the one-dimensional analyses do not include transverse stresses, they make no distinction between $[(S)/90_n]_s$ and $[90_n/(S)]_s$ laminates. In other words, the one-dimensional solution to the stresses in $[(S)/90_n]_s$ laminates is simultaneously a solution to the stresses in $[90_n/(S)]_s$ laminates. This discloses a severe deficiency of all one-dimensional analyses. Experimental observations show that the microcracking properties of $[90_n/(S)]_s$ laminates differ from from those of $[(S)/90_n]_s$ laminates [16, 51]. It is clear that no one-dimensional analysis can predict those differences. As stated in the *Introduction*, a good microcracking analysis should be able to correlate data from a wide variety of laminates. By this criterion, it is not possible to construct a successful analysis for microcracking using a one-dimensional stress analysis.

In contrast, a two-dimensional analysis includes transverse stresses and might be able to explain the microcracking properties of $[90_n/(S)]_s$ laminates. Nairn and Hu [10] extended Hashin's [1, 2] two-dimensional, variational mechanics analysis to account for the staggered microcracks in $[90_n/(S)]_s$ laminates. We briefly describe the analysis results below. Details are given in Ref. [10].

The two 90° ply groups are labeled 1 and 4. By analogy with the analysis of $[(S)/90_n]_s$ laminates, it is assumed that after the formation of microcracks, the x-axis tensile stresses in the two 90° ply groups change to

$$\sigma_{xx}^{(1)} = k_m^{(1)}\sigma_0 - \psi_1(x) \qquad \text{and} \qquad \sigma_{xx}^{(4)} = k_m^{(4)}\sigma_0 - \psi_4(x) \tag{2.37}$$

For symmetric laminates $k_m^{(1)} = k_m^{(4)}$. When the microcrack in ply group 4 is midway between the microcracks in ply group 1 (*i.e.* perfect stagger, see Fig. 2.4A) symmetry dictates that

$$\psi_4 = \begin{cases} \psi_1(\xi - \rho) & \text{for } \xi > 0 \\ \psi_1(\xi + \rho) & \text{for } \xi < 0 \end{cases} \tag{2.38}$$

By virtue of Eq. (2.38), $\psi_1(x)$ and $\psi_4(x)$ are dependent functions. They can be treated as independent functions, however, if we consider them only on the interval $(0, \frac{\rho}{2})$, which is one quarter of the "unit cell" of damage, and impose appropriate boundary conditions at $\xi = 0$ and $\xi = \frac{\rho}{2}$ [10]. After these two independent functions on the interval $(0, \frac{\rho}{2})$ are obtained, the complete ψ_1 and ψ_4 functions can be constructed by symmetry and Eq. (2.38) [10]. The solution on the interval $(0, \frac{\rho}{2})$

is determined by minimizing the complementary energy using the calculus of variations. When cast in terms of two new functions

$$X = \psi_1 + \psi_4 \qquad \text{and} \qquad Y = \psi_1 - \psi_4 \tag{2.39}$$

the complementary energy can be minimized analytically by solving two decoupled fourth order differential equations (see Ref. [10]).

The x-axis tensile stress in the 90° plies (group 1) and the interfacial shear and transverse stresses for a $[90_2/0]_s$ carbon/epoxy laminate are plotted in Fig. 2.8. The tensile stress ($\sigma_{xx}^{(1)}$) is zero at the two microcrack surfaces as required by boundary conditions. Midway between the two microcracks and directly opposite the microcrack in the 90° ply group on the opposing surface (see Fig. 2.4A) there is a local minimum in tensile stress. This local minimum is caused by a bending effect resulting from the asymmetric nature of the unit cell of damage. Two local maxima in tensile stress are located at positions close to $\frac{1}{3}$ and $\frac{2}{3}$ of the way from the bottom microcrack to the top microcrack. The distribution of the tensile stress shown in Fig. 2.8 can be used to explain the tendency towards staggered microcracks. If new microcracks form at all local tensile stress maxima in the 90° plies, the new damage state is equivalent to three unit cells of damage each being $\frac{1}{3}$ as large as the initial unit cell of damage [10] (see Fig. 2.4B). Thus, forming microcracks at positions of local maxima in tensile stresses leads to propagation of staggered microcracks.

As required by boundary conditions, the interfacial shear stress is zero on the microcrack surfaces. The shear stress is also zero at $\xi = 0$ due to symmetry. The peak shear stress is close to the microcrack surfaces and is similar in magnitude, but somewhat less than the peak $\sigma_{xx}^{(1)}$ stress.

$\sigma_{zz}^{(1)}$ plotted in Fig. 2.8 is the transverse stress along the 90/0 interface. There is a significant transverse stress concentration at the microcrack tip. The peak transverse stress is tensile and about twice as large as the peak $\sigma_{xx}^{(1)}$ stress. In dramatic contrast, the corresponding interfacial transverse stress in $[0/90_2]_s$ laminates shows a compressive stress concentration near the microcrack

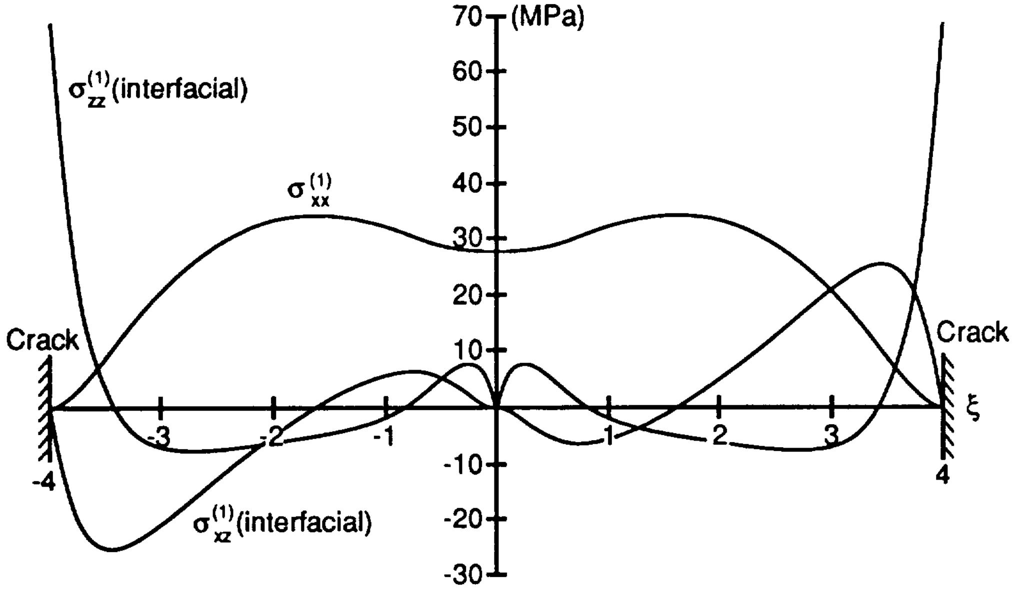

Figure 2.8: Stresses between two microcracks in the 90° ply group of a $[90_2/0]_s$ carbon/epoxy laminate from a two-dimensional, variational mechanics analysis. The applied stress is 100 MPa, the thermal load is $T = -125°\text{C}$, and the microcrack spacing is $\rho = 4$. The normal stress ($\sigma_{xx}^{(1)}$) is for the entire ply group. The plotted shear stress ($\sigma_{xz}^{(1)}$) and transverse stress ($\sigma_{zz}^{(1)}$) are the stresses along the 90/0 interface.

tips (see Fig. 2.6). The difference between $[90_2/0]_s$ and $[0/90_2]_s$ laminates in interfacial transverse stress is due to the bending effect caused by the asymmetric unit cell in $[90_2/0]_s$ laminates. It is the same bending effect that causes the local minimum in $\sigma_{xx}^{(1)}$. This high tensile transverse stress concentration is expected to promote mode I delamination initiating from the tips of microcracks. The difference in transverse tensile stresses between $[90_2/0]_s$ and $[0/90_2]_s$ laminates explains why, as observed by several authors [25, 31, 44], delamination initiation occurs more easily in $[90_n/0_m]_s$ laminates than in $[0_m/90_n]_s$ laminates.

2.2.5 Finite Element Analysis

Finite element analysis is used to look at the stresses in the presence of microcracks (*e.g.* Refs. [26–29, 38, 61]) or in the presence of microcracks and delaminations (*e.g.* Refs. [28, 62, 63]). Used in this way, finite element analysis is a powerful tool for calculating the stresses in a model of a damaged laminate. It can, for example, be used to verify the accuracy of analytical methods such as the shear-lag analysis or the variational analysis. It can also be used to suggest the form of the correct solution and therefore be helpful in choosing approximations for new analytical solutions [10].

Despite the important applications of finite element analysis, it is of limited use in developing useful micromechanics of damage models. Finite element analysis is best characterized as an experimental technique that can *measure* the stresses in model specimens. Even if the stress *measurement* is accurate, it is not sufficient for developing a microcracking analysis. A useful analysis requires knowledge of the stresses in the presence of any amount of damage and as a function of stacking sequence. Elucidating this information with finite element analysis may require hundreds of separate calculations. Thus, although finite elements could be used in principle, it is relatively intractable in practice. It is further unlikely that a finite element based analysis would find wide acceptance. It would be inhibited by the difficult task of transferring the methods from laboratory to laboratory. In this report, we limit our discussion of finite elements to information it gives about specific stress states or specific energy release rate calculations.

2.2.6 Stress Analysis Predictions for Modulus Reduction

As the density of microcracks increases, the longitudinal stiffness of the laminate decreases. At saturation microcrack density, the total modulus decrease ranges from about 5% to as much as 50% [1]. The maximum modulus reduction depends on laminate structure and material properties. Laminates whose axial stiffness is dominated by many 0° plies show a small modulus reduction. As the number of 90° plies increases and those plies play a greater role in the laminate stiffness, the laminate modulus reduction increases. The ratio of the transverse modulus to longitudinal (fiber direction) modulus of the unidirectional material is also important. The larger this ratio, the more the 90° plies contribute to laminate stiffness and therefore the larger the observed modulus reduction. To provide a critical test for theories that might predict modulus reduction, Highsmith and Reifsnider [23] did modulus reduction experiments on $[0/90_3]_s$ glass/epoxy laminates (Scotch Ply 1003). The $[0/90_3]_s$ stacking sequence was purposefully chosen to provide a laminate that is not dominated by the 0° plies. The ratio of the transverse modulus to longitudinal modulus of this glass/epoxy material is higher than it is for typical carbon/epoxy materials. The modulus reduction for glass/epoxy laminates is thus larger than it is for the corresponding carbon/epoxy laminate. In this section we compare Highsmith and Reifsnider's [23] experimental results—modulus as a function of microcrack density—with the predictions made by the one-dimensional analyses and by the two-dimensional, variational mechanics analysis.

From knowledge of the stress distribution, we can calculate the total displacement of the load bearing 0° plies between two microcracks. From this result it is easy to calculate the effective laminate modulus. Nairn and Hu [51] did this calculation for all the one-dimensional analyses and the variational analysis. Their results, which compare the modulus reduction predictions with experimental data, are plotted in Fig. 2.9. The first and simplest one-dimensional analysis by Garrett and Bailey [12] agrees well with experimental observations. Later attempts for improved one-dimensional analyses generally give worse results. The analysis by Ogin *et. al.*, *i.e.*, the analysis that assumes parabolic displacements [42, 43, 54, 55], under predicts the modulus reduction. In effect, the assumption of parabolic displacement makes the damaged 90° plies too stiff. Flaggs' shear-lag analysis [52] and Nuismer and Tan's elasticity analysis [57], which account for Poisson effects by including the y dimension, look better than the Ogin *et. al.* [42, 43, 54, 55] analysis, but they are still too stiff and worse than Garrett and Bailey's [12] analysis. The non-zero $\omega(P)$ function in Nuismer and Tan's [57] analysis has little or no effect on the modulus reduction prediction. A plot with $\omega(P) = 0$ is indistinguishable from the Nuismer and Tan plot in Fig. 2.9. The Reifsnider type analysis, or a shear-lag analysis that uses an effective shear stress transfer layer [36, 53, 56], is in excellent agreement with experimental data. This excellent agreement, however, comes at

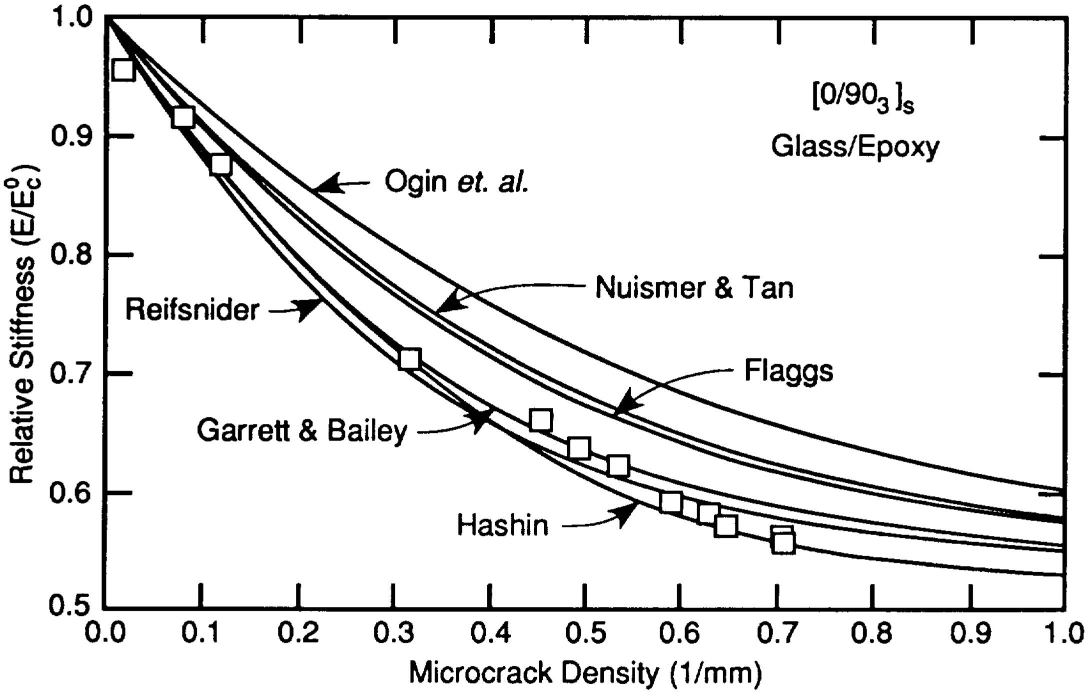

Figure 2.9: Relative modulus as a function of microcrack density for a $[0/90_3]_s$ glass/epoxy (Scotch Ply 1003) laminate. The data points are experimental results from Ref. [24]. The smooth lines are theoretical predictions by various stress analysis procedures.

the cost of using an adjustable parameter—G/t_0, the effective shear stiffness of the shear stress transfer layer. Overall, Hashin's [1, 2] variational mechanics analysis provides the best agreement with Highsmith and Reifsnider's [23] experimental observations. The improvement of Hashin's analysis over the best one-dimensional analysis, however, is only marginal.

Judged solely by their ability to fit the experimental data of Highsmith and Reifsnider [23], we should avoid the analyses that assume parabolic displacement and the quasi-two dimensional analyses of Flaggs [52] and Nuismer and Tan [57] as being too stiff. Of the remaining three analyses, we should avoid the analysis that uses an effective shear stress transfer layer [36, 53, 56] because it achieves agreement with experimental observations only by using an adjustable parameter that is not required in the other two analyses. Between the Garrett and Bailey [12] analysis and the Hashin [1, 2] analysis, we note that they have one assumption in common. The common assumption, which is the only assumption in the Hashin [1, 2] analysis, is that $\sigma_{xx}^{(i)}$ is independent of z. By the principles of variational mechanics, the Hashin [1, 2] analysis which minimizes complementary energy, is assured of finding the best approximation for all possible stress states with $\sigma_{xx}^{(i)}$ independent of z. We can thus conclude with mathematical rigor that the Hashin [1, 2] analysis is more accurate than the Garrett and Bailey [12] analysis.

2.3 Comparison of Microcracking Experiments to Theory

Though necessary, an ability to fit the modulus reduction data of Highsmith and Reifsnider [23] in the previous section is not sufficient to guarantee that a particular stress analysis is capable of providing a micromechanics of damage analysis for microcracking. The true test of any stress analysis is its ability to be used in conjunction with failure criteria to predict laminate failure properties. In this section we explore the various failure models that have been proposed for predicting the initiation and propagation of microcracks. We compare the predictions to our new experiments on several different composite materials and many different stacking sequences. When we attempt to apply the failure criteria to make definite predictions, we do so by using Hashin's [1, 2, 5, 6, 10] two-dimensional, variational mechanics analysis extended to include residual stresses. We find less incentive, except historical interest, to explore the predictions made when using any one-dimensional analysis as we believe them to be less accurate than Hashin's [1, 2] analysis.

2.3.1 Materials and Methods

During the course of this project we did microcracking on many different composite materials. The materials studied included Hercules AS4 graphite/3501-6 epoxy, Hercules IM6/DuPont Avimid® K polymer, T300 graphite/Fiberite 934 epoxy, T300 graphite/Fiberite 977-2 thermoplastic toughened epoxy, and Hercules AS4 graphite/ICI PEEK. For each material we made a series of laminates with 90° plies. The generic layups either had 90°plies in the middle ($[(S)/90_n]_s$ laminates) or had 90°

plies on each free surface ($[90_n/(S)]_s$ laminates). Specimens, which were nominally 12 mm wide and 150 mm long with thicknesses determined by the stacking sequences (about 0.125 mm per ply), were cut from laminate plates. All specimens had 19 mm by 12 mm aluminum end tabs attached using Hysol 9230 epoxy.

All tensile tests were run in displacement control, at a rate of 0.005 mm/sec, on a Minnesota Testing Systems (MTS) 25 kN servohydraulic testing frame. Load *vs.* displacement curves were collected on an IBM PC-XT that was interfaced to an MTS 464 Data Display Device. While testing each specimen, the experiment was periodically stopped and the specimen was examined by optical microscopy. For $[(S)/90_n]_s$ laminates we mapped the complete distribution of microcrack spacings on either edge of the specimen. To get an average crack density, we averaged the densities on the two specimen edges. For $[90_n/(S)]_s$ laminates, microcracks could be seen on the edges and on the faces of the specimen. We mapped the complete distribution of microcrack spacings in each of the two surface 90° ply groups. To get an average crack density, we averaged the densities of the two 90° ply groups. The specimens were continually reloaded into the MTS frame and tested to higher displacements until the end tabs failed, the specimen broke, or delamination began.

2.3.2 Microcrack Initiation

Garrett and Bailey [12] assumed that microcracking initiates when the x-direction stress in the 90° plies becomes equal to the transverse tensile strength of the unidirectional material. The theory simply states that microcracking initiates when

$$\sigma_{x0}^{(1)} = \sigma_T \tag{2.40}$$

where σ_T is the transverse tensile strength of a unidirectional laminate. Solving this equation for applied strain, we obtain the strain to initiate microcracking as

$$\varepsilon_{init} = \frac{\sigma_T - k_{th}^{(1)}T}{E_c^0 k_m^{(1)}} \tag{2.41}$$

where E_c^0 is the longitudinal modulus of the undamaged laminate. This analysis is simply a first-ply failure model derived using a maximum stress failure criterion.

Though simple in concept, the strength model or first-ply failure theory does not agree with experimental observations. A straight forward experiment that demonstrates the poor agreement is to measure the stress to initiate microcracking for a series of laminates. If that stress is σ_{init}, we can calculate $\sigma_{x0}^{(1)}$ at the time of microcrack initiation using

$$\sigma_{x0}^{(1)} = k_m^{(1)}\sigma_{init} + k_{th}^{(1)}T \tag{2.42}$$

If the strength theory is valid, the calculated $\sigma_{x0}^{(1)}$ should be independent of laminate structure and for all laminates it should be equal to σ_T. The finding is that $\sigma_{x0}^{(1)}$ at microcrack initiation is strongly dependent on laminate structure [20, 39]. As the thickness of the 90° plies decreases, $\sigma_{x0}^{(1)}$ at microcrack initiation increases.

Crossman and Wang [39] recognized that $\sigma_{y0}^{(1)}$ at failure is also nonzero and that a simple strength criterion based solely on the magnitude of $\sigma_{x0}^{(1)}$ might be inadequate. To check for the possibility that more "sophisticated" failure criteria, such as a quadratic failure criteria, might work better than the simple strength criterion, Crossman and Wang [39] measured both $\sigma_{x0}^{(1)}$ and $\sigma_{y0}^{(1)}$ at microcrack initiation. Their finding is that no rational stress or strain based criterion can explain the dependence of microcrack initiation stress on laminate structure [39].

The only way a strength based micromechanics of damage analysis can work is if the transverse ply strength is treated is an *in situ* or laminate dependent property [20]. This approach, however, violates the principles of a good micromechanics of damage analysis [51]. A good micromechanics of damage analysis should be definite enough that predictions can be made. Because a model that depends on *in situ* properties cannot be used to make predictions, it is by definition *not* definite.

Some have argued that the strength model fails because a deterministic strength is used and that it should be replaced by a probabilistic or statistical strength model [20, 31, 32, 53, 64]. In support of a statistical strength model, we note that $\sigma_{x0}^{(1)}$ at failure increases as the thickness of the 90° plies decreases. The increase in $\sigma_{x0}^{(1)}$ could be attributed to a size affect. Thinner 90° plies statistically have less flaws and therefore should have a higher effective strength. Two experimental observations, however, argue against using statistical strength models. First consider microcracking in $[(S)/90_n]_s$ laminates *vs.* microcracking in $[90_n/(S)]_s$ laminates. The former fails by microcracking in a (90_{2n}) sublaminate while the latter fails by microcracking in two smaller (90_n) sublaminates. By the statistical strength theory, microcracking should form more easily in $[(S)/90_n]_s$ laminates than $[90_n/(S)]_s$ laminates. The experimental observation is just the opposite—the stress to initiate microcracking in $[90_n/(S)]_s$ laminates is lower than it is in $[(S)/90_n]_s$ laminates [16].

The second experimental observation discounting statistical strength theories is similar to the measurement of $\sigma_{x0}^{(1)}$ at microcrack initiation that discounts deterministic strength theories. The experiment is to assume that the transverse strength of the 90° plies follows a two-parameter Weibull distribution and measure those parameters for 90° plies in different laminates. The findings are that the Weibull parameters depend on the thickness of the 90° plies [20, 32]. Like the deterministic strength theories, the only way a statistical strength theory can work is if the distribution in transverse strength is treated as an *in situ* property. In short, statistical strength theories do not yield definite micromechanics of damage analyses that have predictive capabilities.

The failure of strength based models led Parvizi *et. al.* [14] to propose an energy criterion. They postulated that the first microcrack forms when the *total* energy released due to the formation of that microcrack exceeds some critical value. If G_m is the energy release rate associated with the formation of a complete microcrack, the energy failure criterion is that a microcrack forms when $G_m \geq G_{mc}$. We call G_{mc} the microcracking fracture toughness or the intralaminar fracture toughness of the composite material system.

Since the work of Parvizi *et. al.* [14], the energy criterion has gained popularity and appeared in Refs. [5, 6, 8, 10,15–18, 25, 54–58, 61]. As will be shown later in this report, the energy criterion works well, provided it is implemented correctly. Predicting failure on the basis of *total* energy release rate, however, is an unconventional application of fracture mechanics. Conventional fracture mechanics begins with some initial flaw and calculates the energy release rate for an incremental amount of crack growth. Before proceeding, some qualitative comments on the *total* energy criterion are warranted. Imagine an initial small flaw of size a_0 in the y direction within the 90° plies and let $G_m(a)$ be the energy release rate for incremental crack growth in the y direction from a flaw of size a. As the microcrack propagates in the y direction, the flaw size increases from a_0 to the full width of the laminate or W. The total energy released during crack growth (defined above as G_m) is

$$G_m = \frac{1}{W - a_0} \int_{a_0}^{W} G_m(a)da \tag{2.43}$$

Conventional fracture mechanics assumes that for a flaw of size a_0 that the crack will propagate when $G_m(a_0) > G_{mc}$. Lets consider the case, however, for which $G_m(a)$ is independent of a. Then Eq. (2.43) reduces to

$$G_m = \frac{G_m}{W - a_0} \int_{a_0}^{W} da = G_m \tag{2.44}$$

and conventional fracture mechanics predicts failure when $G_m > G_{mc}$. This criterion is identical to the one discussed above that was proposed by Parvizi *et. al.* [14]. Thus, although predicting failure on the basis of *total* total energy release rate is unconventional fracture mechanics, it is rigorously equivalent to conventional fracture mechanics for the special case in which energy release rate is independent of flaw size. Indeed, both Dvorak and Laws [65, 66] and Hahn and Johannesson [67], on the basis of theoretical arguments, and Boniface and Ogin [22], on the basis of fatigue crack propagation results, have suggested that G_m is independent of flaw size. The ultimate test of this unconventional fracture mechanics, however, is how well it compares to experimental results. Those comparisons (given latter in the report) can be viewed as more evidence that G_m is independent of flaw size.

To make predictions based on the energy criterion it is necessary to calculate the energy release rate associated with the formation of the first microcrack:

$$G_m = \frac{\partial \Omega}{\partial A} - \frac{\partial U}{\partial A} \tag{2.45}$$

where Ω is external work, U is internal strain energy, and A is fracture surface area. The formation of the first microcrack at constant load causes the total laminate displacement and internal strain energy to increase by Δu and ΔU respectively, and creates new fracture surface area $\Delta A = 2t_1W$. The energy release rate due the formation of the first microcrack is

$$G_m = \frac{\sigma_0 BW\Delta u - \Delta U}{2t_1W} \tag{2.46}$$

where σ_0 is the applied stress to initiate microcracking. It is certainly possible to calculate Δu and ΔU and therefore to calculate G_m from any approximate stress analysis. Many authors have given roughly equivalent results for G_m calculated from one-dimensional analyses [12–15, 25, 54–58] In view of the deficiencies in the one-dimensional analyses pointed previously, however, the application of one-dimensional analyses to any failure criterion is only of historical interest. As previously stated, we concentrate on using Hashin's two-dimensional, variational mechanics analysis extended to include thermal stresses [1, 2, 5, 6, 10]. The variational mechanics analysis for microcrack initiation gives [68]:

$$G_m = 2\sigma_{x0}^{(1)^2}\alpha\sqrt{C_1C_3} = \sigma_{x0}^{(1)^2}t_1\sqrt{C_1\left(C_4 - C_2 + 2\sqrt{C_1C_3}\right)} \tag{2.47}$$

where α is defined in Eq. (2.36).

By the energy criterion, the first microcrack forms when $G_m \geq G_{mc}$. Solving Eq. (2.47) for applied strain, we predict the strain to initiate microcracking as

$$\varepsilon_{init} = \frac{1}{k_m^{(1)}E_c^0}\left[\sqrt{\frac{G_{mc}}{t_1\sqrt{C_1\left(C_4 - C_2 + 2\sqrt{C_1C_3}\right)}}} - k_{th}^{(1)}T\right] \tag{2.48}$$

This prediction is in better agreement with experimental observation than any strength model because it correctly predicts that the strain to initiate microcracking increases significantly as the thickness of the 90° plies decreases [14, 68]. The agreement for laminates with very thick 90° plies is not as good. In general the energy theory predicts that the strain to initiate microcracking decreases farther than what is experimentally observed [14]. Although the energy criterion is not a perfect failure criterion, it appears to capture most features of the experimental observations and to be a significant improvement over strength theories.

The inability of the energy criterion to fit all experimental microcrack initiation results may be related to deficiencies in the stress analysis (*e.g.* the assumption of constant x-direction tensile stress within ply groups). Alternatively, it may be due to practical problems associated with microcrack initiation experiments. In microcrack initiation experiments, one looks for the first microcrack and obtains only one data point per laminate. For imperfect laminates containing processing flaws, these types of experiments are inherently sensitive to flaws and perhaps even dominated by flaws. Because processing flaws do not enter the energy release rate calculation, none of the discussed theories can explain results that are influenced by processing flaws. Recent experimental evidence suggests that the first few microcracks are indeed associated with laminate flaws [6]. By microscopy, the early microcracks were noted to be near obvious processing flaws [6]. These comments imply that microcrack initiation experiments may not be the best experiments for studying the microcracking process. The preferred experiments are those that measure microcrack density as a function of applied load. In microcrack density experiments, one obtains many data points from a single laminate. If the first few microcracks are caused by laminate flaws, they can be ignored and many points still remain for studying the microcracking process. Although early microcracking investigations concentrated on microcrack initiation experiments, most recent studies involve microcrack density experiments.

2.3.3 Microcrack Density in $[(S)/90_n]_s$ Laminates

In our microcrack density experiments, we measured the microcrack density as a function of applied load. The goal of the micromechanics of damage analysis is to predict the experimental results. Hopefully the prediction can be applied to a variety of laminate structures and materials. We obtained the most results for Hercules AS4/3501-6 laminates. In this section we consider some microcracking theories and how well they predict some of our new data.

As with microcrack initiation experiments, the first attempt at predicting microcrack density experiments was a simple strength model [12]. From all stress analyses, the maximum tensile stress in the 90° ply group occurs midway between two existing microcracks at $\xi = 0$. The strength theory predicts that the next microcrack occurs when the longitudinal stress at $\xi = 0$ becomes equal to the transverse tensile strength of the unidirectional material, σ_T. Using the variational mechanics solution [1, 2, 5, 6, 10], the next microcrack occurs when

$$\sigma_T = \sigma_{x0}^{(1)}(1 - \phi(0)) \tag{2.49}$$

where $\phi(0)$ is defined in Eq. (2.35). Solving for applied stress, we predict the stress as a function of microcrack density to be

$$\sigma_0 = \frac{1}{k_m^{(1)}}\left(\frac{\sigma_T}{1 - \phi(0)} - k_{th}^{(1)}T\right) \tag{2.50}$$

If σ_T is treated as an adjustable parameter, the strength theory predictions are in reasonable agreement with experimental observations [12]. The problem with the strength theory is that fitting results from the different laminate structures in our new experiments requires using different values of σ_T for each laminate. In other words, the transverse tensile strength must be treated as an *in situ* or laminate dependent property. Several investigators tried statistical strength theories for microcrack densities [21, 31, 32, 53, 64]. As in the simple strength model, however, the Weibull parameters must be treated as *in situ* or laminate dependent properties if one hopes to fit results from different laminates [32]. We thus conclude that micromechanics of damage models based on strength theories have little useful predictive capability.

Although energy release rate failure criteria were proposed for microcrack initiation in 1978 [14], it was not until 1986 that Caslini *et. al.* [25] suggested using total microcrack energy release rate to predict microcrack density as a function of applied load. The expression for energy release rate is given by Eq. (2.46). For any of the approximate stress analyses it is a straight forward matter to calculate W and U as functions of microcrack density. The less straight forward matter is how to evaluate the derivative terms $\frac{\partial W}{\partial A}$ and $\frac{\partial U}{\partial A}$. If D is the microcrack density, then the total microcrack fracture area is $A = 2t_1WLD$. Caslini *et. al.* [25] treated A as a continuous variable and used the one-dimensional analysis of Ogin *et. al.* [42, 43] to derive a simple expression for G_m. Han *et. al.* [54, 55] used an identical stress analysis and a crack closure technique to derive an identical expression for G_m. As explained in the next section, this *analytical* derivative approach as now been show to give very poor results. An alternative way to calculate G_m is required.

Laws and Dvorak [56] recognized that A is not a continuous variable but changes in discrete steps of $\Delta A = 2t_1W$ following the formation of each new microcrack. They advocated considering the formation of a new microcrack at a given microcrack density as a discrete process as illustrated in Fig. 2.3. The energy release rate for the formation of a complete microcrack is the difference in energy between the three microcrack state in Fig. 2.3B and the two microcrack state in Fig. 2.3A. Laws and Dvorak [56] calculated a discrete energy release rate using a one-dimensional analysis.

Nairn *et. al.* [5, 6, 8] calculated the microcracking energy release rate using Hashin's variational mechanics analysis extended to include thermal stresses [1, 2, 5, 6, 10]. Although most microcrack density analyses assume periodic arrays of microcrack spacing, the variational mechanics analysis can handle any distribution of microcrack spacings. Consider a specimen with N microcracks characterized by microcrack spacings $\rho_1, \rho_2, \ldots, \rho_N$. From the variational mechanics analysis the specimen compliance is [5, 6]:

$$C = C_0 + \frac{2C_3 t_1 L k_m^{(1)^2}}{B^2 W} \frac{\sum_{i=1}^{N} \chi(\rho_i)}{\sum_{i=1}^{N} \rho_i} \tag{2.51}$$

where $C_0 = L/BE_c^0 W$ is the compliance of the undamaged laminate and the function $\chi(\rho)$ is defined in Refs. [1, 2, 5, 6, 10]. Physically, $\chi(\rho)$ is the excess strain energy in the laminate associated with the presence of microcracking in the 90° plies. Nairn *et. al.* [5, 6, 8] derived an expression for G_m in terms of a derivative of the compliance:

$$G_m = \frac{B^2 W^2 \sigma_{x0}^{(1)^2}}{2k_m^{(1)^2}} \frac{dC}{dA} \tag{2.52}$$

Evaluating $\frac{dC}{dA}$ by differentiating Eq. (2.51) results in the final energy release rate expression [5, 6, 8]:

$$G_m = \sigma_{x0}^{(1)^2} C_3 t_1 Y(D) \tag{2.53}$$

where $Y(D)$ is a function that depends on the microcrack density, $D = \frac{N}{L}$, or more formally on the complete distribution of microcrack spacing:

$$Y(D) = LW \frac{d}{dA} \frac{\sum_{i=1}^{N} \chi(\rho_i)}{\sum_{i=1}^{N} \rho_i} = \frac{d}{dD}\Big(D\langle\chi(\rho)\rangle\Big) \tag{2.54}$$

where $\langle\chi(\rho)\rangle$ is the average value of $\chi(\rho)$ over the N microcrack intervals.

To use Eq. (2.53), $Y(D)$ must be evaluated. Following Laws and Dvorak [56], Nairn *et. al.* [5, 6, 8] evaluated $Y(D)$ for the discrete process of forming a new microcrack at dimensionless position $\xi = 2\delta - \rho_k$ in the k^{th} microcrack interval (see Fig. 2.3B). A discrete differentiation of Eq. (2.54) results in

$$Y(D) = \frac{\Delta D\langle\chi(\rho)\rangle}{\Delta D} = \chi(\rho_k - \delta) + \chi(\delta) - \chi(\rho_k) \tag{2.55}$$

During a typical experiment, one does not know where the next microcrack will form and therefore does not know ρ_k or δ. It is known, however that $[(S)/90_n]_s$ laminates tend to form regularly spaced microcracks, especially when microcrack density is high enough that processing flaws play no role.

We thus might expect

$$\rho_k \approx \langle\rho\rangle \qquad \text{and} \qquad \delta \approx \frac{\langle\rho\rangle}{2} \tag{2.56}$$

where $\langle\rho\rangle$ is the average value of ρ_i. With these approximations

$$Y(D) \approx 2\chi(\langle\rho\rangle/2) - \chi(\langle\rho\rangle) \tag{2.57}$$

Liu and Nairn [6] note results that are sensitive to the distribution of microcrack spacings and thus Eq. (2.57) is sometimes an oversimplification. From Eq. (2.53) it can be calculated that the energy release rate is higher when the microcrack forms in a large microcrack interval than it is when it forms in a small microcrack interval. If we assume that microcrack formation prefers locations that maximize energy release rate, then ρ_k will tend to be larger than $\langle\rho\rangle$ and δ will tend to be larger than $\frac{\langle\rho\rangle}{2}$. The best way to account for microcrack spacing distribution effects is to measure that distribution and calculate $Y(D)$ using Eq. (2.54). This approach is very tedious and Liu and Nairn [6] suggest a simpler approach that is in good agreement with experiments. Let the size of the microcrack interval where the new microcrack forms be a factor f times larger than the average microcrack interval. Then on average

$$\rho_k \approx f\langle\rho\rangle \qquad \text{and} \qquad \delta \approx \frac{f\langle\rho\rangle}{2} \tag{2.58}$$

which gives

$$Y(D) \approx 2\chi(f\langle\rho\rangle/2) - \chi(f\langle\rho\rangle) \tag{2.59}$$

Using f values between 1.0 and 1.44, Liu and Nairn [6] find good fits to results from a wide variety of laminates. An experimental technique for measuring f, developed in this contract, verifies that is is usually between 1.0 and 1.44 with an average value of about 1.2.

A rigorous test of the energy release rate theory requires experiments on many different laminate structures. We measured the microcrack density as a function of applied load in 21 different

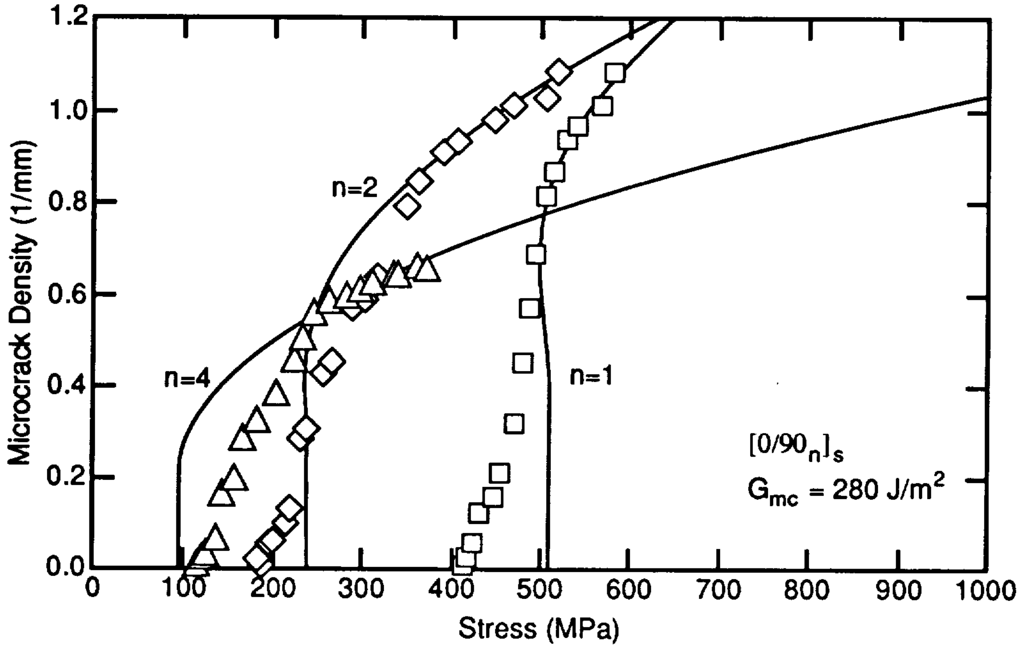

Figure 2.10: Microcrack density as a function of applied load in a series of AS4/Hercules 3501-6 carbon/epoxy laminates. The symbols are experimental data points. The smooth lines are predictions using the variational mechanics energy release rate theory and $G_{mc} = 280$ J/m^2

layups of AS4/Hercules 3501-6 carbon/epoxy laminates. We compare a few of those results to predictions for experimental verification that the energy release rate theory predicts the microcracking properties of $[(S)/90_n]_s$ laminates. Latter in this chapter we present an *master plot* approach that allows us to efficiently compare all experimental results to the theoretical predictions.

Solving Eq. (2.53) for applied stress, we obtain the stress as a function of microcrack density as

$$\sigma_0 = \frac{1}{k_m^{(1)}}\left(\sqrt{\frac{G_{mc}}{C_3 t_1 Y(D)}} - k_{th}^{(1)} T\right) \tag{2.60}$$

There is one unknown parameter in Eq. (2.60)—G_{mc}, the microcracking fracture toughness of the composite material system. For a single laminate, we can measure G_{mc} by fitting Eq. (2.60) to experimental results. If G_{mc} is a useful material property, however, it should be independent of laminate structure. If a single value of G_{mc} predicts the results from many different laminates, then we can claim experimental verification of a energy release rate micromechanics of damage model.

The results for $[0/90_n]_s$ laminates with $n = 1$, 2, and 4 are given in Fig. 2.10. All results are fit with a single value of $G_{mc} = 280$ J/m^2. This value of G_{mc} is similar, but slightly higher than the delamination or *interlaminar* fracture toughness of this material. The fits are good but we point out two deficiencies that should be the subject of future work. For $n = 4$ or for thick 90° ply groups, we consistently observed experimental results rising slower than predicted. This discrepancy could be associated with the approximate stress analysis that assumes the x-axis tensile stresses to be independent of z [1, 2, 5, 6, 10]. When the ply groups get thick, this approximation may be an oversimplification. For $n = 1$, a few microcracks start before the predicted rise in microcrack density. These early microcracks are probably associated with laminate flaws [6]. To account for these early microcracks, the energy theory needs to be modified to include laminate imperfections.

2.3.4 Microcracking in $[90_n/(S)]_s$ Laminates

An important class of cross-ply laminates receiving significantly less study is laminates of generic layup $[90_n/(S)]_s$ or laminates having outer-ply 90° ply groups. The microcracking properties of $[90_n/(S)]_s$ laminates differ from those of the corresponding $[(S)/90_n]_s$ laminates. In particular, the initial microcracks form at lower loads in $[90_n/(S)]_s$ laminates and at saturation damage, the microcrack density of $[90_n/(S)]_s$ laminates is lower. Furthermore, $[90_n/(S)]_s$ laminates develop a staggered or antisymmetric pattern of damage (see Figs. 2.7 and 2.4) that complicates the stress analysis and the resulting micromechanics of damage analysis. In this section, we explore the use of an energy based micromechanics of damage model to predict the microcrack density as a function of applied load for $[90_n/(S)]_s$ laminates.

As explained in the Stress Analysis section, a one-dimensional analysis cannot explain the observed differences between $[(S)/90_n]_s$ and $[90_n/(S)]_s$ laminates—we must use a two dimensional $x-z$ plane analysis. Nairn and Hu [10] extended Hashin's two-dimensional, variational mechanics analysis [1, 2] of $[(S)/90_n]_s$ laminates to $[90_n/(S)]_s$ laminates having staggered microcracks. They cast the solution in a form similar to the $[(S)/90_n]_s$ laminate analysis. The total energy release rate for the formation a new microcrack is expressed as

$$G_m = \sigma_{x0}^{(1)^2} C_3 t_1 Y_a(D) \tag{2.61}$$

where $Y_a(D)$ is

$$Y_a(D) = LW \frac{d}{dA} \frac{\sum_{i=1}^{N} \chi_a(\rho_i)}{\sum_{i=1}^{N} \rho_i} = \frac{d}{dD}\Big(D\langle\chi_a(\rho)\rangle\Big) \tag{2.62}$$

Evaluating the derivative in Eq. (2.62) by a discrete process of forming staggered microcracks and introducing the "f" factor to account for a distribution in crack spacings results in [10]:

$$Y_a(D) \approx \frac{1}{2}(3\chi_a(f\langle\rho\rangle/3) - \chi_a(f\langle\rho\rangle)\Big) \tag{2.63}$$

Equations (2.61) and (2.62) are identical to the corresponding expressions for $[(S)/90_n]_s$ laminates (Eqs. (2.53) and (2.54)) except that $Y_a(D)$ and $\chi_a(\rho)$ replace $Y(D)$ and $\chi(\rho)$. The subscript a denotes laminates with antisymmetric or staggered microcracks. Physically $\chi_a(\rho)$ corresponds to the excess strain energy caused by the presence of staggered microcracks in a unit cell of damage of dimensionless spacing 2ρ (See Fig. 2.4). The function $\chi_a(\rho)$ is more complex than $\chi(\rho)$ and the reader is referred to Ref. [10] for details.

To test the microcracking analysis for $[90_n/(S)]_s$ laminates we compare the predictions to experimental results. Our 21 layup study of microcracking in AS4/Hercules 3501-6 carbon/epoxy laminates included $[90_n/(S)]_s$ laminates. In fact, we have a more rigorous test for $[90_n/(S)]_s$ laminates than we did for $[(S)/90_n]_s$ laminates. The reason is that the results on $[(S)/90_n]_s$ laminates can be viewed as experiments that measured $G_{mc} = 280$ J/m^2. If Eq. (2.61) correctly accounts for outer-ply 90° plies and staggered microcracks, then it should be possible to fit experimental results for $[90_n/(S)]_s$ laminates with the same value of G_{mc}.

The results for $[90/0_n]_s$ laminates with $n = 0.5$, 1, 2, and 4 are given in Fig. 2.11. All results are fit with a single value of $G_{mc} = 240$ J/m^2. This microcracking fracture toughness is lower

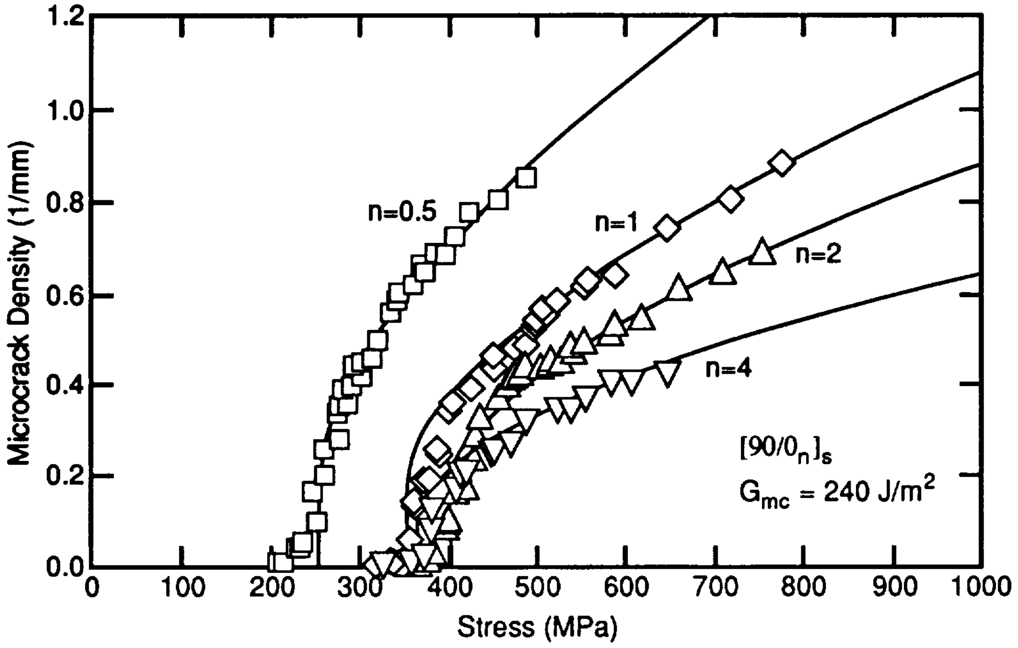

Figure 2.11: Microcrack density as a function of applied load in a series of AS4/Hercules 3501-6 carbon/epoxy laminates. The symbols are experimental data points. The smooth lines are predictions using the variational mechanics energy release rate theory and $G_{mc} = 240\ J/m^2$

than the toughness used to fit the results for $[0_n/90_m]_s$ but close enough to be within experimental uncertainty. The fits for the $[90/0_n]_s$ laminates are better than the fits for the $[0_n/90]_s$ laminates. The most important point from Figs. 2.10 and 2.11 is that a unified fracture theory can predict results from both $[(S)/90_n]_s$ and $[90_n/(S)]_s$ laminates.

2.4 Master Plot Analysis

Plots like those in Figs. 2.10 and 2.11 show that the variational analysis and the energy release rate failure criterion can predict microcracking properties of $[(S)/90_n]_s$ and $[90_n/(S)]_s$ laminates. For a critical evaluation of any microcracking theory, however, it is desirable to test it with many different layups. Comparing each laminate to theory requires many plots. If possible, it is preferable to develop a master plot approach that uses scaling laws to plot microcracking results from all laminates on a single plot. A single master plot will quickly reveal the adequacy of the microcracking theory.

In this section we develop a master plot analysis for microcracking. The master plot approach is used to critically evaluate the microcracking analysis of the previous section. In brief, we measured microcracking properties of 21 different layups of Hercules AS4/3501-6 laminates. Three of those laminates failed by premature delamination, but 18 gave sufficient microcracking results to compare to theory. The 18 laminates included some with 90° plies in the middles, some with 90° plies on the free surface, some with supporting (S) sublaminates of (0_n), and some with the supporting (S) sublaminates of (±15) or (±30). We found that the variational analysis and the energy release rate failure criterion works well and can correlate all experimental results.

We were able to extend the master plot technique to evaluate previous microcracking theories. We found that no theory that uses a failure criterion other than the energy release rate failure criterion can explain the results. In particular maximum stress or maximum strain failure criteria were bad. We also found that all one-dimensional stress analyses, regardless of failure criterion, gave poor results.

2.4.1 Variational Analysis of One Laminate

Multiplying Eq. (2.60) by $-k_m^{(1)}/k_{th}^{(1)}$ gives

$$-\frac{k_m^{(1)}}{k_{th}^{(1)}}\sigma_0 = -\frac{1}{k_{th}^{(1)}}\sqrt{\frac{G_{mc}}{C_3 t_1 Y(D)}} + T \tag{2.64}$$

This equation leads us to define a reduced stress and a reduced crack density as

$$\begin{aligned} \text{reduced stress:} \quad & \sigma_R &=& -\tfrac{k_m^{(1)}}{k_{th}^{(1)}}\sigma_0 \\ \text{reduced crack density:} \quad & D_R &=& -\tfrac{1}{k_{th}^{(1)}}\sqrt{\tfrac{1}{C_3 t_1 Y(D)}} \end{aligned} \tag{2.65}$$

A similar analysis for microcracking in $[90_n/(S)]_s$ laminates gives

$$-\frac{k_m^{(1)}}{k_{th}^{(1)}}\sigma_0 = -\frac{1}{k_{th}^{(1)}}\sqrt{\frac{G_{mc}}{C_{3a} t_1 Y_a(D)}} + T \tag{2.66}$$

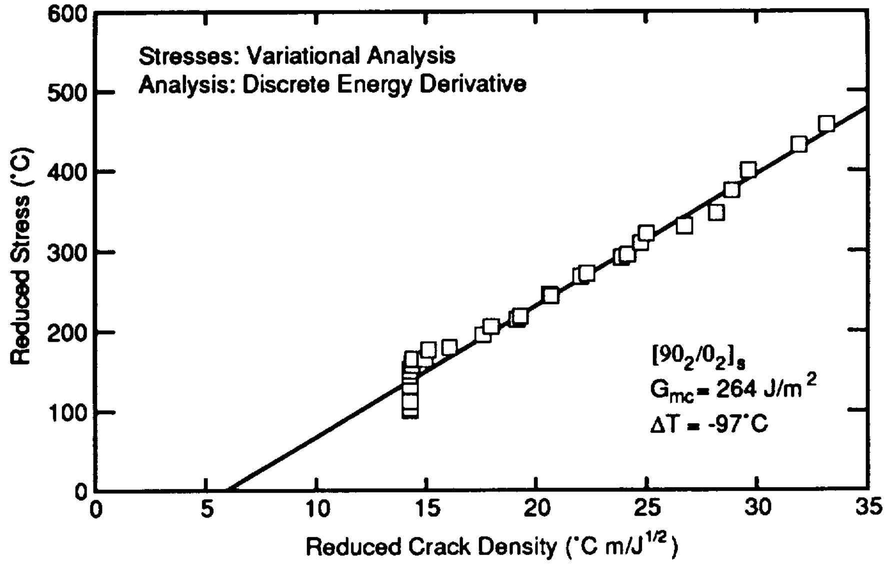

Figure 2.12: A master curve analysis of a $[90_2/0_2]_s$ AS4/3501-6 laminate. The energy release rate is calculated with a discrete energy derivative defined by $Y_a(D)$ in Eq. (2.61) using $f = 1.2$.

which leads us to define a reduced crack density for $[90_n/(S)]_s$ laminates as

$$\text{reduced crack density:} \quad D_R = -\frac{1}{k_{th}^{(1)}}\sqrt{\frac{1}{C_{3a}t_1Y_a(D)}} \tag{2.67}$$

For all types of laminates, a plot of σ_R *vs.* D_R defines a master plot for microcracking experiments. If the variational analysis and energy release rate failure criterion are appropriate, a plot of σ_R *vs.* D_R will be linear with slope $\sqrt{G_{mc}}$ and intercept T. Because G_{mc} and T are layup independent material properties, the results from all laminates of a single material with the same processing conditions should fall on the same linear master plot. A critical test of the variational analysis microcracking theory is to determine if the master plot is linear and if all laminates fall on the same line. Furthermore, the resulting slope and intercept should define physically reasonable quantities.

A typical master curve analysis for a single $[90_2/0_2]_s$ laminate is shown in Fig. 2.12. The master plot is linear except for a few points at the lowest reduced crack density. As previously discussed, the low crack density results are affected by processing flaws that are not specifically included in the microcracking analysis [6]. It is not surprising that they deviate from the master curve, and they should be ignored when measuring G_{mc}. The straight line in Fig. 2.12 is the best linear fit

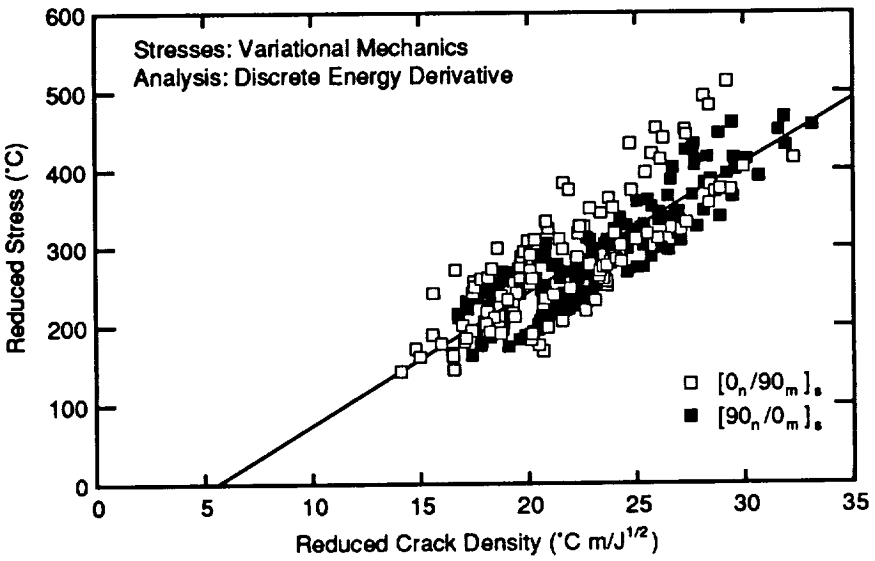

Figure 2.13: A master curve analysis of all AS4/3501-6 laminates. The energy release rate is calculated with a discrete energy derivative defined by $Y(D)$ or $Y_a(D)$ in Eqs. (2.57) and (2.61) using $f = 1.2$. Data for crack densities less than 0.3 mm^{-1} are not included in this plot.

that ignores the low crack density data. The slope gives $G_{mc} = 264$ J/m^2 which agrees with the fits to raw data in the previous section and with the results in other studies [6, 30]. The intercept gives $T = -93$°C, which is a reasonable number and is similar to the previously assumed value of $T = -125$°C [6]. Note that a side benefit of the master curve analysis is that the value of T does not have to be assumed or measured. It can, in effect, be measured by analysis of the microcracking data.

2.4.2 Variational Analysis of All Laminates

Figure 2.13 gives the master plot for the 18 laminates tested in this study. We assumed that $f = 1.2$ for all laminates and we ignored data with crack densities less than 0.3 mm^{-1}. We claim Fig. 2.13 verifies both the validity of an energy release rate failure criterion and the accuracy of the variational analysis calculation of G_m in Eqs. (2.53) and (2.61). There are three facts that support this claim. First, all laminates fall on a single master curve plot within a relatively narrow scatter band. We discuss the scatter more below. Second, the results for $[(S)/90_n]_s$ laminates (open symbols) agree with the results for $[90_n/(S)]_s$ laminates (solid symbols). Thus a single unified analysis can account for both the symmetric damage state in $[(S)/90_n]_s$ laminates and the antisymmetric damage state in $[90_n/(S)]_s$ laminates. Third, the slope and the intercept of the global linear fit in Fig. 2.13 result in $G_{mc} = 279$ J/m^2 and $T = -93$°C. Both of these results are reasonable measured values for these physical quantities.

There is an observable scatter band for the experimental points relative to the global, linear master curve. This scatter band may represent deficiencies in the analysis that need further refinement. Alternatively, we note that the scatter was caused more by a laminate to laminate variation in intercept than by a laminate to laminate variation in slope. It is thus possible that the scatter is due to real variations in T. Physically, $T = T_s - T_0$ and because all laminates were processed under identical conditions, T should be the same for all laminates. T, however, can also be interpreted as the *effective* level of residual thermal stresses. By Eq. (2.2), when $\sigma_0 = 0$ the residual stress in the 90° plies is $\sigma_{xx,th}^{(1)} = k_{th}^{(1)}T$. Although all laminates were processed under identical conditions, the laminates had different thicknesses. If the different thicknesses caused variations in thermal history, it is possible that the level of residual stresses was layup dependent. A layup dependence in T would cause the type of scatter observed in Fig. 2.13.

2.4.3 Master Plot Analysis for Other Microcracking Theories

As discussed in the *Stress Analysis* section, most previous microcracking theories are based on stress analyses that eliminate the z-dependence of the stress state by making various assumptions about the z-direction stress or displacement. We classified these analyses as "one-dimensional" analyses. In this section we develop master plot analysis for one-dimensional analyses and show that all of them give poor results.

Garrett and Bailey [12] postulated that the next microcrack forms when the maximum stress in the 90° plies, which occurs at $\xi = 0$, reaches the transverse strength of those plies. By this failure

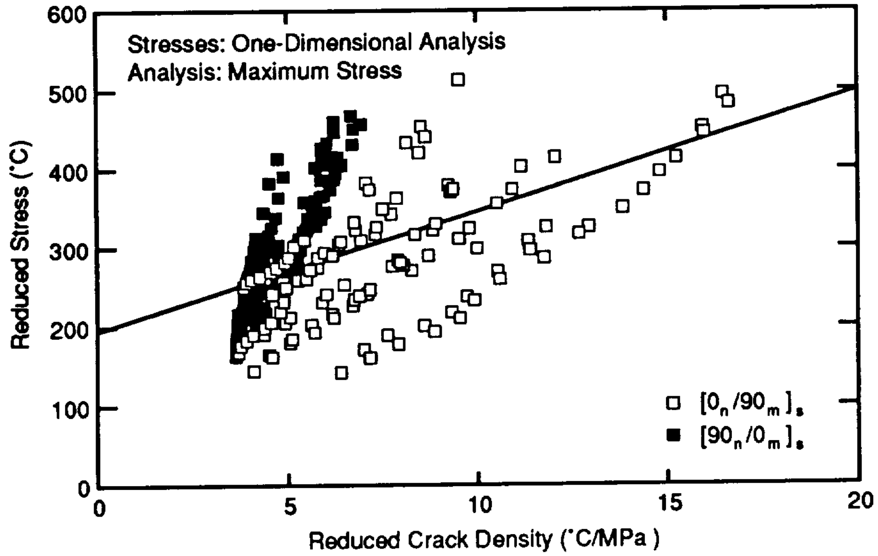

Figure 2.14: A master curve analysis of all AS4/3501-6 laminates using a maximum stress failure criterion and a one-dimensional stress analysis. Data for crack densities less than 0.3 mm^{-1} are not included in this plot.

criterion and the one-dimensional stress analysis, Eqs. (2.2) and (2.15) can be rearranged to give a strength theory master curve

$$-\frac{k_m^{(1)}}{k_{th}^{(1)}}\sigma_0 = -\frac{1}{k_{th}^{(1)}}\frac{\sigma_T}{\left(1-\frac{1}{\cosh\phi\rho}\right)} + T \tag{2.68}$$

where σ_T is the transverse strength of the 90° plies and, as calculated by Garrett and Bailey [12], $\phi = \sqrt{G_{xz}^{(1)}C_1}$. Defining the reduced stress as in Eq. (2.65) and the reduced crack density as

$$\text{reduced crack density}: \qquad D_R = -\frac{1}{k_{th}^{(1)}}\frac{1}{\left(1-\frac{1}{\cosh\phi\rho}\right)}, \tag{2.69}$$

and using a master curve analysis, Eq. (2.68) predicts that a plot of σ_R *vs.* D_R should be linear with slope σ_T and intercept T.

The result of a strength theory analysis applied to our experimental results is in Fig. 2.14. The master curve analysis shows the theory to be very poor. The results from individual laminates are somewhat nonlinear and they do not overlap the results from other laminates. Furthermore, the results from $[(S)/90_n]_s$ (open symbols) and $[90_n/(S)]_s$ (filled symbols) laminates segregate into two groups. This segregation is a characteristic of all one-dimensional analyses. Any analysis that ignores the z-dependence of the stress state will fail to make a distinction between inner and outer 90° ply groups. We therefore conclude that no model based on a one-dimensional stress analysis can successfully predict results for both $[(S)/90_n]_s$ and $[90_n/(S)]_s$ laminates. If we draw a least-squares linear fit through the data in Fig. 2.14, the slope and intercept give $\sigma_T = 15.2$ MPa and $T = +192$°C. These results are unreasonable because the transverse tensile strength of AS4/3501-6 laminates is higher than 15.2 MPa and T should be below zero for laminates that were cooled after processing.

There are two problems with the Garrett and Bailey [12] model. First, it uses a one-dimensional, shear-lag stress analysis. Second it uses a poor failure criterion. To investigate the limitations of the stress analysis, we implemented the strength model using the two-dimensional, variational analysis. This approach still gave poor results. The poor results with the more accurate stress analysis suggest that it is the use of a strength failure criterion that is the more serious and fundamental problem with this analysis. There have been some attempts to develop more sophisticated strength models, such as probabilistic strength models [20, 32, 31, 53, 64]. As discussed before, however, these models have been found to require *in situ* laminate strength properties and therefore would also give poor master plots [51]. We suggest that strength models cannot adequately predict failure in composite laminates.

Because of the problems with all strength analyses, numerous authors suggested energy failure criteria for predicting microcracking [5, 6, 8, 10, 14, 16, 28, 25, 51, 54–56, 58]. Caslini *et. al.* [25] were the first to suggest using total microcrack energy release rate to predict microcrack density as a function of applied load. They used a one-dimensional analysis that assumes parabolic displacements in the 90° plies [42, 43] to express the structural modulus as a function of crack density. They treated crack area, $A = 2t_1WLD$, as a continuous variable and differentiated the modulus expression to find energy release rate. Because they take an analytical derivative as

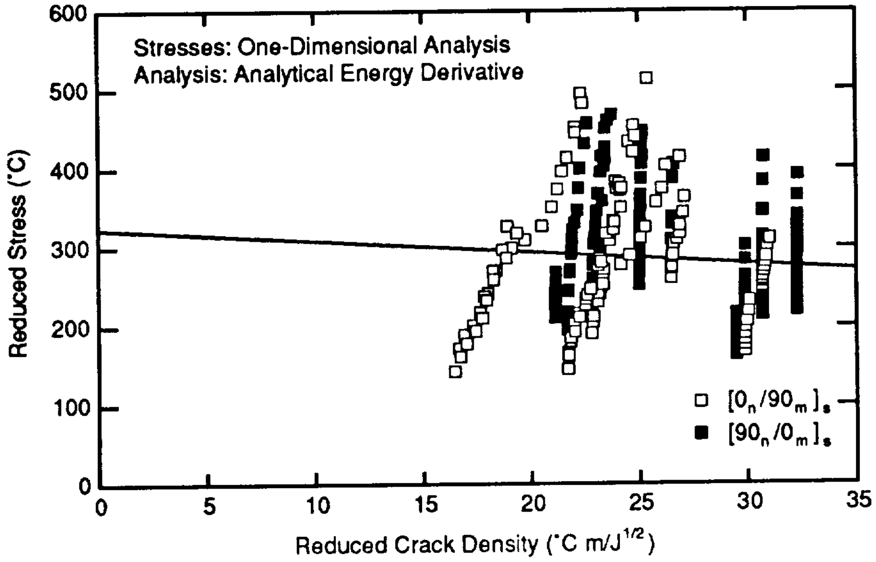

Figure 2.15: A master curve analysis of all AS4/3501-6 laminates using an analytical derivative energy release rate failure criterion and a one-dimensional stress analysis. Data for crack densities less than 0.3 mm^{-1} are not included in this plot.

a function of crack area, we refer to this approach as the "analytical derivative approach." By treating Eq. (2.53) as a definition of $Y(D)$, the Caslini *et. al.* [25] result for G_m can be expressed using

$$Y_{1D,a}(D) = \frac{C_1}{C_3\phi}\left(\tanh\phi\rho - \Phi\rho\,\mathrm{sech}^2\phi\rho\right) \tag{2.70}$$

where subscript "$1D,a$" denotes one-dimensional stress analysis and an analytical derivative approach, and $\phi = \sqrt{3G_{xz}^{(1)}C_1}$. Han *et. al.* [54, 55] describe a similar analysis, but used crack-close methods to calculate G_m. Because their results are identical to those of Caslini *et. al.* [25], the Han *et. al.* [54, 55] approach is also an analytical derivative model.

By replacing $Y(D)$ with $Y_{1D,a}(D)$ we can evaluate the microcracking models in Refs. [25, 54, 55]. The results of such an analysis applied to our experimental results are in Fig. 2.15. This master curve analysis was the worst of any model we evaluated. The results from individual laminates are fairly linear but they give slopes and intercepts corresponding to toughnesses as high as 10^{12} J/m^2 and T's that imply specimen temperatures well below absolute zero. These are clearly unreasonable results. The least-squares linear fit through the data in Fig. 2.15 gives G_{mc} = 2 J/m^2 and T =

323°C. The global fit does not pass through the data (because the data from different laminates do not overlap) and the global fitting constants are unrealistic.

Earlier in this chapter, we argued that Caslini *et. al.*'s [25] original suggestion about analyzing microcracking using energy release rate is appropriate. We are left with explaining why their energy release rate approach is a complete failure. Our first attempt was to use the variational mechanics stress analysis and calculate G_m by a similar analytical derivative approach. This made slight improvements in the master curve but the overall quality and the fitting constants were still unsatisfactory. We suggest instead that the analytical derivative approach is non-physical and therefore $Y_{1D,a}(D)$ gives the *wrong* energy release rate. The analytical derivative energy release rate at a given crack density corresponds to the unlikely fracture event whereby all cracks close and then reopen again as periodic cracks with a slightly higher crack density. In real microcracking, one microcrack forms between two existing microcracks. Apparently the energy release rate for this process is dramatically different from that calculated with an analytical derivative.

Laws and Dvorak [56] were the first to suggest modelling the actual fracture process. They calculated the change in energy associated with the formation of a new microcrack between two existing microcracks. Because they model a discrete process, we call their approach the "discrete derivative approach." We cast Laws and Dvorak [56] results in the form of the variational analysis by redefining $Y(D)$ to be

$$Y_{1D,d}(D) = \frac{C_1}{C_3\phi}\left(2\tanh f\phi\rho/2 - \tanh f\phi\rho\right) \tag{2.71}$$

where subscript "$1D, d$" denotes one-dimensional stress analysis and a discrete derivative approach, and f is the factor introduced earlier to account for the tendency of microcracks to prefer larger than average microcrack intervals. Following Reifsnider [36], Laws and Dvorak [56] used a shear-lag analysis that assumes an interlayer of unknown thickness and stiffness between the (S) sublaminate

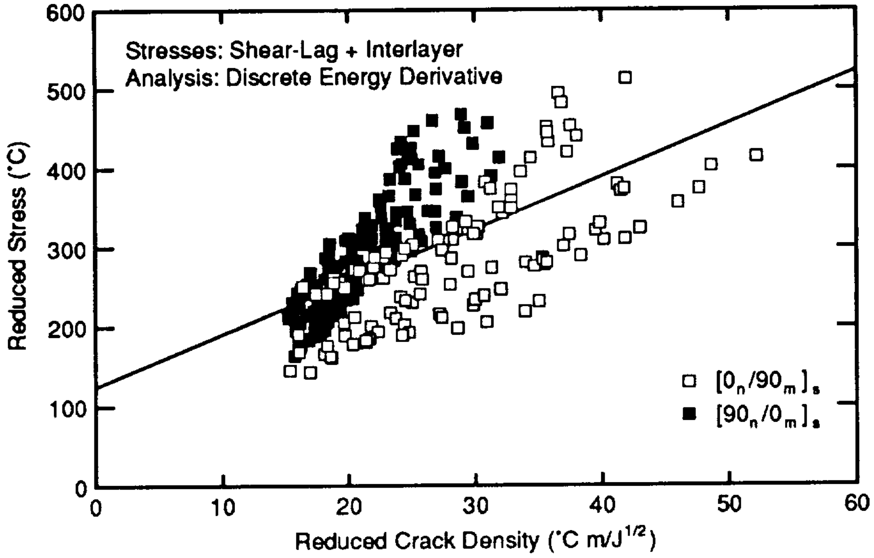

Figure 2.16: A master curve analysis of all AS4/3501-6 laminates using a discrete derivative energy release rate failure criterion and a one-dimensional stress analysis. Data for crack densities less than 0.3 mm^{-1} are not included in this plot.

and the 90° plies. Their ϕ can be expressed as

$$\phi = \sqrt{\frac{Gt_1C_1}{t_0}} \tag{2.72}$$

where G is the shear modulus of the interlayer and t_0 is its thickness.

By replacing $Y(D)$ with $Y_{1D,d}(D)$ we can evaluate the Laws and Dvorak [56] microcracking model. A drawback of their analysis is that the effective stiffness of the interlayer is an unknown parameter. Laws and Dvorak [56] suggested a circular scheme in which G/t_0 is determined by prior knowledge of G_{mc} and the stress required to form the first microcrack. Because of our concern about the sensitivity of low crack density results to laminate processing flaws, we instead used the high crack density results from the single laminate in Fig. 2.12 to determine G/t_0. We varied G/t_0 until the slope of the Laws and Dvorak [56] analysis master curve gave G_{mc} equal to the variational analysis result of 280 J/m^2. This exercise yielded $G/t_0 = 4000$ N/mm, a linear master curve, and an intercept of $T = -73$°C. These initial results were promising. The results of a master plot analysis applied to all our experimental results using $Y_{1D,d}(D)$, $G/t_0 = 4000$ N/mm, and $f \approx 1.2$ are in

Fig. 2.16. This master curve analysis is the most satisfactory of all previous literature models but it still has serious problems. Most importantly, the results from individual lamina do not overlap each other. As is characteristic of one-dimensional analyses, the results from $[(S)/90_n]_s$ and $[90_n/(S)]_s$ laminates segregate into two groups. The least-squares linear fit through the data in Fig. 2.16 gives $G_{mc} = 44$ J/m^2 and $T = +124$°C. The global fit does not pass through the data (because the data from different laminates do not overlap) and the global fitting constants are unrealistic.

We believe the only problem with the Laws and Dvorak [56] analysis is its use of an oversimplified, one-dimensional stress analysis. If their failure criterion is implemented with the variational mechanics stress analysis, the result is equivalent to the analysis first presented by Nairn [5]. As shown in Fig. 2.13, such an analysis gives a good master plot.

It is possible to evaluate many other theories by using master plot analyses. One could combine any failure criterion (strength, analytical derivative G_m, or discrete derivative G_m) with any stress analysis (one-dimensional analyses, two-dimensional variational analyses, refined variational analysis [69], or numerical stress analyses). We tried many such combinations and found that all attempts at using one-dimensional stress analyses are complete failures. If nothing else, they always fail to differentiate between $[(S)/90_n]_s$ and $[90_n/(S)]_s$ laminates. When more accurate stress analyses, such as the variational analysis, are used, all attempts at using strength or analytical derivative G_m failure criteria are also complete failures. We finally concluded that only the specific combination of a sufficiently accurate stress analysis (*e.g.* variational stress analysis) with a discrete derivative evaluation of G_m is capable of producing a meaningful master plot.

2.5 Microcracking Fracture Toughness

2.5.1 Room Temperature Results

The previous sections have shown that the variational analysis and the energy release rate failure criterion can predict all microcracking experiments. One application of the theory is to characterize the toughness of composite materials with respect to microcracking by measuring G_{mc}. G_{mc} can be measured by measuring the microcracking density as a function of load and fitting raw data to the microcracking theory or analyzing the results with a master plot. In this section we discuss the results of measuring G_{mc} for several material systems. Physically, G_{mc} is the energy required to form a complete microcrack or the microcracking fracture toughness. Because microcracks are within a ply group rather than between ply groups, G_{mc} is also an *intralaminar* fracture toughness. The higher the value of G_{mc} for a given composite material, the more resistant that material is to microcracking.

Yalvac *et. al.* [30], and Nairn *et. al.* [6, 8, 70] measured G_{mc} for a variety of materials using the variational mechanics theory (*i.e.* the energy release rates in Eqs. (2.53) and (2.61)). The results are summarized in order of increasing toughness in Table 2.1. The lowest toughness material is AS4/Hercules 3501-6. This material has been reported in four different references and G_{mc} is reproducibly 250±30 J/m^2. The materials with tougher matrices than Hercules 3501-6 epoxy predictably have higher values of G_{mc}. Some examples include the toughened epoxies (IM7/Hercules 8551-7 and T300/Fiberite 977-2), the polycyanate matrices (AS4/Dow polycyanate and G40-800/rubber modified Dow polycyanate), and the thermoplastic matrices (IM6/duPont Avimid® K Polymer and AS4/ICI PEEK). The G_{mc} for the toughened IM7/Hercules 8551-7 is double that of AS4/Hercules 3501-6 but similar in magnitude to other untoughened epoxy systems (e.g. T300/Fiberite 934). The G_{mc}'s for the two toughest materials (T300/Fiberite 977-2 and AS4/ICI PEEK) are based on only a few points and are regarded as approximate [6]. The AS4/PEEK results in Ref. [70] used

Table 2.1: The microcracking fracture toughness, G_{mc}, of several composite material systems. All values of G_{mc} were determined from an energy release rate expression derived from a two-dimensional, variational mechanics analysis

Material	G_{mc} J/m^2	Reference
AS4/Hercules 3501-6	230	30
AS4/Hercules 3501-6	240	6
AS4/Hercules 3501-6	260 ± 20	8
AS4/Hercules 3501-6	279	This report
AS4/Dow Polycyanate	430	30
AS4/Dow Polycyanate	460	30
IM7/Hercules 8551-7	525	30
AS4/Dow Tactix® 556	550	30
T300/Fiberite 934	690	6
G40-800/rubber modified Dow Polycyanate	720	30
AS4/Dow Tactix® 696	825	30
IM6/DuPont Avimid® K Polymer	960	6
AS4/ICI PEEK	1600	70
T300/Fiberite 977-2	1800-2400	6
AS4/ICI PEEK	3000	6

$[90_n/(S)]_s$ laminates and got more data points and probably represent a more reliable measurement of G_{mc}.

The values of G_{mc} are qualitatively similar to delamination fracture toughness (G_{Ic}) measured using double cantilever beam specimens. This correlation is expected because both microcracks and delamination are predominantly mode I crack growth through the matrix. The microcracking and delamination processes differ in detail, however, because microcracking is an *intralaminar* process and delamination is an *interlaminar* process. For at least three materials (AS4/Hercules 3501-6, T300/Fiberite 934, and IM6/duPont Avimid®K Polymer) we have reliable results for both G_{mc} and G_{Ic}. In the two brittle epoxy materials, AS4/Hercules 3501-6 has G_{mc} = 250 J/m^2 and G_{Ic} = 175 J/m^2 [71], and T300/Fiberite 934 has G_{mc} = 690 J/m^2 and G_{Ic} = 140 J/m^2 (John A. Barnes, private communication). In both cases G_{mc} is significantly larger than G_{Ic}. The implication is that cracks propagate more easily between plies than they do within a ply. The higher *intralaminar* toughness may be associated with increased fiber bridging during *intralaminar* fracture [72]. In the thermoplastic composite material (IM6/duPont Avimid®K Polymer), we find the opposite relation. For IM6/duPont Avimid®K Polymer $G_{mc} = 960\ J/m^2$ and $G_{Ic} = 1200\ J/m^2$ [72]. For this material, cracks propagate more easily within plies than between plies. The lower *intralaminar* fracture toughness may reflect the difficulty of achieving complete penetration of the thermoplastic matrix into the carbon fibers of each ply [72].

The above experimental results discuss a new and useful material property—the microcracking or *intralaminar* toughness of a composite material. Although it is truly a measured property, the numerical accuracy of G_{mc} depends on the accuracy of G_m in Eqs. (2.53) and (2.61). To verify the measured G_{mc} by independent experiments, we measured the *transverse* fracture toughness of unidirectional AS4/3501-6 laminates and of IM6/duPont Avimid® K polymer laminates. By *transverse* toughness we mean the material toughness for a crack running parallel to the fibers, but normal to the plies. In other words, the propagation of an *intralaminar* crack. The *transverse* toughness was measured using a conventional double-cantilever beam for delamination specimens and rotating it 90° so that the previous *interlaminar* crack becomes an *intralaminar* crack. The results were analyzed using the DCB specimen analysis recommended by Hashemi *et. al.* [73].

The transverse toughness of Hercules AS4/3501-6 was $G_{tc} = 309$ J/m^2 which is close to the $G_{mc} = 250 \pm 30$ give in Table 1-1. Likewise the transverse toughness of IM6/duPont Avimid® K polymer was $G_{tc} = 1000$ J/m^2 which is close to the the $G_{mc} = 960$ J/m^2 give in Table 1-1. We claim these results support that claim that the experimental technique accurately measures G_{mc}. They further show that *intralaminar* fracture toughness is distinct from *interlaminar* fracture toughness. A complete characterization of the fracture toughness of an advanced composite should consider both failure modes.

The material with the largest discrepancy between G_{mc} and G_{Ic} is T300/Fiberite 934. The microcracking toughness is 2-3 times larger than the delamination fracture toughness. Although we did not measure the transverse toughness of T300/Fiberite 934, it was measured by ICI/Fiberite and found to be $G_{tc} = 590$ J/m^2 (John A. Barnes, private communication). Again, we see that that the transverse toughness is closer to the microcracking toughness than it is to the delamination toughness.

2.5.2 Temperature Dependent Results

To study the effect of residual thermal stresses on microcracking we tested AS4/PEEK laminates at different temperatures. We tested two layups ($[90_4/0]_s$ and $[90_4/0_2]_s$) at three different temperatures (20°C, -10°C, and -50°C). Because we varied temperature, these results cannot be plotted on a single master plot. Both G_{mc} and T may be temperature dependent and thus data from different laminates would fall on lines with different slopes and intercepts. Some analyses of raw data,

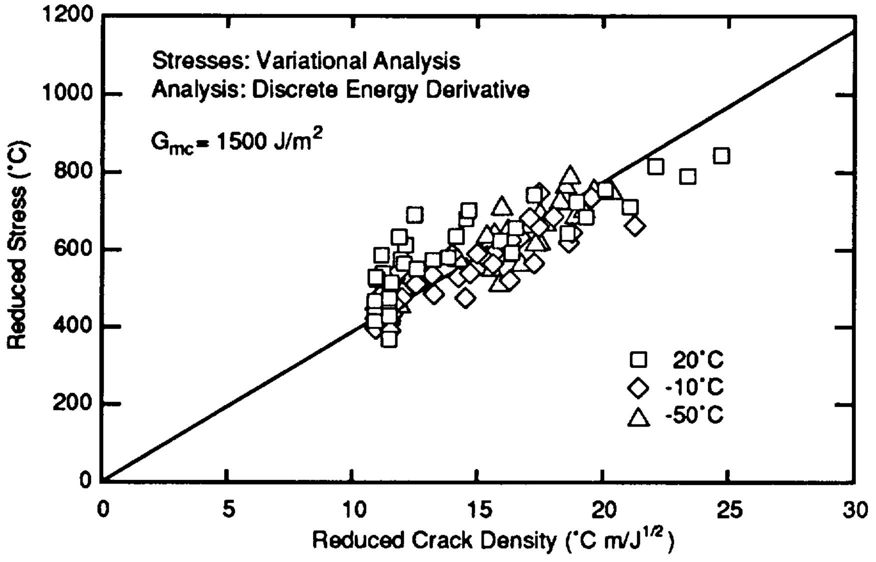

Figure 2.17: A master curve analysis of all AS4/PEEK laminates tested at 20°C, -10°C, and -50°C. The energy release rate is calculated with a discrete energy derivative defined by $Y(D)$ or $Y_a(D)$ in Eqs. (2.57) and (2.61) using $f = 1.2$.

however, using the procedures in the *Microcracking in* $[90_n/(S)]_s$ *Laminates* section indicated that G_{mc} is independent of temperature or only weakly dependent of temperature in the range -50°C to 20°C. The major effect on the microcracking properties therefore arises from changes in the residual thermal stresses or in T. The room temperature experiments could be fit well with $T = -230°\text{C}$, which is similar to the $T = -250°\text{C}$ used by Liu and Nairn [6]. Assuming linear thermoelasticity from -50°C to 20°C, T at -10°C and -50°C should be -260°C and -300°C, respectively. If we accept the previous values of T as reasonable measures of the residual thermal stresses in these laminates, and we assume G_{mc} is independent of temperature, we can propose a residual stress independent master plot. We define a modified reduced stress as

$$\text{modified reduced stress:} \quad \sigma_R' \quad = \quad -\frac{k_m^{(1)}}{k_{th}^{(1)}}\sigma_0 - T \tag{2.73}$$

A plot of σ_R' *vs.* D_R should be linear with a slope of $\sqrt{G_{mc}}$ and pass through the origin.

Figure 2.17 gives the master plot for the two AS4/PEEK laminates tested at each of the three test temperatures. We assumed that $f = 1.2$ for all laminates and we included data at all crack densities. The slope of the best fit line that is forced to pass through the origin gives $G_{mc} = 1500$ J/m^2. The experimental results conform reasonably well to the master line and the results from the different temperatures fall on the same line. Some of the scatter may be caused by temperature variations in G_{mc}, but we do not have enough data to prove of disprove this possibility. A master plot that ignores the change in residual thermal stresses has two to three times the amount of scatter of the master plot in Fig. 2.17. These experiments thus demonstrate the real effect that residual thermal stresses have on microcracking properties of laminates. Finally, we note that previous attempts at studying microcracking in AS4/PEEK laminates used $[(S)/90_n]_s$ layups. The experiments showed only a few microcracks and yielded only a rough estimate of G_{mc} [10]. In this study the 90° plies were on the free surface instead of in the middle. The free-surface plies crack easier and we were thus able to get more experimental results and a more precise determination of G_{mc}. We recommend using $[90_n/(S)]_s$ laminates when studying microcracking in laminates with tough matrices.

2.6 Conclusions

It is relatively easy to fit approximate theories to experimental results from one or two laminates, which is what many researchers do. When theories are required to simultaneously fit results from many different laminates and from many different materials, however, the task is much harder. Our large data base thus allowed us to make critical evaluations of various microcracking theories. We found that of the existing theories, only an energy-based failure criterion implemented using a discrete evaluation of the energy release rate, and a two-dimensional variational stress analysis was capable of analyzing all results. The differences between various theories were best visualized using master plot analyses. Those master plots showed that the differences between the theories are not subtle. All attempts at using one-dimensional stress analyses, regardless of failure criterion, were very poor. Even the more accurate variational stress analysis gave poor results when it was used to predict failure with an inappropriate failure criterion. The variational stress analysis and discrete energy release rate method we recommended can be viewed as not only the best model but also as the only acceptable model. Of course additional models that build on the recommended approach by refining the variational analysis [69] would also produce acceptable results.

A crucial aspect of any microcracking theory is the failure criterion used to generate the predictions. We tried many failure criteria and found that only a fracture mechanics failure criterion based on the actual fracture process provided a fundamental interpretation of all results. The fracture mechanics criterion states that microcracking occurs when the energy release rate associated with the formation of the next microcrack exceeds the microcracking toughness of the material. It is important that the calculated energy release rate corresponds to the actual fracture process. For microcracking this involves modeling the fracture event of a new microcrack forming between two existing microcracks. One approach that ignores the actual fracture process is to treat crack density as a continuous variable and analytically differentiate the strain energy to get a *pseudo*-energy release rate. This analytical derivative approach ignores the actual fracture process and does not agree with experimental results.

Maximum stress or maximum strain failure criteria were particularly bad. Our results substantiate this conclusion for microcracking experiments, but the conclusion is probably more general. We suggest that simple maximum stress or even more sophisticated point stress, average stress, or quadratic failure criteria are not based on energy principles of fracture mechanics, have no fundamental physical basis, and therefore should not be expected to give useful predictions about any composite failure mode. For example, many laminated plate analyses predict the onset of failure using first-ply failure criteria that are based on simple maximum stress rules. The initiation of microcracking in this paper can be viewed as an experimental study on first-ply failure. The inability of strength models to make useful predictions about our experimental results is verification that first-ply failure models are inappropriate. If first-ply failure models are inappropriate, we further suggest that more complicated composite failure theories that are rooted in simple strength rules are equally inappropriate.

We found that a good failure criterion alone is not enough for developing a successful analysis of microcracking. The failure criterion must be used in conjunction with some stress analysis before it can make predictions. That stress analysis must be sufficiently accurate to insure good results. We found, for example, that the qualitative stresses calculated by one-dimensional stress analyses always gave poor results. This result may be surprising to many who previously thought the one-dimensional theories give at least approximate understanding of microcracking. Our new analysis shows that one-dimensional analysis give poor results even when coupled with the best failure criterion such as in the model of Laws and Dvorak [56]. We recommend that all future attempts at using one-dimensional analysis in modeling composite fracture be abandoned.

In contrast, the more accurate two-dimensional, variational stress analysis coupled with the best failure criterion gave good results. If one plots the stresses calculated by a one-dimensional analysis and those calculated by a variational analysis, the differences are marked, but hardly dramatic [51]. We were thus initially surprised by the dramatic differences between the predictions based on the two analyses. A qualitative interpretation of the differences can follow from realizing that fracture is an instability event. When calculating instability processes, minor differences in input stresses can lead to dramatic differences in predictions. In other words, the increased accuracy in the stresses attributed to the variational analysis was crucial to the predictions of microcracking. In contrast, non-instability properties, such as plate stiffness or in-plane displacements, are much easier to predict. Researchers have been mislead into believing that one-dimensional analysis are reasonably accurate due to their ability to predict such non-instability properties.

We close with some general comments about fracture analysis of composite materials. We claim that microcracking, in being controlled by energy release rate, is not a unique composite failure mechanism. Instead, energy release rate is a powerful technique that should be applicable to all composite failure mechanisms. We further suggest that because energy release rate is the fundamental failure criterion, that composite failure models couched in stress-based failure criteria are doomed to inadequacy unless it can be demonstrated mathematically that the stress failure criterion is equivalent to an energy release rate criterion. A similar situation exists in fracture of isotropic, homogeneous materials where a stress criterion or critical stress intensity factor can predict failure because it is exactly related to energy release rate. No one would consider using maximum stress, maximum strain, average stress, point stress, or quadratic stress functions to predict failure in cracked isotropic, homogeneous materials. Likewise, no one should consider using such failure criteria in composite materials.

Chapter 3

MICROCRACKING UNDER FATIGUE LOADS

3.1 Overview

Several investigators have measured the longitudinal stiffness of cross-ply laminates as a function of cycle number during constant load-amplitude fatigue [23, 42, 43]. The goal is to assess the effect of fatigue loading on mechanical properties. Analyzing such fatigue data requires the simultaneous solution of two problems, which are the microcrack density as a function of cycle number and the effect of microcracks on mechanical properties. If attempts to fit experimental results fail, it may not be clear which problem introduces error. Even if data can be fit, it still may not be clear if the physics of the problem is understood or if there is nothing but a fortunate cancelation of errors. The preferred approach is to separate the two problems. The effect of microcrack density on mechanical properties is a micromechanics problem that was discussed in the Stress Analysis section of Chapter 2. The new problem discussed in this chapter is the prediction of the microcrack density as a function of cycle number during fatigue loading.

An important conclusion from Chapter 2, is that variational mechanics analysis gives an accurate energy release rate for the formation of microcracks in cross-ply laminates. In $[(S)/90_n]_s$ laminates the energy release rate is

$$G_m = \sigma_{x0}^{(1)^2} C_3 t_1 Y(D) \tag{3.1}$$

where

$$\sigma_{x0}^{(1)} = k_m^{(1)} \sigma_0 + k_{th}^{(1)} T \tag{3.2}$$

is the stress in the 90° plies before damage, σ_0 is the total applied axial stress, T is the effective residual stress term, C_3 is a constant, t_1 is the semi-thickness of the 90° plies, and $Y(D)$ is a function. C_3 and $Y(D)$ are defined in Chapter 2. An extended variational analysis gives an analogous expression for energy release rate for the formation of microcracking in $[90_n/(S)]_s$ laminates [10]:

$$G_m = \sigma_{x0}^{(1)^2} C_{3a} t_1 Y_a(D) \tag{3.3}$$

where C_{3a} and $Y_a(D)$ are analogs of C_3 and $Y(D)$. They account for the antisymmetric damage state in $[90_n/(S)]_s$ laminates [10].

Equations (3.1) and (3.3) give microcracking energy release rate as a function of applied thermal and mechanical load. A rational procedure for analyzing microcracking damage during fatigue is to use a modified Paris law [74] in which the microcrack density increase per cycle is given by

$$\frac{dD}{dN} = A \Delta G_m^n \tag{3.4}$$

where A and n are two power-law fitting parameters. From any laminate having 90° plies, it is a simple matter to calculate ΔG_m using Eq. (3.1) or Eq. (3.3). If Eq. (3.4) is valid, plotting $\frac{dD}{dN}$ as a function of ΔG on a log-log plot should yield a linear relation. All cross-ply layups of a single material system should fall on the master Paris-law plot.

In this chapter we discuss application of the variational analysis to the interpretation of fatigue experiments. The energy release rate expressions (Eqs. (3.1) and (3.3)) include both mechanical and thermal terms, Therefore, in principle we should be able to interpret mechanical fatigue, thermal cycling fatigue, and combined thermal and mechanical fatigue. Most fatigue data can be analyzed well. There are some important details, however, that precluded the possibility of superposing thermal and mechanical fatigue results on a single Paris-law plot.

3.2 Mechanical Fatigue

We did constant load-amplitude fatigue experiments on various cross-ply laminates of IM6/duPont Avimid® K Polymer laminates and on T300/Fiber 934 laminates. The experimental details are described in Ref. [41]. In this section we summarize the results.

The first problem when analyzing fatigue fracture results is to determine the crack driving force. A difficulty with conventional Paris-law fatigue crack propagation experiments is that during the experiment, both the dependent variable (crack length) and the independent variable (ΔG or ΔK - stress intensity factor) change [74]. A fortunate feature of microcracking fatigue experiments, however, is that the calculated independent variable (ΔG) remains constant up to reasonably high microcrack densities. Figure 3.1 plots ΔG as a function of microcrack density for a typical fatigue experiment on a $[0_2/90_4]_s$ laminate. ΔG is constant up to a microcrack density of about 0.20 mm^{-1} and then drops rapidly to a lower value.

Some typical microcrack densities as a function of cycle number are shown in Fig. 3.1. At low microcrack density, where ΔG is constant, Eq. (3.4) predicts that microcrack density should increase linearly with cycle number $\left(\frac{dD}{dN} = \text{constant}\right)$. The observation is that there is an initial rapid increase in microcrack density that is followed by a slower linear increase in microcrack density. In Fig. 3.1 the slower linear increase is from a microcrack density of 0.13 mm^{-1} to 0.23 mm^{-1}. Liu and Nairn [41] suggested that the initial rapid rise in microcrack density is due to laminate processing flaws and that the slower linear increase is a Paris-law region that characterizes the material's

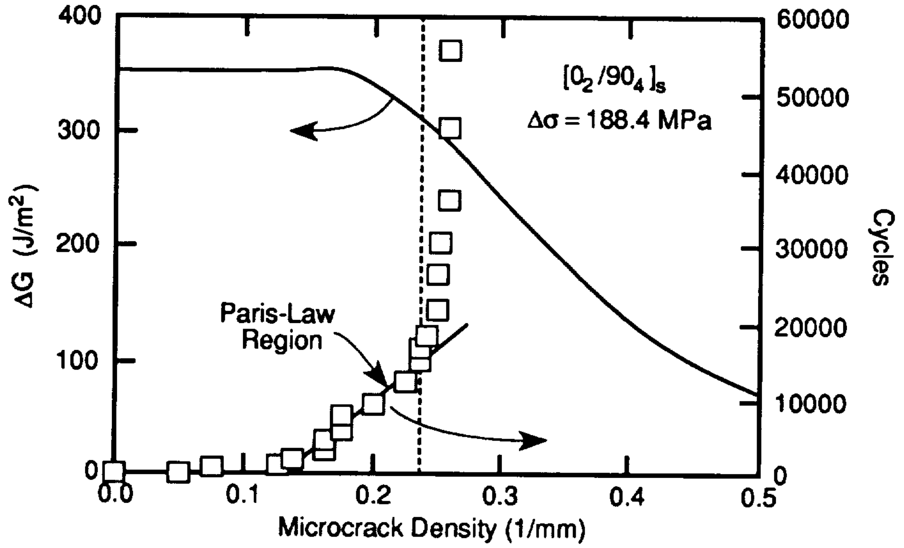

Figure 3.1: Microcracking fatigue data for a $[0_2/90_4]_s$ carbon/epoxy laminate. The solid line shows ΔG as a function of microcrack density. The symbols show the microcrack density as a function of cycle number. The straight line through the microcrack density data shows the Paris-law region of constant microcrack density growth rate.

resistance to fatigue induced microcracking. The suggestion that the initial results are dominated by processing flaws is consistent with the similar observation made during static microcracking experiments [6].

Two experimental observations support the use of the modified Paris-law in Eq. (3.4). First, the rate of increase in microcrack density dramatically decreases at a microcrack density similar to the point where ΔG begins to decrease (see Fig. 3.1). Second, Fig. 3.2 plots the slope of the Paris-law region defined in Fig. 3.1 as a function of ΔG for three different IM6/duPont Avimid® K Polymer laminates. The results for all laminates fall on a single master curve that is linear over a wide range in ΔG. The two points near ΔG = 1000 J/m^2 deviate above the linear Paris-law line which indicates a rapid increase in microcrack density. A rapid increase in microcrack density at this level of ΔG is reasonable because the static microcracking toughness of this material is G_{mc} = 960 J/m^2 [6]. The lowest ΔG point deviates below the linear Paris-law and may be an indication of a threshold limit.

In summary, the variational energy release rate analysis is useful in analyzing mechanical fatigue

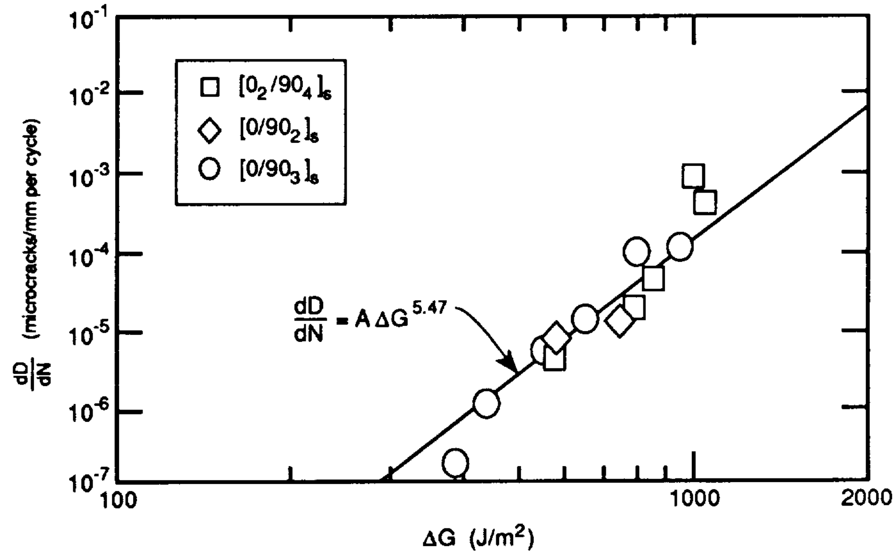

Figure 3.2: The microcrack density growth rate (in microcracks per mm per cycle) as a function of applied ΔG for Avimid® K Polymer/IM6 laminates. As indicated on the figure, the results are from three different cross-ply layups.

experiments. The results in Fig. 3.2 along with similar results for T300/Fiberite 934 in Ref. [41] show that all results for a single material fall on a master Paris-law plot. In other words the Paris-law plot can be viewed as a characterization of a material's resistance to fatigue induced microcracking. The plots from two materials can be used to rank materials. In conjunction with stiffness loss equations and loss limits, the Paris law plot can be used to predict fatigue lifetimes.

3.3 Thermal Cycling

A similar Paris-law analysis can also be applied to thermal cycling fatigue experiments or to combined thermal and mechanical fatigue. Whatever the loading conditions are, Eqs. (3.1) and (3.3) can be used to calculate ΔG. For example, during thermal cycling

$$\Delta G = G_m(T_{min}) - G_m(T_{max}) \tag{3.5}$$

where T_{min} and T_{max} are the minimum and maximum temperatures of the thermal cycle. We built a computer controlled thermal cycling chamber that can do thermal cycling experiments It was

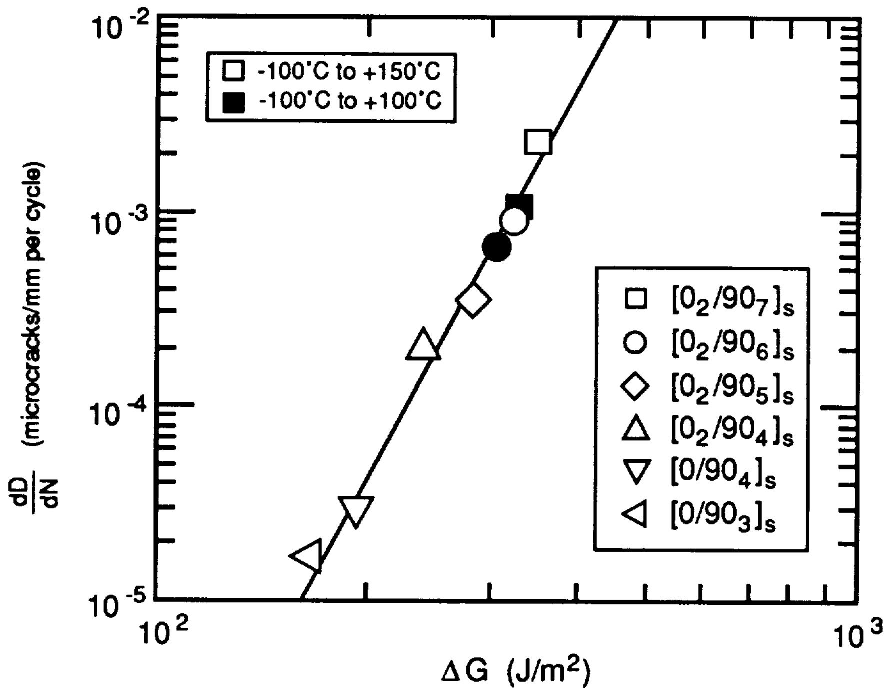

Figure 3.3: The microcrack density growth rate (in microcracks/mm per cycle) as a function of applied ΔG for AS4/Hercules 3501-6 during thermal cycling. As indicated on the figure, the results are from six different cross-ply layups and from two different thermal cycling temperature ranges.

used to test the ability of the variational analysis to correlate thermal cycling data from different laminates.

We tested the modified Paris-law on six different $[0_m/90_n]_s$ layups of Hercules AS4/3501-6 graphite/epoxy composites. As seen in Fig. 3.3, all laminates fall on the the same Paris-law line. We must emphasize that the data is from many different layups. Furthermore, the thermal cycling was between −150°C and +150°C or between −100°C and +150°C. Some samples were dead weight loaded and some were tested unloaded. Despite the variety of layups and loading conditions, all results can be interpreted with a single curve. The Paris-law analysis gives a universal curve that characterizes a given material's resistance to thermally induced microcracking damage. The Paris-law curve should therefore be viewed as a useful, layup independent, material toughness parameter.

We did similar thermal cycling experiments on Fiberite T300/934 graphite/epoxy composites. The thermal cycling results are plotted in Fig. 3.4. Also plotted in Fig. 3.4 are our mechanical

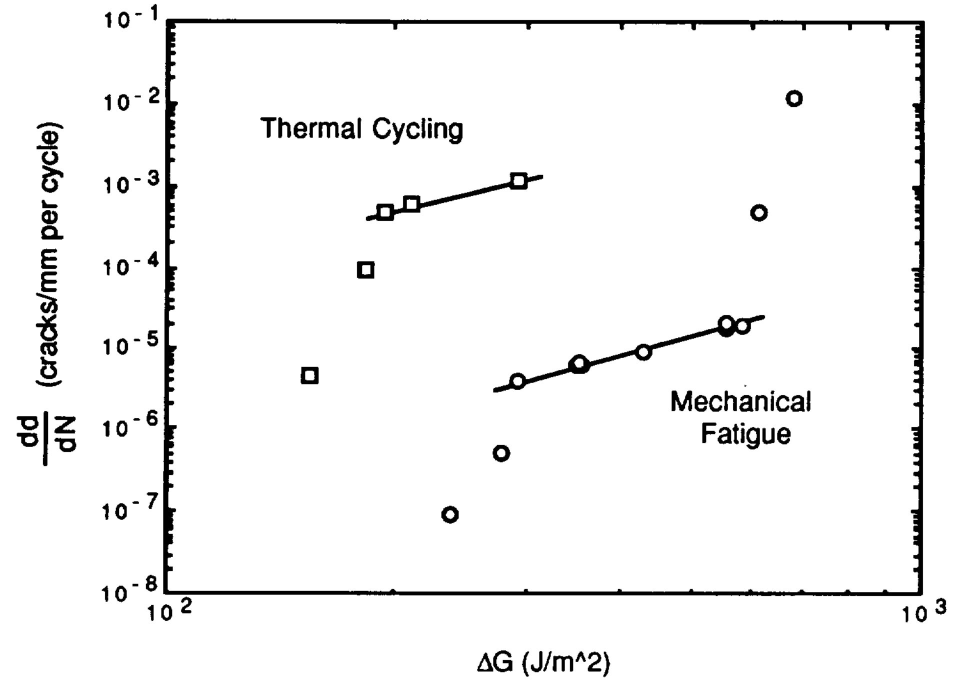

Figure 3.4: Thermal cycling and mechanical fatigue results for Fiberite T300/934 graphite/epoxy laminates. The straight lines indicate regions of Paris-law behavior.

fatigue results [41]. Both the thermal cycling results and the mechanical fatigue results show evidence of a threshold limit. Below the threshold ΔG the crack density growth rate decreases rapidly. Above the threshold limit the crack density growth follows a Paris law. At high ΔG the mechanical fatigue tests show a rapid increase in growth rate. This rapid increase occurs when ΔG reaches the G_c for this material system of 690 J/m^2 [6].

An important question is whether thermal cycling fatigue results can be correlated with mechanical fatigue results? The results in Fig. 3.4 are not the same for thermal *vs.* mechanical loading, although they do parallel each other. In the thermal cycling experiments, the cracks probably form at the maximum stress intensity or at the maximum energy release rate. The maximum energy release rate occurs when the temperature is at the low temperature end of the thermal cycle or between -100°C and -150°C. The thermal cycling fatigue experiments should thus be viewed as fatigue damage induced at low temperatures. In contrast, the mechanical fatigue experiments should be

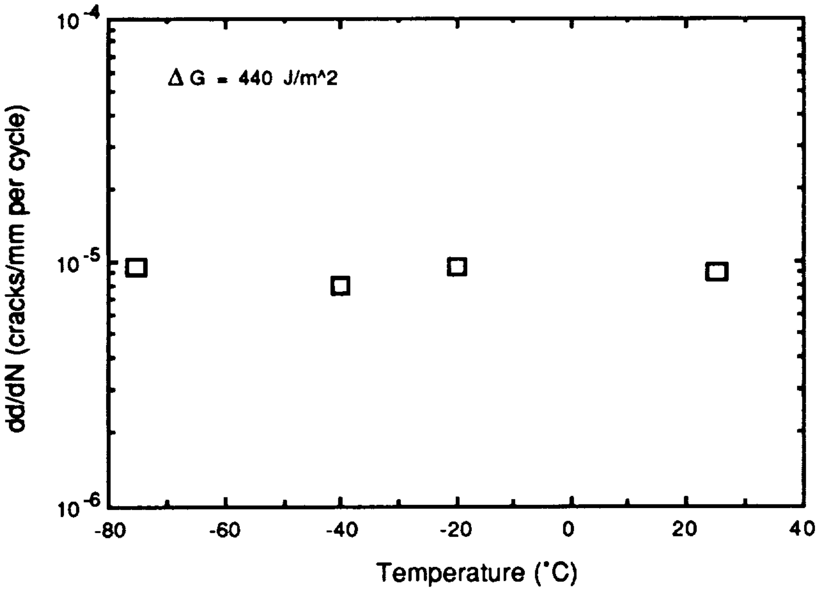

Figure 3.5: Mechanical fatigue results for Fiberite T300/934 graphite/epoxy laminates as a function of test temperature.

viewed as fatigue damage induced at room temperature. It is possible that the shift of the thermal cycling results to more rapid crack growth rates is a consequence of them being low temperature *vs.* room temperature results.

To test the hypothesis in the previous paragraph, we did low temperature mechanical fatigue tests on T300/Fiberite 934 composites. The results of several low-temperature fatigue experiments are in Fig. 3.5. From room temperature down to −75°C, the mechanical fatigue experiments were independent of temperature which is inconsistent with the increase in rate of fatigue damage observed during thermal cycling. There are two possible explanations. First, the hypothesis from the previous paragraph may be wrong. There instead must be some other mechanism that causes thermal cycling induced damage to occur more rapidly than mechanical fatigue induced damage. Second, there may be an abrupt transition at low temperature that eventually results in a coincidence of thermal cycling and mechanical fatigue results. We could not test this second possibility because of limited cooling capabilities in the environmental chamber on our MTS fatigue frame.

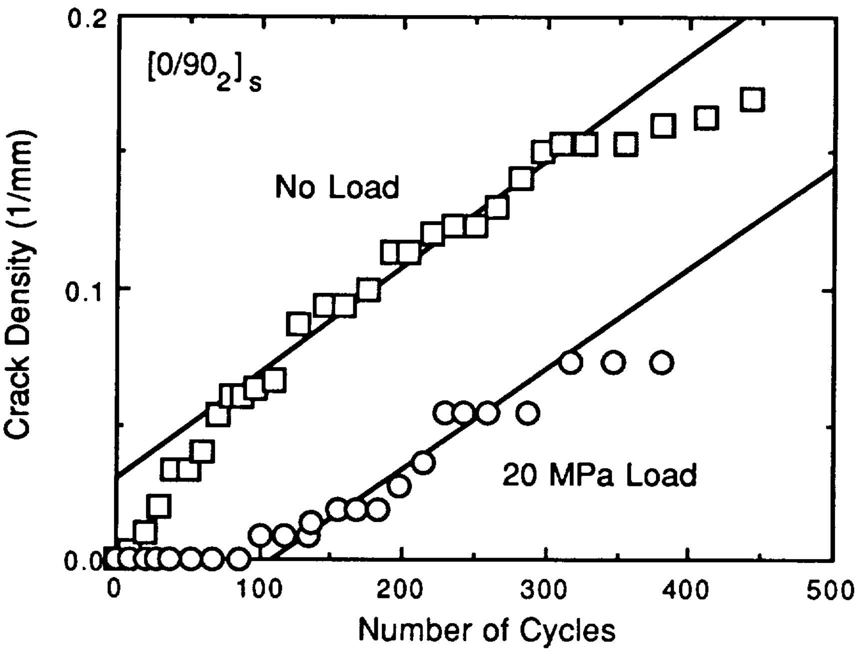

Figure 3.6: Crack density (in cracks per mm) as a function of number of thermal cycles for thermal cycling of an unloaded and of a 20 MPa loaded Hercules 3501-6 epoxy/AS4 graphite laminates. Thermal cycling was between -100°C and +150°C.

3.4 Combined Mechanical and Thermal Fatigue

To test the effect of combined mechanical and thermal loading we did some preliminary thermal cycling experiments in which the sample was simultaneously dead-weight loaded. The typical experimental results in Fig. 3.6 show a surprising result. The raw data in Fig. 3.6 shows that the application of axial load *retards* the formation of microcracks. This observation is at odds with the Paris-law (Eq. (3.4)). An axial load increases ΔG_m and therefore the rate of microcracking formation should increase. Once the microcracks begin to form the crack formation rate or the slope of the crack density *vs.* cycle number plot is slightly larger for the sample with load than for the sample without load. This result agrees with the Paris law analysis. There is, however, no obvious explanation of the low-cycle results.

One possible hypothesis is that the dead-weight load effect results from a stress-activated cure of the epoxy matrix. Epoxy cure reactions are ring-opening reactions. It is reasonable to expect,

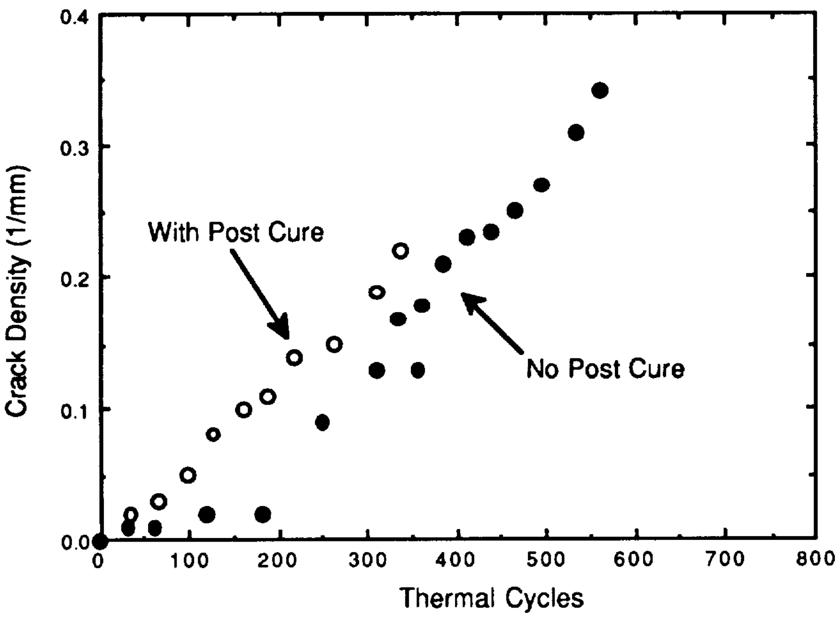

Figure 3.7: Crack density (in cracks per mm) as a function of number of thermal cycles for thermal cycling of 50 lb loaded Hercules 3501-6 epoxy/AS4 graphite laminates. Thermal cycling was between -100°C and +150°C. One sample was post cured on the first thermal cycle by holding at +170°C for 2 hours. The other sample was not post cured.

by Le Chatelier's principle, that an applied tensile load will enhance the cure reaction. It is thus possible that the applied stress induces post-cure reactions when the temperature is at the high-temperature end of each thermal cycle. Such post cure might "heal" laminate flaws and thereby retard the formation of microcracks. There are two ways to test this hypothesis. First we could do thermal cycling on thermoplastic matrices that have no possibility of stress-activated chemical reactions. Second, we could post cure epoxy matrix composites before thermal cycling and look for a reduction or elimination of the applied load effect. We did experiments on post cured epoxy matrix composites.

Our first experiments were on AS4/3501-6 laminates. The results were very dependent on the post cure conditions. The best results were obtained by post curing under load in the thermal cycling chamber at +170°C. In effect we cycle up to high temperature and hold for 2 hours. These samples were then thermal cycled under applied load and compared to an identically prepared

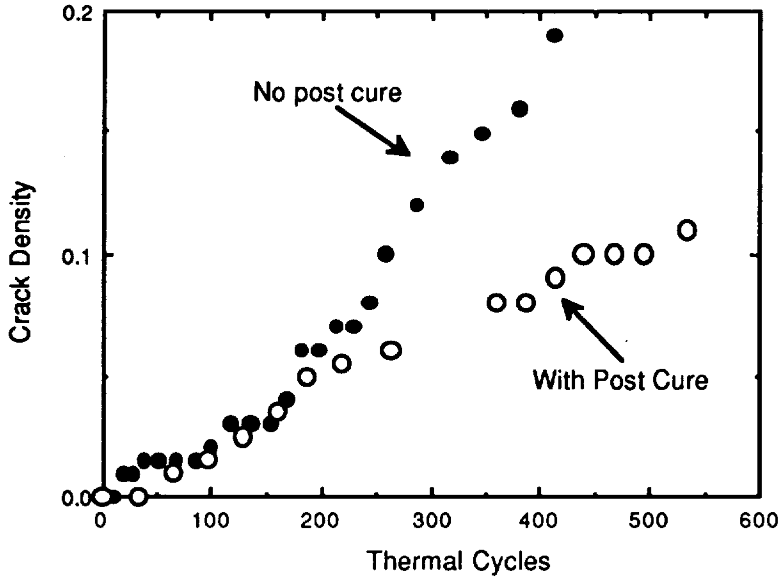

Figure 3.8: Crack density (in cracks per mm) as a function of number of thermal cycles for thermal cycling of 50 lb loaded T300 graphite/Fiberite 934 epoxy laminates. Thermal cycling was between -100°C and +150°C. One sample was post cured on the first thermal cycle by holding at +170°C for 2 hours. The other sample was not post cured.

sample whose only difference was that there was no hold time on the first thermal cycle. Some typical results are in Fig. 3.7. The post cured sample showed no lag in the onset of microcracking. We suggest that the post cured samples were completely cured and thus had no potential for additional cure during the thermal cycling experiment. In the specimens that were not post cured, initial flaws that developed during early thermal cycles may be "healed" by additional cure. The "healing" of the initial flaws delays the onset of microcracking. In contrast, when initial flaws cannot be "healed" the crack density begins to increase in the first few thermal cycles. The final slopes of the crack density *vs.* thermal cycles plot were similar for the post cured and the non-post cured samples. The post cure thus had little effect on the inherent microcracking toughness of the laminates. It only affected the initial flaw "healing" mechanism.

Some similar experimental results for T300/Fiberite 934 are given in Fig. 3.8. At first these results seemed contradictory to the AS4/3501-6 results. There was little difference between the two laminates during early thermal cycles while there was a considerable difference in the final slopes.

We suggest that the post cure process had two effects on these laminates. First, it eliminated the "healing" mechanism as observed for AS4/3501-6. Second, it improved the microcracking toughness. The improvement in toughness caused the slope of the post-cured sample results to be lower. If we extrapolate the high cycle results (data at more than 200 cycles) back to zero crack density, the non-post cured sample shows an intercept of about 100 cycles which indicates a significant delay in the onset of microcracking. In contrast the post-cured sample extrapolates to near zero cycles which indicates little or no delay in the onset of microcracking. In brief, the effect of post cure on the "healing" mechanism in T300/934 laminates was real, but it was masked by a simultaneous improvement in the inherent microcracking toughness effected by the post curing process.

In conclusion, our post curing experiments are consistent with the hypothesis that the observed delay in the onset of microcracking in loaded specimens is due to a stress-activated post curing process that is capable of "healing" laminate flaws caused by the early thermal cycles. Post curing eliminates the initial lag. Post curing may additionally affect the inherent resistance of the material to thermal cycling fatigue damage. Our post cure had no effect on the inherent fatigue damage rate in AS4/3501-6 laminates, but significantly improved it in T300/934 laminates.

3.5 Conclusions

During static tests (see Chapter 2), the variational analysis was shown to accurately give the energy release rate associated with the formation of microcracking in the 90° plies of composite laminates. In this chapter, we showed that the same energy release rate analysis can be used to analyze fatigue experiments. In brief, the energy release rate expression was used to find ΔG_m during fatigue cycling and the fatigue results were interpreted by plotting crack density growth rate as a function of ΔG_m. Out findings were that the results from many different layups for a single material fall on the same dD/dN *vs.* ΔG_m curve. We claim that such a curve characterizes that materials resistance to fatigue induced microcracking.

We did mechanical fatigue, thermal cycling fatigue, and combined mechanical loading and thermal cycling fatigue. There are many similarities in the results suggesting that the energy release rata analysis can explain them all with a single unified analysis. On closer inspection, however, there are important differences in the thermal cycling results. The differences are probably caused by temperature dependent effects in the material system. For example, we suggested that the effect of adding a dead-weight load during thermal cycling was not simply its effect on ΔG_m. Instead, the dead-weight load influenced the chemistry of the epoxy matrix thereby influencing the fatigue results. To explain all details of thermal cycling, it will first be necessary to study the effect of temperature on composite properties such as toughness and chemical stability. Once these effects are understood, it should be possible to predict fatigue lifetimes for any structure under any combination of thermal and mechanical fatigue loading.

Chapter 4

MICROCRACK-INDUCED DELAMINATION

4.1 Introduction

An important detrimental effect of microcracks is that they promote delamination. Considering the importance of delamination damage, the efforts aimed at explaining microcrack-induced delaminations are limited. O'Brien [75, 76] developed the first analytical method for the energy release rate associated with the growth of microcrack-induced delaminations by using simple load sharing rules and ignoring residual stresses. In regions adjacent to delaminations, the 90° plies are assumed to carry no load and thus the uncracked plies carry proportionately increased loads. In regions where there is no delamination, the stresses in all plies are identical to the stresses in the undamaged state. The resulting energy release rate is [75, 76]:

$$G_d = \frac{\sigma_0^2 B^2}{4}\left(\frac{1}{2t_2 E_x^{(2)}} - \frac{1}{BE_c^0}\right) \tag{4.1}$$

where subscript d denotes delamination. This G_d is independent of delamination size and is shown in subsequent calculations to be in reasonable agreement with three-dimensional finite element analysis [62]. Because stresses in regions where there is no delamination are assumed to be the same as that of the undamaged laminate, O'Brien's result is a limiting special case that applies to delaminations induced by isolated microcracks [9]. Experimental observations, however, show that microcrack-induced delaminations usually do not appear until after the formation of many microcracks [27, 37]. Thus, instead of analyzing delaminations induced by isolated microcracks, it is important to consider delaminations induced by microcracks in the proximity of neighboring microcracks.

Dharani and Tang [77] described a consistent shear-lag theory analysis for both microcracking and microcrack-induced delaminations. They predict failure using numerical stress calculations and a point-stress failure criterion. Many of their predictions are in qualitative agreement with experimental results. Like O'Brien's analysis [75, 76], however, Dharani and Tang's delamination study is limited to delamination at isolated microcracks.

Several authors did three-dimensional finite element analyses for free-edge and microcrack-induced delaminations [28, 62, 63]. Fish and Lee [63] considered delaminations near the free edge that are inclined 45° with respect to the microcrack. The crack shape they assumed is reasonable for free-edge delaminations in the absence of microcracks but is not a good representation of microcrack-induced delaminations (see Refs. [27] and [37]). Wang *et. al.* [28] assumed a specific delamination growth process and calculated the energy released as the delamination grows. Because they assumed a specific growth process, their results are only useful in a qualitative sense. Salpekar and O'Brien [62] presented the most comprehensive results including 45° inclined crack fronts, 10.6° inclined crack fronts, and through-the-width delaminations. They calculated mode I, mode II, and mode III energy release rates as functions of position along the various crack fronts. In general, the three-dimensional finite element analyses provide important information about edge effects that cannot be learned from two-dimensional analyses. Their practical utility is limited, however, because by restricting the models to isolated microcracks they fail to account for the effect of neighboring microcracks.

We extended the variational analysis of microcracking to include delaminations emanating from the microcracking tips. We thus derived an analytical, variational mechanics analysis for the stresses in the presence of microcracking and delamination damage. The analysis works for any microcrack spacing and is not limited to isolated microcracks. In this chapter, we describe the variational analysis and calculation of the energy release rate for growth of a delaminations. There are relatively few experimental results on microcrack-induced delaminations. The variational analysis, however, is consistent with those available experimental results.

4.2 Variational Analysis of Delaminations

To analyze microcrack-induced delaminations, we extended the variational analysis of microcracking in 90° plies [1, 2, 5, 6, 10] to account for delaminations emanating from microcrack tips. Figure 4.1 shows two microcracks having delaminations of length d_1 and d_2 emanating from the top and bottom microcrack tips. As implied by Fig. 4.1, we only considered $[(S)/90_n]_s$ laminates. Applying Hashin's [1, 2] only assumption that $\sigma_{xx}^{(i)}$ is independent of z, the stresses in regions I and III of Fig. 4.1 reduce to a simple stress state. The 90° plies carry no load and the (S) sublaminate carries the load lost by the 90° plies in simple uniaxial tension. In regions I and III, the stresses reduce to [9]:

$$\begin{aligned}
\sigma_{xx}^{(1)} &= 0 & \sigma_{xx}^{(2)} &= \sigma_{x0}^{(2)} + \tfrac{\sigma_{x0}^{(1)}}{\lambda} = \tfrac{1+\lambda}{\lambda}\sigma_0 \\
\sigma_{xz}^{(1)} &= \sigma_{zz}^{(1)} = 0 & \sigma_{xz}^{(2)} &= \sigma_{zz}^{(2)} = 0
\end{aligned} \tag{4.2}$$

In region II, the boundary conditions imply the stresses are identical to the stresses that exist between two microcracks separated by a dimensionless half spacing of $\rho - \delta$ instead of the original spacing ρ, where

$$\delta = \frac{d_1 + d_2}{2t_1} \tag{4.3}$$

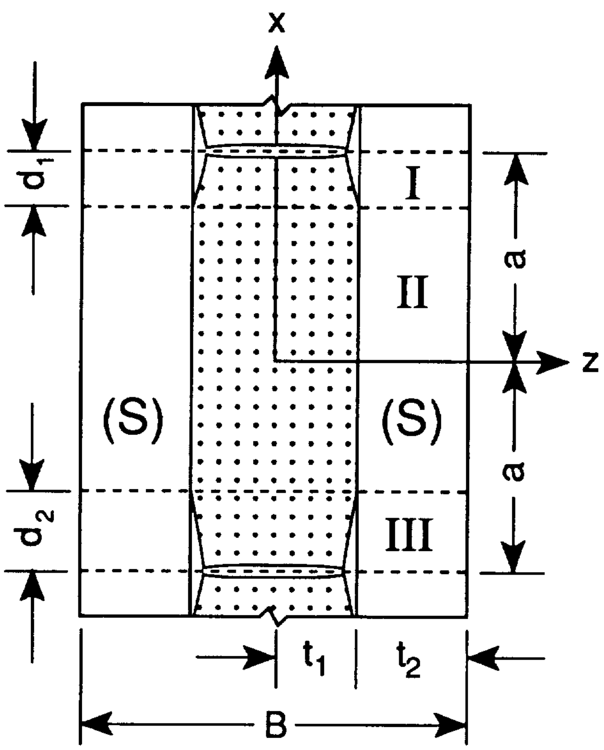

Figure 4.1: Edge view of a $[0_n/90_m]_s$ cross-ply laminate with microcracks and delaminations emanating from the tips of those microcracks. The dashed lines demarcate regions I, II, and III for the stress analysis

Consider a sample having N microcrack intervals characterized by dimensionless spacings ρ_1, ρ_2, $\ldots$, ρ_N and dimensionless delamination lengths δ_1, δ_2, $\ldots$, δ_N. We used the new two-dimensional, variational mechanics stress state in the previous paragraph to find the sample compliance [9]:

$$C = C_0 + \frac{2t_1 E_x^{(1)^2}}{B^2 W E_c^{0^2}} \left(C_3(L-d)\frac{\sum \chi(\rho_i - \delta_i)}{\sum(\rho_i - \delta_i)} + C_1 d \right) \tag{4.4}$$

where d is the sum of the lengths of all delaminations. Knowing all the stresses and the compliance as a function of microcracking and delamination, it is a straightforward problem to calculate the energy release rate for the growth of delamination damage. The details of the calculation are given in Ref. [9]. From that paper, the energy release rate for the growth a single, through-the-width delamination in microcrack interval k is:

$$G_d = \sigma_{x0}^{(1)^2} C_3 t_1 \frac{\chi'(0) - \chi'(\rho_k - \delta_k)}{2} \tag{4.5}$$

The same $\chi(\rho)$ function that appears in the energy release rate expressions for microcrack formation (see Eqs. (2.53) and (2.54)) now appears differentiated in the energy release rate expression for delamination. Unlike O'Brien's [75, 76] simple result, the G_d in Eq. (4.5) depends on delamination size through δ_k. Taking the limit of G_d in Eq. (4.5) as $\rho \to \infty$ and setting $T = 0$ (which appears in $\sigma_{x0}^{(1)}$) gives a result which is the energy release rate for growth of a delamination from an isolated microcrack in the absence of residual thermal stresses; the result is identical to O'Brien's [75, 76] result (see Eq. (4.1)). The new variational mechanics analysis [9] can thus be viewed as a correction to O'Brien's [75, 76] result to account for microcrack growth in small microcrack intervals and to account for thermal stresses.

The variational mechanics delamination analysis can be used to discuss competition between microcracking and delamination and to make comparisons to experimental results. The next section discusses these topics.

4.3 Delamination Predictions

The first form of damage in cross-ply laminates is usually microcracking. Once the first microcrack has formed, we can ask if a delamination will initiate at that microcrack or if instead another microcrack will form. Comparing the energy release rate expression for microcracking (Eq. (2.53)) to the one for delamination (Eq. (4.5)), the predicted failure mode depends on the values of G_{mc} and G_{dc} (the delamination fracture toughness) and on the relative magnitudes of "dimensionless"' energy release rates for microcracking

$$2\chi(\rho/2) - \chi(\rho) \tag{4.6}$$

and for delamination

$$\frac{1}{2}\left(\chi'(0) - \chi'(\rho)\right) \tag{4.7}$$

Assuming for the moment that G_{mc} and G_{dc} are the same (they both represent crack growth through the matrix, albeit possibly by different fracture modes — mode I *vs.* mode II), the predicted failure mode can be determined by plotting the the dimensionless energy release rates as a function of microcracking density. Figure 4.2 gives such a plot for a typical $[0_2/90_4]_s$ carbon/epoxy laminate.

Figure 4.2 shows that at low microcrack densities, microcracking is the preferred mode of failure. At some critical microcrack density (0.51 mm^{-1} in Fig. 4.2), however, the energy release rate for a through-the-width delamination surpasses the energy release rate for microcracking and delaminations are expected to initiate at the microcrack tips. Once delaminations initiate, microcracking will cease and the delaminations will dominate failure. The critical microcrack density for delamination depends on the laminate structure. In agreement with experimental observations [27, 37], the more 90° plies, the lower the critical microcrack density for delamination. In other words, delaminations initiate more easily from microcrack tips in thick 90° ply groups.

Figure 4.3 plots the critical crack density for delamination as a function of the number of 90° plies

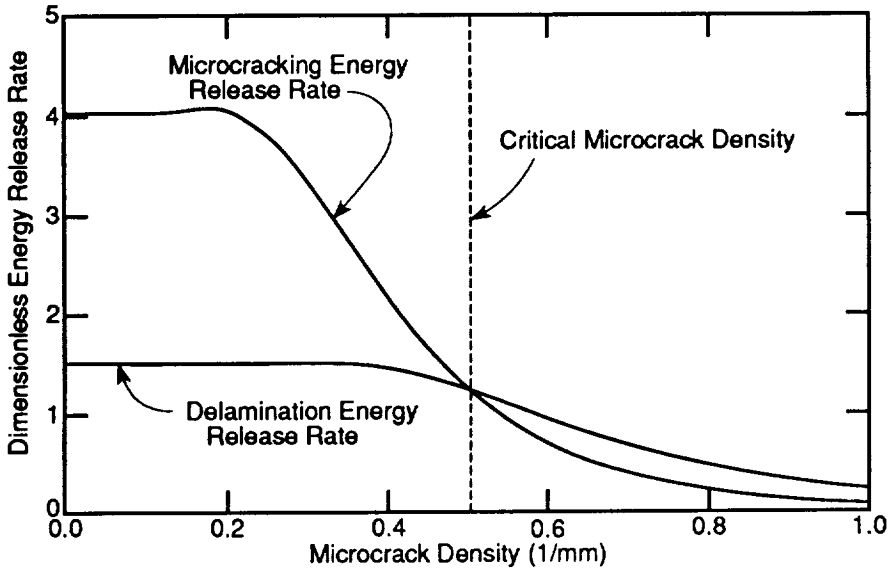

Figure 4.2: Dimensionless energy release rates for initiation of delamination and for continued microcracking as functions of microcrack density for a $[0_2/90_4]_s$ carbon/epoxy laminate. The critical microcrack density for delamination is defined by the microcrack density where the two curves cross.

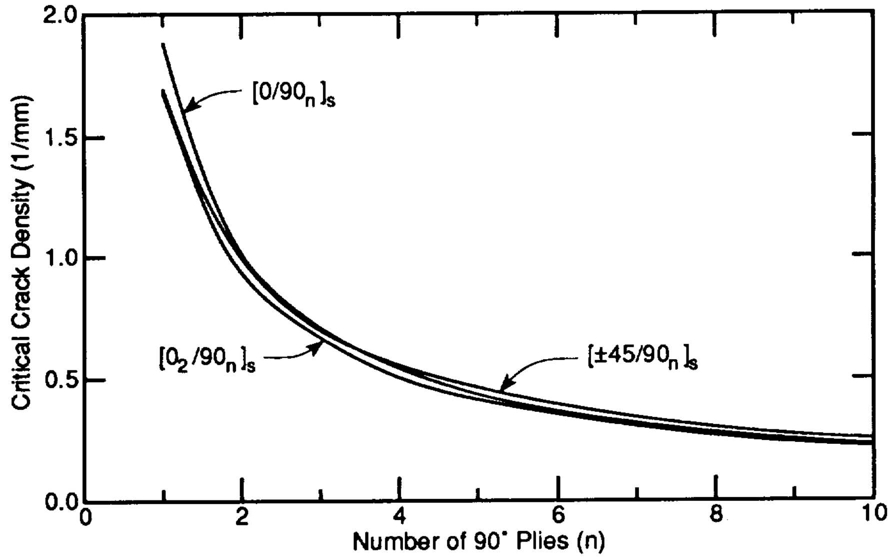

Figure 4.3: The critical crack densities for delamination as functions of the number of 90° plies in half of the symmetric laminate. The three curves are for different (S) sublaminates supporting the 90° plies.

for three different $[(S)/90_n]_s$ laminates. The critical microcrack density is virtually independent of the sublaminate (S) supporting the 90° plies. Although sublaminate (S) has little effect on critical microcrack density, it has a significant effect on the load at which the critical microcrack density is reached. The stiffer the sublaminate (S), the higher the load required to reach a given microcrack density and therefore the higher the load required to induce delamination.

Although we previously assumed that $G_{mc} = G_{dc}$, the conclusions drawn from Fig. 4.2 are easily generalized for $G_{dc} \neq G_{mc}$. We merely need to normalize the dimensionless energy release rates by dividing them by the critical energy release rates. The trends in the dimensionless energy release rates remain the same but one of them (*e.g.* the microcracking energy release rate) moves up or down relative to the other, depending on $G_{mc} < G_{dc}$ or $G_{mc} > G_{dc}$. Consequently the critical microcrack density increases (for $G_{mc} < G_{dc}$) or decreases (for $G_{mc} > G_{dc}$). In the limit of low delamination fracture toughness, the formation of the first microcrack might be immediately followed by initiation of delamination.

4.4 Three-Dimensional Effects

Experimental observations indicate that delamination and its propagation is not a through-the-width process [27, 37]. The delamination analysis problem is thus not two-dimensional. To explain three-dimensional effects, we constructed a quasi-three dimensional analysis using an array of parallel, two-dimensional springs. The details of the analysis are in Ref. [9]. This section discusses the predictions of the quasi-three-dimensional model.

Experimental observations [27, 37] suggest that delaminations initiate at a free-edge with an angled crack front (see Fig. 4.4A). In Fig. 4.5 we use the quasi-three-dimensional analysis of Ref. [9] to plot the energy release rate as a function of position along an angled edge delamination. The sample calculation is for a 12.7 mm wide $[0_2/90_4]_s$ carbon fiber/epoxy laminate with a 45° crack

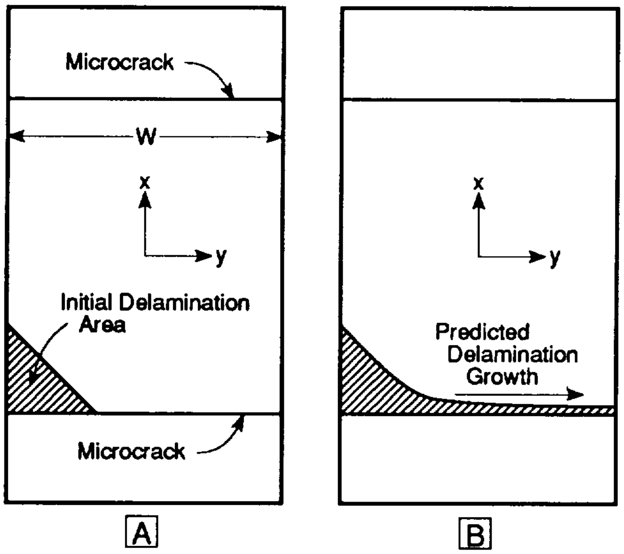

Figure 4.4: A schematic view of the predicted growth of a delamination emanating from a microcrack tip. A. An initial delamination growth with a 45° crack front. B. If a 45° delamination front develops, it would be predicted to grow by extending along the microcrack tip or across the sample width.

front that has grown 1 mm into a microcrack interval in which the microcracks are 2 mm apart. The energy release rate has its minimum at the free-edge, where the axial extent of delamination is the largest, and monotonically increases along the crack front as the axial extent of delamination monotonically decreases. When axial extent of delamination becomes zero the energy release rate reaches a maximum and constant value. Assuming that delamination growth occurs at locations of maximum G_d, the quasi-three-dimensional model implies that delamination growth will proceed from regions where there is currently little or no delamination extending from the tip of the microcrack. As illustrated in Fig. 4.4B, we expect delamination growth to proceed along the microcrack tip. This form of crack growth will be preferred over self-similar propagation of the angled crack front. The predicted crack growth in Fig. 4.4B qualitatively agrees with experimental observations in Refs. [27] and [37].

Two qualifications need to be placed on the predictions of the quasi-three-dimensional model. First, the tendency towards delamination growth from the regions of minimal current delamination is strong only for the small microcrack intervals typical for those beyond the critical crack density for

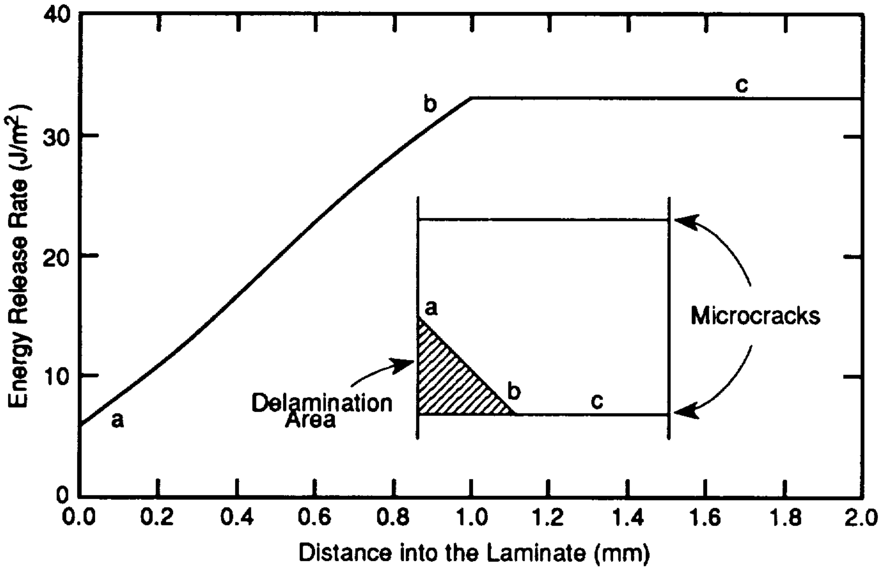

Figure 4.5: The energy release rate for delamination as a function of position along a 45° crack front. The assumed delamination extends 1 mm into a 2 mm microcrack interval. The letters a, b, and c show a position along the crack front and the corresponding position on the energy release rate plot.

delamination. In relatively large microcrack intervals, the energy release rate remains constant over a wide range of initial delamination length and consequently there will be no dominant delamination growth direction [9]. Second, the quasi-three dimensional model cannot account for free-edge interlaminar stresses. Three-dimensional finite element analysis shows that the free-edge stresses increase the loading for mode I fracture near the edge [62]. The increased mode I component may be responsible for the initiation of the delamination and for the initial observation of angled crack fronts. Once delamination growth has proceeded a few ply depths into the laminate, the quasi-three-dimensional analysis described here will provide adequate predictions.

4.5 Delamination in $[90_n/(S)]_s$ Laminates

The delamination analysis and predictions discussed above are for $[(S)/90_n]_s$ laminates or laminates with interior 90° plies. Experimental observations show that laminates with microcracks in outer-ply 90° plies (*e.g.* $[90_n/(S)]_s$ laminates) are more susceptible to microcrack-induced delaminations than the corresponding $[(S)/90_n]_s$ laminate [25, 31, 44]. The variational mechanics analysis of $[90_n/(S)]_s$ laminates described in Chapter 2 and in Ref. [10], explains this increased tendency towards delamination by noting that the asymmetry of the characteristic damage state leads to a bending effect that enhances the mode I character of the delamination process. No one has been able to analytically calculate the energy release rate for delamination in $[90_n/(S)]_s$ laminates. Work in progress shows that the two-dimensional, variational mechanics analysis of $[90_n/(S)]_s$ laminates can be extended to account for delaminations.

4.6 Assessment of Accuracy

We consider the expected accuracy of the variational mechanics analysis of microcrack-induced delaminations. The only approximation made in the analysis is that within the ply groups, $\sigma_{xx}^{(i)}$ are functions of x but independent of z. This approximation is most severe near the microcrack tips and consequently results in expected stress singularities being ignored. Our fracture analysis, however, is not based on crack tip stress state, but rather on global strain energy. Despite missing stress singularities, we claim the global strain energy given in Ref. [9] is sufficiently accurate. There are three pieces of evidence to support this claim. First, all limiting values are correct; *i.e.* the strain energy, modulus, and thermal expansion coefficient all give the correct results in the limit of zero or complete delamination [9]. Second, there are precedents for laminate energy release rate analyses that ignore stress singularities to give accurate results. Two examples are double cantilever beam delamination [78] and edge delamination [79]. We suggest that the approximation used in our delamination analysis is the tensile loading analog of the standard beam theory approximation. This suggestion implies that our results have an accuracy similar to that of beam theories for delamination. The third piece of evidence supporting sufficient accuracy is that all predictions agree, at least qualitatively, with experimental observations. A more quantitative test of the analysis will require more detailed experiment results.

An alternative delamination analysis could be developed using the one-dimensional shear-lag methods discussed in Chapter 2. Like the variational analysis, the one-dimensional models also assume that $\sigma_{xx}^{(i)}$ is a function of x only. Unlike the variational analysis, however, the one-dimensional models make additional assumptions that remove the z coordinate from the analysis and leave the transverse normal stresses undefined. Our new experiments on microcracking show that the extra assumptions render the one-dimensional stress analyses severely inadequate for interpreting microcracking experiments [51]. In contrast, the variational analysis can satisfactorily explain a wide body of microcracking results. We claim that the requirements of an approximate stress analysis for delamination are even more severe. While the validity of the variational approach to delamination remains to be experimentally verified, the likelihood that a one-dimensional shear-lag analysis will provide any useful results is very low.

4.7 Conclusions

We have extended the variational analysis to account for delaminations emanating from the tips of microcracks. The stress analysis was used to calculate the energy release rate for propagation of a microcrack-induced delamination. This analysis along with the stress analysis of $[90_n/(S)]_s$ laminates leads to five important conclusions:

1. Microcracks can induce delaminations but they only initiate after the microcrack density reaches some critical crack density for delamination.
2. The critical crack density for delamination is independent of the supporting sublaminate (S), but it may depend on the relative material toughnesses for the two failure modes of microcracking and delamination.

3. Microcrack-induced delaminations form more easily as the thickness of the 90° plies increases.

4. Delaminations that initiate on a free edge will tend to propagate across the width of the laminate as opposed to propagating axially or parallel to the applied load.

5. $[90_n/(S)]_s$ laminates are more susceptible to microcrack-induced delaminations than the corresponding $[(S)/90_n]_s$ laminate.

All these conclusions agree qualitatively with experimental observations.

To prove the validity of the new delamination analysis it is important to do a quantitative comparison between theory and experiments. These experiments are difficult because microcrack-induced delaminations may form at any microcrack. When there are many microcracks, it is difficult or impossible to watch them all and to observe the delamination process. We suspect that the preferred experiments will be bending experiments on $[90_n/(S)]_s$ laminates. The use of $[90_n/(S)]_s$ laminates will promote the delamination process. The use of bending loads will focus delamination damage into a small region. The only problem is that interpreting the experiments will require some new and non-trivial variational analyses. We recommend that future work include analysis of delamination experiments in $[90_n/(S)]_s$ laminates under bending loads.

Chapter 5

EXTENSIONS TO VARIATIONAL ANALYSIS TECHNIQUES

5.1 Introduction

Chapter 2 showed that a variational stress analysis coupled with a energy release rate failure criterion can explain virtually all the microcracking properties of $[(S)/90_n]_s$ and $[90_n/(S)]_s$ laminates. Chapter 3 showed that the the energy release rate analysis can correlate experimental results during mechanical fatigue, thermal cycling, and combined mechanical loading and thermal cycling. The success of the variational stress analysis and the resulting energy release rate calculations suggests that more work along these lines would produce useful results for explaining composite failures. The first extension of the variational analysis was described in Chapter 4. The variational delamination analysis was found to qualitatively agree with all delamination experimental observations.

In this chapter we describe some additional, albeit less complete, extensions to the variational analysis. The next section discusses curved microcracks. Although we cannot predict the stresses in the presence of curved microcracks, we can predict the geometric effects that lead to the formation of curved microcracks as opposed to straight microcracks. The third section discusses generalizations

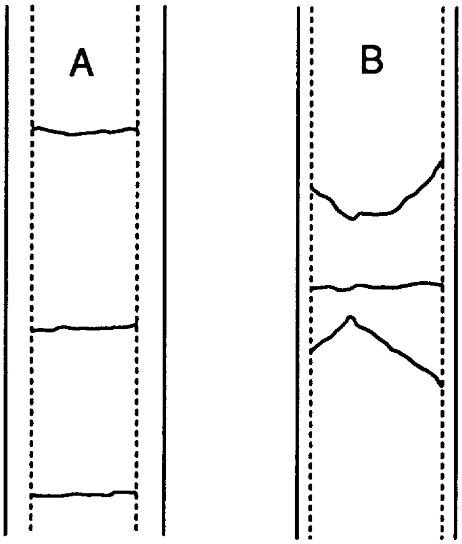

Figure 5.1: Sketches of actual edge view of typically damaged $[(S)/90_n]_s$ laminates. A. Toughly periodic array of straight microcracks in an AS4/PEEK $[0/90_4]_s$ laminate. B. Two curved microcracks near one straight microcrack in an AS4/PEEK $[0/90_8]_s$ laminate.

of the variational analysis. The generalizations are mostly preliminary and presented in an abstract manner. The main purpose of including them in this report is that they illustrate the range of problems that can be solved with the variational stress analysis. Some of the problems can be solved immediately with only minor extensions to the theory. Other problems will require more extensive analysis and perhaps development of numerical methods. The fourth section discusses an axisymmetric variational analysis that gives the stresses around breaks in embedded single fibers. We expect this analysis to be helpful in interpreting interface tests such as single-fiber fragmentation tests [80–83], fiber pull-out tests [84], or microdrop debond tests [85].

5.2 Curved Microcracks

At low microcrack densities microcracks in $[(S)/90_n]_s$ laminates are straight (see Fig. 5.1A). The tendency towards periodic arrays of straight microcracks implies that new microcracks form approximately midway between existing microcracks. At high microcrack densities curved microcracks that make an angle of 40-50° with respect to the $90/(S)$ interface (see Fig. 5.1B) are observed

[12, 15, 24, 33, 34, 86]. Curved microcracks are always associated with existing straight microcracks and form at a position about one-ply thickness away from the straight microcrack [33, 34, 86]. Groves *et. al.* [34] described the only attempt at understanding the mechanism behind curved microcracks. They tried many failure criteria and postulated that curved microcracks form at local maxima in principle stress and that the curvature of the microcracks is determined by the trajectory of the maximum principle stress [34]. Their claims are qualitatively supported by finite element calculations that show a principle stress maximum near existing straight microcracks that occurs near the $90/(S)$ interface. In agreement with experimental observations, the principle stress trajectories at the location of the maximum principle stress make an angle of 40–60° with respect to the $90/(S)$ interface [34]. The location of the principle stress maximum, however, is only in qualitative agreement with experimental observations. The finite element analysis predicts that the maximum principle stress is closer to the straight microcrack than the initiation site of experimentally observed curved microcracks [34].

It is interesting to apply Hashin's [6, 1, 2, 5] two-dimensional, variational mechanics analysis to the prediction of curved microcrack formation using the maximum principle stress model proposed by Groves *et. al.* [34]. There are two goals to this exercise. First, if successful, we have further evidence that the stress components of Hashin's two-dimensional analysis are of sufficient accuracy for the basis of models on composite fracture. Second, we can derive analytical tools that might be useful in understanding curved microcracks.

In the $x - z$ plane, the maximum principle stress is

$$\sigma_{max} = \frac{\sigma_{xx} + \sigma_{zz}}{2} + \sqrt{\left(\frac{\sigma_{xx} - \sigma_{zz}}{2}\right)^2 + \sigma_{xz}^2} \tag{5.1}$$

Applying the two-dimensional, variational mechanics stress state for the 90° plies of $[(S)/90_n]_s$

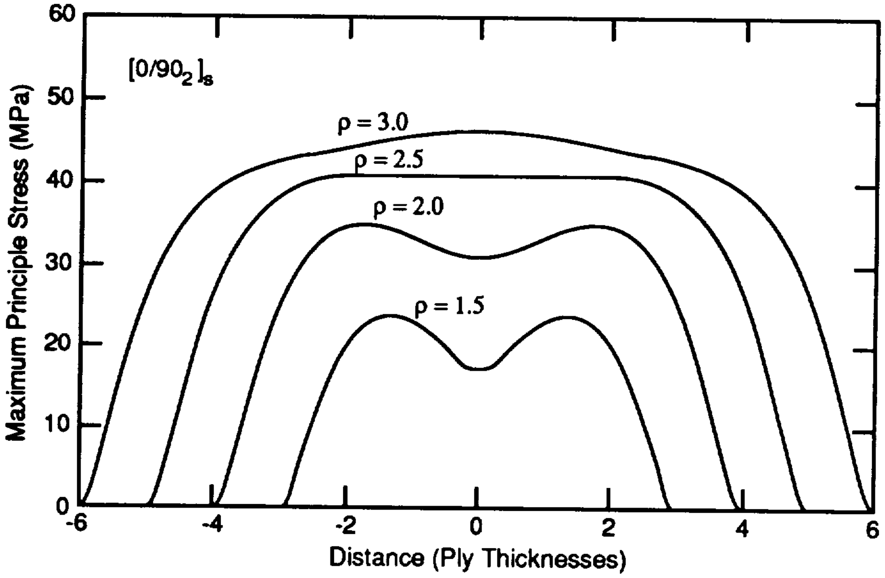

Figure 5.2: The maximum principal stresses along the 0/90 interface in a typical $[0/90_2]_s$ carbon/epoxy laminate for four values of the microcrack spacing. ρ is a dimensionless microcrack spacing defined by $\rho = a/t_1$. The critical crack density is approximately 2.5.

laminates in Eqs. (2.28) and (2.29) gives

$$\sigma_{max} = \frac{k_m^{(1)}\sigma_0 - \psi(x) + \frac{\psi''(x)}{2}(ht_1 - z^2)}{2} + \sqrt{\left(\frac{k_m^{(1)}\sigma_0 - \psi(x) - \frac{\psi''(x)}{2}(ht_1 - z^2)}{2}\right)^2 + \psi'(x)^2 z^2} \quad (5.2)$$

Plotting Eq. (5.2) over the entire 90° ply group shows that the maximum principle stress always occurs at the 90/(S) interface, but its location on the interface depends on the microcrack density and on laminate structure [86]. Figure 5.2 plots the maximum principle stresses along the 90/0 interface of a $[0/90_2]_s$ carbon/epoxy laminate for four different microcrack densities. For low microcrack densities ($\rho \geq 3.0$ in Fig. 5.2) there is a broad maximum in principle stress midway between the two existing microcracks. The principle stress trajectory midway between two existing microcracks is normal to the 90/0 interface. The prediction is that only straight microcracks form when the microcrack density is low. At high microcrack densities ($\rho \leq 2.0$ in Fig. 5.2) there are two local maxima in principle stress. In agreement with experimental observations, the local stress maxima are approximately one to two ply thicknesses away from the existing microcracks. The location of the principle stress maxima is in better agreement with experimental observation than the finite element calculations by Groves *et. al.* [34].

We are enlightened by Fig. 5.2 that for any laminate structure there is some critical microcrack density where the local principle stress maxima near existing microcracks are equal to the local principle stress maximum midway between existing microcracks. For the laminate in Fig. 5.2 the critical microcrack density is when $\rho = 2.5$. When the microcrack density is below the critical microcrack density, straight microcracks midway between existing microcracks will dominate. When the microcrack density is above the critical microcrack density, curved microcracks near existing straight microcracks will dominate. These predictions agree with our new experimental observations [86].

Groves *et. al.* [34] suggested that the shape of curved microcracks can be approximated by the trajectory of the maximum principle stress that exists before the curved microcrack forms. This simple suggestion ignores the effect that a propagating curved microcrack has on principle stress trajectories, but it appears to be qualitatively correct [34]. The maximum principle stress trajectory in the $x - z$ plane can be determined from the differential equation

$$\frac{dz}{dx} = \frac{\sigma_{xx} - \sigma_{zz}}{2\sigma_{xz}} + \sqrt{\left(\frac{\sigma_{xx} - \sigma_{zz}}{2\sigma_{xz}}\right)^2 + 1} \tag{5.3}$$

Substitution of the variational mechanics stress state gives

$$\frac{dz}{dx} = \frac{k_m^{(1)}\sigma_0 - \psi(x) - \frac{\psi''(x)}{2}(ht_1 - z^2)}{2\psi'(x)z} + \sqrt{\left(\frac{k_m^{(1)}\sigma_0 - \psi(x) - \frac{\psi''(x)}{2}(ht_1 - z^2)}{2\psi'(x)z}\right)^2 + 1} \tag{5.4}$$

Numerical integration of Eq. (5.4) starting at the principle stress maximum on the $90/(S)$ interface gives a prediction of the shape of the curved microcracks. Two typical predictions for actual curved microcracks are shown in Fig. 5.3. The initial angle and the overall trajectory are a reasonable agreement with experimental observations [86].

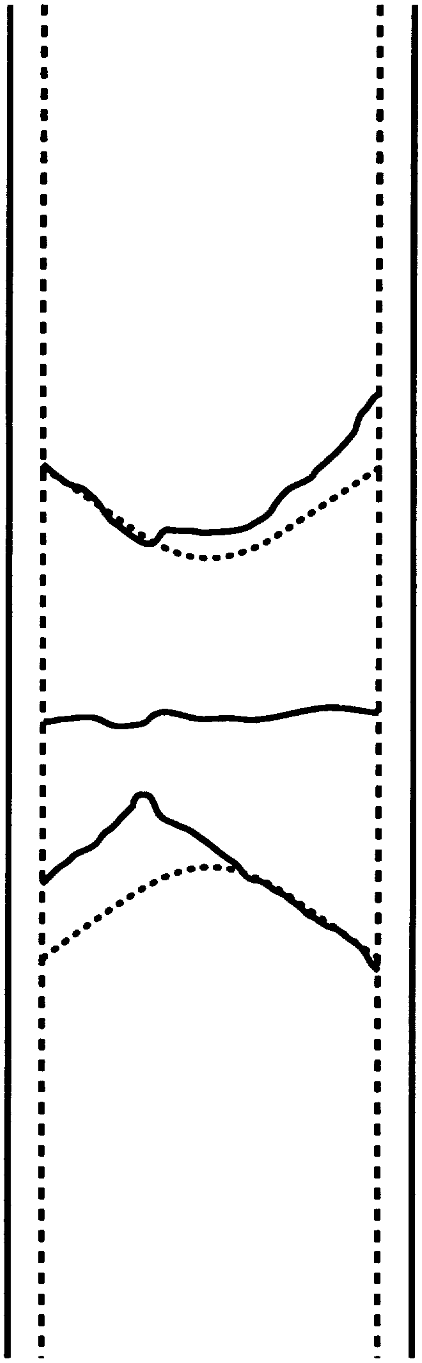

Figure 5.3: Predicted trajectories of two curved microcracks in an AS4/PEEK $[90/0_8]_s$ laminate compared to experimentally observed shapes.

5.3 Generalized Analysis

The variational analysis has been successful and it is worth considering ways to generalize the technique to solve a wider variety of composite fracture problems. There are two features to the variational analysis of $[(S)/90_n]_s$ and $[90_n/(S)]_s$ laminates in Chapter 2 that require generalization:

1. The stresses in the undamaged laminate
2. The number of ply groups

5.3.1 The Initial Stress State

Hashin's variational analysis [1–2] and our extensions to that analysis [5, 6, 8–10, 51] all assumed a simple initial stress distribution in the undamaged laminate. In most cases the initial stresses were assumed to be simple uniaxial tension in which all stresses were constant and independent of x and z. To generalize the analysis we should consider initial stresses that are any general function of x and z. In this section we outline some of the problems that can be solved with a more general initial stress state.

When laminates are cooled slowly from the processing temperature, the thermal stresses within any ply are usually assumed to be constant. If the laminate is quenched, however, the temperature distribution during cool down will cause the matrix in the outer plies to solidify before the matrix in the inner plies. Subsequent thermal shrinkage of the inner plies will tend to put the outer plies in compression. This thermal gradient effect will superpose on ply-level thermal stresses that result from disparate thermal expansion coefficients between plies oriented in different directions. Hu and Nairn [7] calculated the distribution of thermal stresses following various cool-down procedures on a thermoplastic cross-ply laminate. Some typical results for a $[90_2/0_2]_s$ graphite/PEEK laminate are shown in Fig. 5.4. Following slow cooling, the stresses in the outer 90° plies are constant and

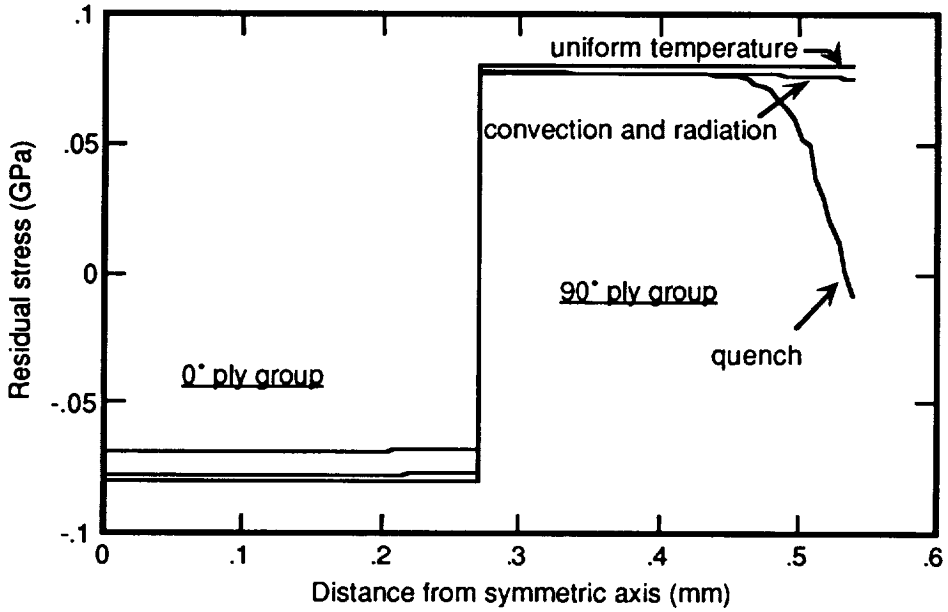

Figure 5.4: The distributions of x-axis residual stresses in a $[90_2/0_2]_s$ laminate cooled under uniform temperature distribution (slow cooling), by convection and radiation, and by quenching to room temperature.

tensile. These constant thermal stresses correspond to the thermal stresses assumed in Chapter 2. If the laminate is quenched, however, this is a significant compression effect on the outer surface.

Differences in the distribution of thermal stresses should be expected to play a role in the fracture properties of laminates. For a large plate, the thermal gradient effect will give initial thermal stresses that are functions of the thickness direction, z, but still independent of the axial direction, x. We generalized the variational analysis of $[(S)/90_n]_s$ and $[90_n/(S)]_s$ laminates to handle any arbitrary distribution of initial stress in the z coordinate. We found that all equations still apply; only the constants C_1–C_4, C_{2a}, C_{3a}, and C_1^*–C_4^* change. For any given distribution of initial stresses, simple formulas were derived to calculate the new constants. Once the new constants are found, the microcracking properties can be analyzed in a manner identical to the procedures in Chapter 2.

Besides thermal gradients, other effects can cause the initial stresses in each ply to vary in the z direction. A simple example is bending loads. Under bending, the stresses will vary linearly across

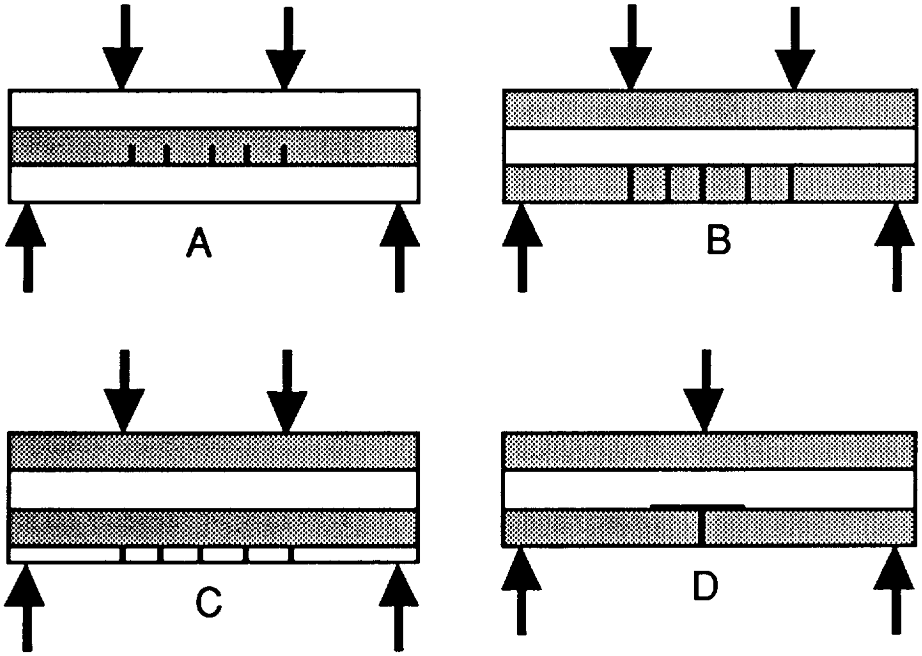

Figure 5.5: Three microcracking specimen geometries in which the initial stresses depend on z and perhaps also on x. A: Four point bending of a $[(S)/90_n]_s$ laminate. B: Four point bending of a $[90_n/(S)]_s$ laminate. C: Four point bending of a laminate with a brittle coating. D: Three point bending of a $[90_n/(S)]_s$ laminate with delaminations.

each ply. For pure bending, the stresses will depend only on z and be independent of x. Thus the generalization that was developed for non-uniform thermal stresses can also be applied to bending geometries. Figure 5.5A and B give two four point bending geometries that might be useful for studying microcracking. Figure 5.5A is an $[(S)/90_n]_s$ laminate under bending. This loading will eventually cause microcracking in the 90° plies. The microcracks probably will not span the entire cross section of the 90°plies; instead compression effects will confine them to the tension side of the beam. The variational analysis can be useful in predicting microcrack formation during bending. The results will be helpful in designing composites that are subjected to bending loads.

Figure 5.5B shows bending experiments on $[90_n/(S)]_s$ laminates. For these specimens one of the surface 90°ply groups will be on the tension side of the beam and the other will be on the compression side. The expectation is that the tension side will microcrack. The variational analysis can be used to predict the microcrack density as a function of bending loads. A related experiment is a composite that has been surface treated with a coating. If the coating is relatively brittle compared to the composite, the first form of failure will be cracking in the coating (see Fig. 5.5C). If an intact coating is crucial to the performance of the composite part, it will be important to understand coating failure and to characterize coating fracture toughness. The variational analysis can be used to predict failure in coatings; in fact, it has already been used to predict failures of coatings on polymeric and metallic parts [87]. It should also be possible to predict coating failures on composite substrates.

Figure 5.5D shows a three-point bending experiment. The initial stresses in this specimen depend on both x and z. The x-direction dependence complicates the variational analysis. The governing equation for minimizing the complementary energy is different than the one in Chapter 2. The equation is still a fourth order differential equation, but it can no longer be solved analytically. It can, however, be rapidly solved numerically to give a variational solution to a new class of fracture problems. For the $[90_n/(S)]_s$ laminate specimen in Fig. 5.5D, we would expect a single microcrack at the point of maximum tensile load which is immediately under the mid-span loading position. The microcrack may soon be followed by delamination emanating from the microcrack tip. We recommend this specimen as the preferred way to study microcrack induced delamination. In ordinary microcracking specimens, delaminations may form at any microcrack and may propagate simultaneously from many different microcracks. As explained in Chapter 4, it is difficult to get experimental results on such delamination processes. By focusing the failure zone using the three-point bending geometry, we have a better hope of obtaining quantitative experimental results on microcrack induced delaminations.

If we treat initial stresses that depend on x and z as an arbitrary state of x–z plane loading, we have the analysis illustrated in Fig. 5.6. This most general analysis will contain all other analyses as special cases. One possible use of a general in-plane loading analysis is as a component of a

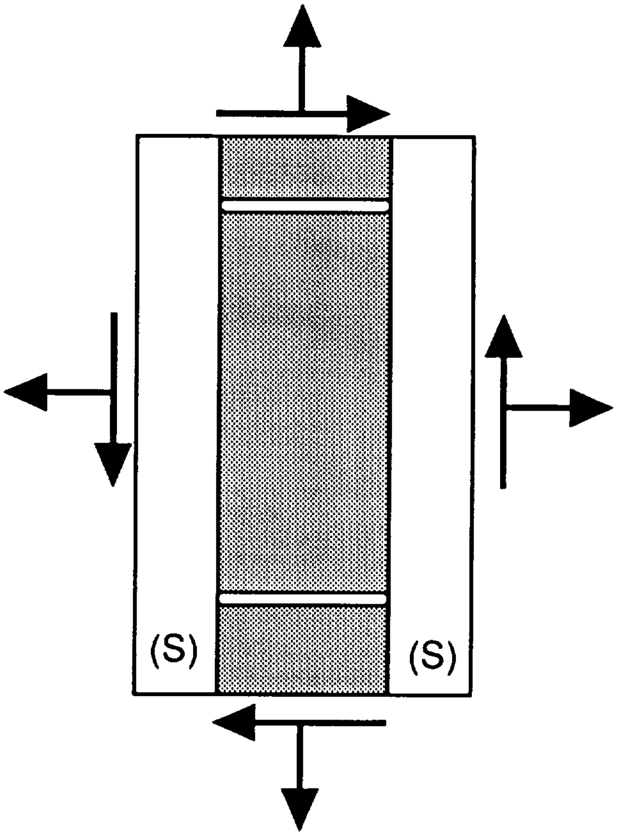

Figure 5.6: An $[(S)/90_n]_s$ laminates are an arbitrary state of x–z plane loading. The arrows indicate tensile and shear loads.

global-local finite element analysis. A global finite element analysis could be used to predict the stress near the off axis plies. The proven variational analysis and energy release rate criterion could then be used to predict the development of microcracking and delamination damage.

5.3.2 Number of Ply Groups

The variational analysis of $[(S)/90_n]_s$ and $[90_n/(S)]_s$ laminates was derived using a relatively small number of ply groups. For $[(S)/90_n]_s$ laminates, symmetry reduced the problem to two ply groups—the 0° plies and the 90° plies. For $[90_n/(S)]_s$ laminates, the antisymmetric damage states necessitated analysis of all four ply groups. The variational analysis of coatings requires three layers [87]. It was fortunate that we could derive realistic models with relatively few ply groups. The analyses with two or three layers reduced to a single fourth order differential equation. The analysis with four layers reduced to two fourth order differential equations that decoupled due to other symmetries. These fourth order differential equations all had constant coefficients and could be solved analytically.

A more general analysis would remove the limit of two to four ply groups. We have worked out the general complementary energy for a sample with any number of layers. This analysis can potentially solve a wide variety of composite fracture problems. The only disadvantage is that future results may require more numerical methods. For a sample with n ply groups, minimizing the complementary energy will require solving $n-1$ or $n-2$ fourth order differential equations. In general the equations will be coupled, but various symmetry relations may decouple some or all of the equations. We can imagine a complementary based finite element package that solves these differential equations. The new numerical methods might offers advantages such as speed, accuracy, or adaptability to fracture predictions, over conventional finite element analyses. If so, it is an analysis technique worth pursuing.

5.4 Embedded Single Fibers

The single-fiber fragmentation test [80–83] is often used to study the fiber/matrix interface in composites. In brief, the fiber is embedded in a matrix and the specimen is loaded in tension under a microscope. As the load increases the single fiber fractures into a roughly periodic array of fragments. The test is interpreted using a simple elastic-plastic analysis of the interface. The smaller the final fiber fragment size, the better the fiber/matrix interface. A major limitation of the single-fiber fragmentation test is that data interpretation always relies on simplistic stress analysis such as elastic-plastic or shear-lag models. One could hope to get more quantitative results from that test if there were better stress analysis techniques available.

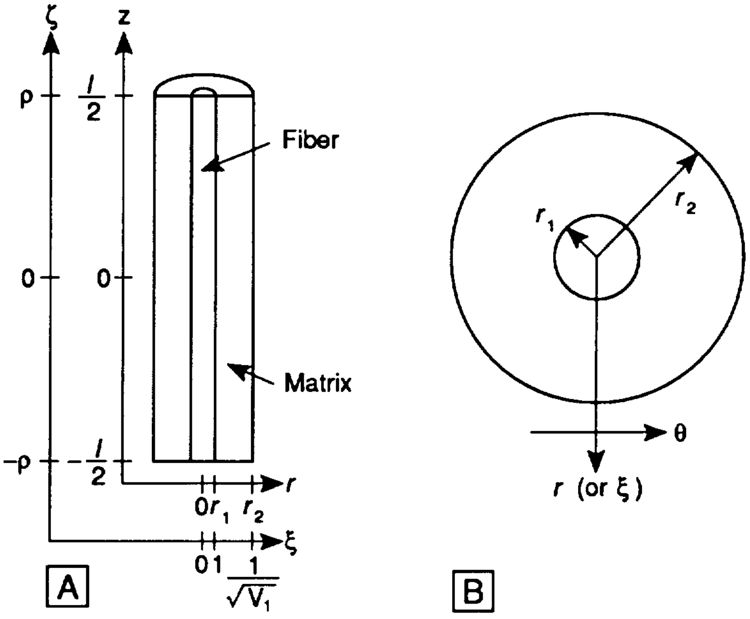

Figure 5.7: An axisymmetric stress analysis for a single embedded fiber. A single fragment of length l. There are breaks at the top and bottom of the fragment (at $z = \pm l/2$) B: A cross-section of the specimen showing the fiber of radius r_1 and the matrix of radius r_2.

As a spin-off from our microcracking theory, we noted that matrix microcracking and fiber fragmentation have much in common. Both involve periodic cracking of a relatively more "brittle" phase embedded in a relatively more "tough" phase. The variational stress analyses of these specimens are thus mathematically related. The only difference is the specimen geometry. The microcracking analysis is a two-dimensional analysis (see Fig. 2.3). As illustrated in Fig. 5.7, the single-fiber fragmentation test is an axisymmetric analysis.

We extended the two-dimensional variational analysis of microcracking to the axisymmetric geometry in Fig. 5.7 (for details see Ref. [88]). The resulting analysis is a single fiber analysis and it gives an accurate stress state for the stresses around breaks in single fiber specimens. Besides analyzing single-fiber fragmentation tests, it can be used to analyze fiber pull-out tests [84] and microdrop debond tests [85]. We applied the analysis to the microdrop debond test [89, 90]. We proposed several failure criteria and used the new analysis to predict experimental results as a function of size of the matrix microdrop. We pointed out that the correct failure model can only be verified by comparison to a large body of experimental results.

The current state-of-the art in single fiber interface testing is to use strength based models. The interface is characterized in terms of an interfacial shear strength and the interface is assumed to fail when the interfacial shear stress equals or exceeds its strength. In our microcracking studies we found that strength based models never work. There is no reason to expect they will be any better for interface characterization. By using the new variational mechanics analysis of stresses in embedded fibers, it is possible to calculate the energy release rate for propagation of interfacial damage. We can hope that such analysis will make it possible to develop a more useful characterization of the fiber/matrix interface.

Chapter 6

LONGITUDINAL SPLITTING

6.1 Introduction

Figure Fig. 6.1A is a double-edge notched (DEN) fracture specimens that can be used to study fracture in isotropic, homogeneous materials. The analysis of fracture in such specimens is well understood, providing the failure is not dominated by plastic yielding processes. For mode I loading, the stress intensity factor is

$$K_I = \sigma^2 Y(a/W)\sqrt{a} \tag{6.1}$$

where σ is applied tensile stress, a is crack length, and $Y(a/W)$ is a geometric calibration function. By linear elastic fracture mechanics, the specimen will fail when K_I equals or exceeds K_{Ic} where K_{Ic} is the critical mode I stress intensity factor. Stated equivalently, if failure occurs when $\sigma = \sigma_c$, than K_{Ic} for the material is

$$K_{Ic} = \sigma_c^2 Y(a/W)\sqrt{a} \tag{6.2}$$

For isotropic materials, the critical stress intensity factor is simply related to the critical stress intensity factor. For plain-strain fracture the relation is

$$G_{Ic} = \frac{(1-\nu^2)K_{Ic}^2}{E} \tag{6.3}$$

where E and ν are the modulus and Poisson's ratio of the material.

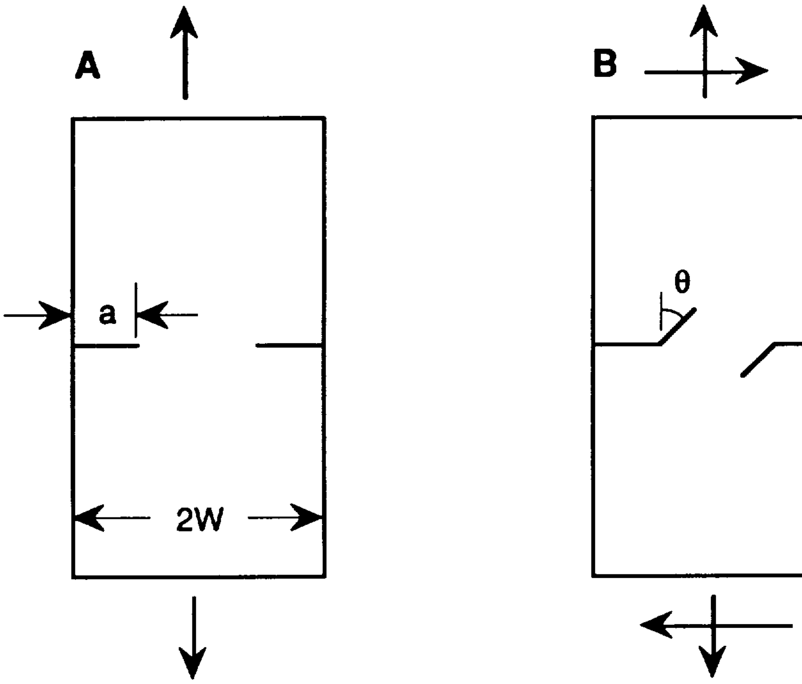

Figure 6.1: Double edge notched specimens for isotropic homogeneous materials. A: Sample under pure mode I loading. B: A sample under mixed mode loading which fails by non-self-similar crack growth at an angle θ with respect to the loading direction.

For composite materials, the fracture analysis process is much more complex. Stated simply, composites differ from isotropic, homogeneous materials, because they are instead anisotropic, heterogeneous materials. We consider each of these differences, how they affect failure, and how one might analyze fracture experiments.

Sih, Paris, and Irwin [91] solved for the crack tip stresses in anisotropic materials. A profound result from their paper is that stress intensity factors for cracks in anisotropic materials are identical to those in isotropic materials. There are some important qualifications that need to placed on this finding, however, before one approaches fracture analysis of composite materials. The invariant stress intensity factors only apply to cracks lying along a symmetry plane of the material and to cracks in infinite sheets. When either of these qualifications are not obeyed, Eq. (6.2) must be modified before analyzing fracture.

If the crack is not along a symmetry plane, then pure mode I loading can result in both mode

I and mode II loading along the crack plane. This situation complicates the fracture analysis, but also opens the possibility of doing mixed-mode fracture testing using simple mode I type specimen geometries. As described below, we make use of this type of mixed-mode loading to study mixed-mode longitudinal splitting in unidirectional composites.

If the specimen is not infinite, the stress intensity factor in an anisotropic sheet will differ from that in a finite sheet. For the simple case of a crack along a symmetry plane, the effect of using a finite sheet of an anisotropic material is that K_I must be replaced by

$$K_I = \sigma^2 Y_a(a/W)\sqrt{a} \tag{6.4}$$

where $Y_a(a/W)$ is a new geometric calibration function for the anisotropic sheet. The effect of specimen size can be understood by visualizing the crack tip singular stress field. For an infinite sheet the stress intensity or magnitude of the singular stress field is independent of the mechanical properties of the material. The shape of that stress field, however, does depend on the mechanical properties. In a unidirectional composite for example, the high stress concentration around the crack tip extends farther along the fiber direction than it does in a similarly notched isotropic material. Because the shape of the stress field depends on material properties, the effect of encroaching on that stress field by choosing finite specimen dimensions will also depend on material properties. We thus expect changes, albeit possibly minor changes, in the stress intensity factor. We noted in Chapter 2 that small changes in the stress analysis can lead to large changes in the fracture predictions. Likewise small changes in the stress intensity factor can lead to large differences in the fracture analysis of notched composites. Before we can expect a valid fracture analysis of composite fracture, we must therefore address the effect of material anisotropy. Analyses that ignore this problem and indiscriminately apply isotropic geometric correction factors are not likely to succeed.

A perhaps more significant difference between isotropic materials and composite materials is that composite materials are heterogeneous. Because they are heterogeneous, failure can follow different paths depending on the material properties in a given direction. In isotropic materials, the properties are the same in all direction. During mode I loading of an isotropic DEN specimen as in Fig. 6.1A, the crack will always propagate by self-similar crack growth normal to the loading direction. Mixed-mode loading of isotropic DEN specimens will give non-self-similar crack growth at some angle θ (see Fig. 6.1B). The angle, however, is determined by the stress state at the crack tip and not by directionally dependent properties of the material. In contrast, composites often have a weak fracture plane. The cracks grow along this weak plane regardless of the loading conditions. This effect of material heterogeneity has two consequences on the analysis of composite fracture. First, the energy release rate for the actual fracture process is no longer uniquely related to the stress intensity factor at the time of failure. To understand this effect, consider the DEN specimen in Fig. 6.1B in which the crack grows at some angle θ determined by the material heterogeneity (*e.g.* it may fail be crack growth along the fiber direction). The stress intensity factor for such a specimen is a function of specimen geometry, crack length, material properties, and material orientation. The energy release rate depends on all these factors, but also depends on the crack growth angle θ. In other words for a given stress intensity factor, the energy release rate will be different for crack growths in different directions. It is not possible to have a unique relation between a single stress intensity factor and the multitude of possible energy release rates.

The second and related effect of material heterogeneity is that stress intensity factor is only of limited use and cannot be the basis for a thorough fracture analysis of composite fracture. To understand this problem, consider the single-edge notched, unidirectional specimens in Fig. 6.2. For a given crack length and applied stress, the stress intensity factors are only weakly dependent on the fiber orientation angle θ. In contrast, we measured the failure load and found it to be strongly dependent on θ. In other words the concept of failure at a critical value of K_I does not correctly predict the θ dependence of failure load in notched unidirectional composites. In contrast,

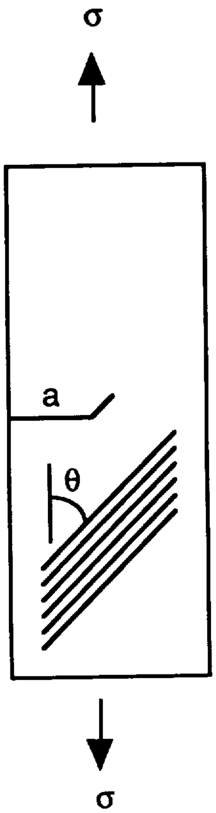

Figure 6.2: A single-edge notched specimen for testing mixed-mode longitudinal splitting in unidirectional laminates. The fibers make an angle θ with respect to the loading direction. Upon loading, the initial edge crack of length a grows at an angle θ or parallel to the fibers. The ratio of mode I to mode II depends on a and θ.

an energy release rate approach can predict the experimental results. Unlike K_I, the energy release rate for crack growth along the fiber direction is a strong function of θ. The preferred approach to fracture mechanics of composites is to say failure occurs when $G = G_c$ where G_c is the critical energy release rate for failure by the observed mechanism.

The difficult task of analyzing composite fracture is to develop stress analysis techniques that can give G for crack growth by various failure mechanisms. In this chapter we limit ourselves to *intralaminar* crack growth in unidirectional composites. In 1962, Hedgepeth outlined a useful shear-lag method for analyzing stress concentrations around broken fibers or notches in unidirectional composites [92]. Since his work, many authors have applied the shear-lag model to stress analysis of unidirectional composites [93–100]. Unfortunately, all of them analyzed infinite sheets and none made calculations of energy release rates. In contrast, Nairn [101, 102] used the shear-lag model to solve for the stresses around cracks in *finite* width DEN specimens with the fibers aligned in the loading direction (see Fig. 6.3). The stresses were used to calculate the energy release rate for self-similar crack growth through the fibers, G_F, or for longitudinal splitting parallel to the fibers, G_L. The result for G_L is

$$G_L = \frac{\sigma^2 a}{4E_c} S_L(a/W) \tag{6.5}$$

where E_c is the tensile modulus of the composite and $S_L(a/W)$ is a geometric calibration function that is specific for longitudinal splitting. $S_L(a/W)$ is given in Ref. [101] where is was noted to be similar to the $Y(a/W)$ function for isotropic DEN specimens. The minor differences are a consequence of the anisotropy of unidirectional composites. The energy release rate for self-similar crack growth through the fibers is

$$G_F = 2G_L\sqrt{\frac{E_c}{\mu_c}} \tag{6.6}$$

where μ_c is the shear modulus of the composite.

Equations (6.5) and (6.6) can be used to predict failure in notched unidirectional composites. If the composites fail be self-similar crack propagation, failure would be expected to occur when $G_F = G_{Fc}$ where G_{Fc} is the critical energy release rate for fiber fracture. If the composites fail by longitudinal splitting, failure would be expected to occur when $G_L = G_{Lc}$ where G_{Lc} is the critical energy release rate for fiber fracture. Conversely, if one knows G_{Lc} and G_{Fc}, it possible to predict the failure mode. In other words one can predict whether failure proceeds by self-similar crack growth or by longitudinal splitting. If G_{Lc}/G_{Fc} is less than G_L/G_F then the composite should fail by longitudinal splitting. Otherwise, the composite should fail by self-similar crack propagation. All reported experiments on organic matrix composites indicate that notched unidirectional composites always fail by longitudinal splitting [100–103]. Thus for organic matrix composite $G_{Lc}/G_{Fc} <$

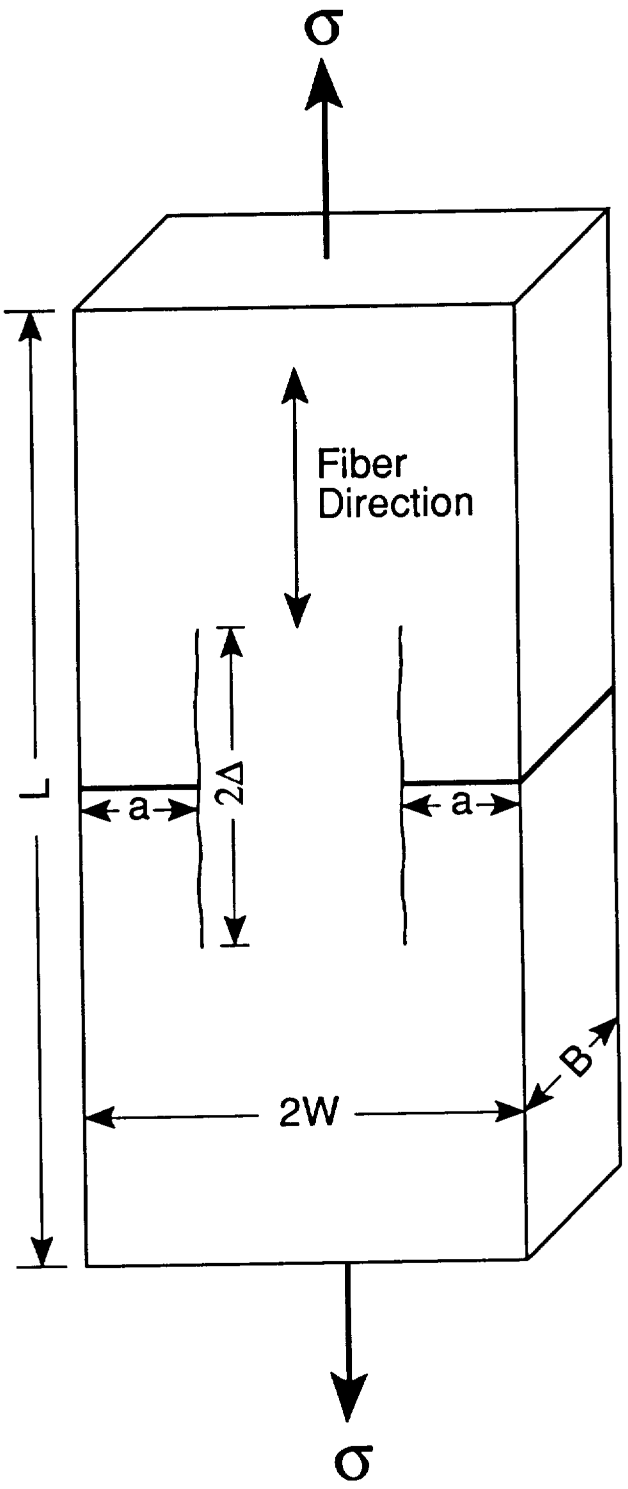

Figure 6.3: The double edge notched specimen geometry. L is total sample length, $2W$ is total sample width, B is sample thickness, a is notch length, Δ is the length of the four longitudinal splits, and σ is applied stress. The fiber direction is parallel to the longitudinal splits.

G_L/G_F.

A problem with the analysis in Ref. [101] is that it does not account for the possibility of fibers bridging across the longitudinal split fracture surface. In this project, we modified the shear-lag analysis of longitudinal splitting to account for fiber bridging. In this chapter we discuss using the new analysis to interpret longitudinal splitting experiments on DEN specimens. We found that the fiber bridging analysis agreed better with experimental observations than did an analysis that ignores fiber bridging. More importantly, we demonstrated that care must be taken in characterizing the toughness of composite materials. If one indiscriminately applies energy release rate equations, one is likely to misinterpret the results.

The longitudinal splitting experiments were interpreted in terms of total energy release rate for failure. In an attempt to characterize the mixed-mode toughness for longitudinal splitting, we ran experiments with two different specimen geometries—single edge notched unidirectional composites and unidirectional composites in asymmetric four-point bending. Surprisingly, the mixed-mode failure envelope for the two different specimens were drastically different. We concluded that the asymmetric four-point bending test was the best. The single edge notched tests were influenced by fiber bridging that precluded measuring the *true* material toughness for *intralaminar* fracture toughness.

6.2 Materials and Methods

Unidirectional Hercules AS4 carbon/3501-6 epoxy composites were made from Hercules prepreg and autoclave cured according to the manufacturer's recommendations. All Hercules IM6/DuPont Avimid® K Polymer composites were supplied by duPont. The testing specimens were 12.7 mm wide by 127 mm long. The thicknesses ranged from 1.25 mm to 4 mm depending on number of plies. We tested 10, 20, and 32 ply laminates.

Included in the Avimid® K Polymer laminates were same laminates with intentionally varied matrix properties and processing conditions. The neat matrix toughnesses were measured by duPont from the same batch of matrix that was used to make the composites. The toughnesses varied from 300 to 1500 J/m^2 and were controlled by varying the molecular weight. They were measured according to ASTM E399 [104] procedures using single-edged notched bending specimens. The processing conditions were varied by varying the final consolidation temperature. The final temperature was varied from 650°F to 680°F.

Most specimens were notched using a 10 mil diamond wheel on a DoAll cutting machine. Some specimens were double-edge notched (DEN) and others were single-edged notched (SEN). The lengths of the cracks were measured using a traveling microscope. Before testing, each specimen had aluminum end-tabs glued in place and was painted with white correction fluid in the areas of anticipated crack growth. The white correction fluid aided observation of crack initiation.

All experiments were run an on MTS 810 servohydraulic testing frame under displacement control. The load was recorded with a 25 kN load cell. The displacements were recorded with a 50 mm gage length extensometer. The long gage-length extensometer was used to record displacements remote from the crack tips. The load and displacement data were collected on an IBM PC interfaced to an MTS 464 Data Display Device.

6.3 Longitudinal Splitting

6.3.1 Analysis Ignoring Fiber Bridging

We tested DEN, unidirectional laminates with the fibers perpendicular to the notches (see Fig. 6.3). All our experiments were found to fail be longitudinal splitting parallel to the fibers and parallel to the applied load. To analyze the experiments we first turned to the shear-lag analysis in Ref. [101]. That analysis gives the the energy release rate for initiation of a longitudinal split (see Eq. (6.5)).

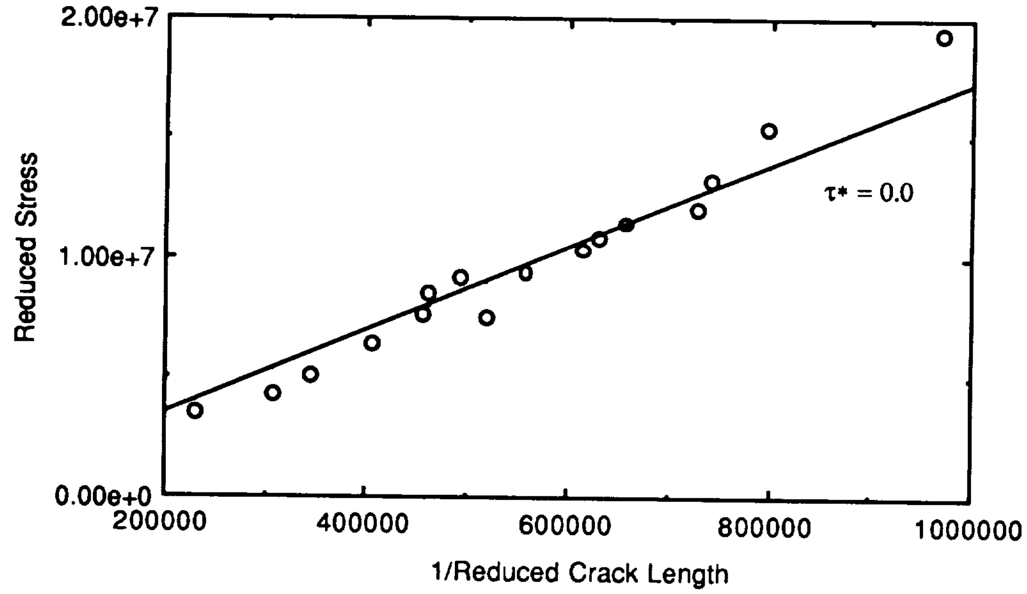

Figure 6.4: A master plot analysis of longitudinal splitting in AS4/3501-6 DEN, unidirectional laminates. The symbols are the experimental points. The line is the prediction of a shear-lag analysis that ignores fiber bridging.

In the spirit of the microcracking analysis in Chapter 2 we constructed a master plot analysis by assuming the longitudinal splitting initiates when $G_L = G_{Lc}$. Rearranging Eq. (6.5) gives

$$\sigma_c\sqrt{W} = \sqrt{\frac{4E_cG_{Lc}}{\frac{a}{W}S_L\left(\frac{a}{W}\right)}} \tag{6.7}$$

Equation (6.7) suggests defining a reduced stress and reduced crack length as

$$\begin{aligned} \text{reduced stress:} \quad \sigma_R &= \sigma_c\sqrt{W} \\ \text{reduced crack length:} \quad a_R &= \frac{a}{4E_cW}S_L\left(\frac{a}{W}\right) \end{aligned} \tag{6.8}$$

A plot of σ_r *vs.* $1/\sqrt{a_R}$ should be linear, pass though the origin and have a slope $\sqrt{G_{Lc}}$.

Nairn [102] reports experimental results for longitudinal splitting of AS4/3501-6 laminates. We repeated those experiments using new material. The experimental results in the form of σ_R *vs.* $1/\sqrt{a_R}$ are given in Fig. 6.4. The slope gives $G_{Lc} = 330$ J/m^2 which agrees well with $G_{Lc} =$ 300 J/m^2 reported in Ref. [102].

A close look at the results in Fig. 6.4 reveals some deficiencies that caused concern. The data on the left half of Fig. 6.4 (region A) are the data for long crack lengths. These data appeared systematically below the theoretical line. The data on the right have of Fig. 6.4 (region B) are the data for short crack lengths. These data appeared systematically above the theoretical line. These discrepancies may result from inaccuracies in the analysis. One of our first thoughts was fiber bridging effects. Observations during the tests or of fracture surfaces after the test confirmed a significant amount of fibers bridging across the longitudinal splits. Because the bridging fibers are parallel to the applied load, they can potentially carry large loads and significantly affect the stresses in the specimen. The next section discusses a modification of the shear-lag analysis to account for fiber bridging.

6.3.2 Fiber Bridging Analysis

As discussed above and in Ref. [101], the energy release rate for the initiation of a longitudinal split from the tip of a notch in double edge notched specimens tested in tension was shown to be:

$$G_L = \frac{\sigma^2 a}{4E_c} S_L(a/W) \tag{6.9}$$

where σ is the applied stress, a is the notch depth, $2W$ is the sample width, E_c is the longitudinal modulus of the unidirectional composite, and $S_L(a/W)$ is a geometric calibration factor that is tabulated in Ref [101]. The analysis that led to Eq. (6.9) was for stress-free longitudinal split fracture surfaces. When fibers bridge across longitudinal splits the fracture surfaces will not be stress free and the amount of energy released will be less than predicted by Eq. (6.9). In other words, Eq. (6.9) will give an amount of energy release that differs from the amount that is released during the actual fracture process.

To account for the presence of bridging fibers, we derived a modified shear-lag analysis that gave a fiber-bridging correction factor. We define $F_B(\tau_B, a/W)$ as the ratio between the actual energy release rate and the energy release rate calculated by assuming that the fracture surfaces

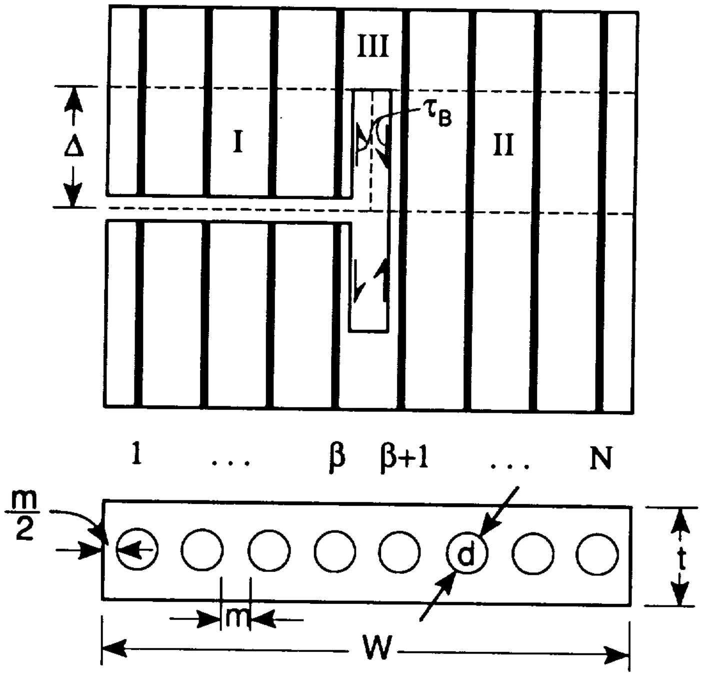

Figure 6.5: An N fiber unidirectional composite in which the first β fibers were broken and a longitudinal split of length Δ exists between fiber β and fiber $\beta + 1$. The longitudinal split fracture surface is loaded by a constant fiber bridging stress of τ_B.

are stress free:

$$F_B(\tau_B, a/W) = \frac{G_L(\text{actual})}{G_L(\tau_B = 0)} \tag{6.10}$$

where τ_B is the fiber bridging stress on the longitudinal split fracture surface. The corrected energy release rate becomes

$$G_L(\text{actual}) = \frac{\sigma^2 a}{4E_c} S_L(a/W) F_B(\tau_B, a/W) \tag{6.11}$$

Figure (6.5) shows the shear-lag model used to calculate $F_B(\tau_B, a/W)$. In brief, we modeled an N fiber unidirectional composite in which the first β fibers are broken and a longitudinal split of length Δ exists between fiber β and fiber $\beta + 1$. To model fiber bridging the surfaces of the longitudinal split were assumed to be held back by a shear traction of τ_B. When $\tau_B = 0$ we recover the model in Ref. [101] and the energy release rate in Eq. (6.9). When $\tau_B \neq 0$ we have a fiber bridging model and a model for calculating $F_B(\tau_B, a/W)$.

The fiber bridging correction factor, $F_B(\tau_B, a/W)$, potentially depends on τ_B, a/W, and specimen dimensions. We varied the specimen width, by varying the number of fibers in the model, N, and varied the crack length a. The calculation of $F_B(\tau_B, a/W)$ requires a large numerical calculation. A remarkable results, however, is that all numerical results can be reproduced with a simple analytical formula [72]:

$$F_B(\tau_B, a/W) = 1 - \tau^* \left(\frac{1 - \frac{a}{W}}{\frac{a}{W}}\right)^{0.4193} \tag{6.12}$$

where

$$\tau^* = \frac{\tau}{\sqrt{W}} \tag{6.13}$$

and τ is a dimensionless fiber-bridging stress defined in Ref. [72]. For more details on the evaluation of $F_B(\tau_B, a/W)$, the reader in referred to Ref. [72]. The next two sections discuss using the fiber bridging analysis to interpret longitudinal splitting experiments on DEN, unidirectional composites.

6.3.3 AS4/3501-6 Splitting

We measured the stress to initiate longitudinal splitting as a function of notch depth in AS4/3501-6 laminates. To analyze the experiments we assumed that longitudinal splitting initiates when $G_L = G_{Lc}$. Figure (6.6) compares the fits to experimental data using either an analysis that ignores fiber bridging or an analysis that includes fiber bridging. The fit labeled $\tau^* = 0$ is the fit that ignores fiber bridging. The fit is linear on the master plot of σ_R *vs.* $1/\sqrt{a_R}$. The slope of the line gives $G_{Lc} = 330$ J/m^2. The fit labeled $\tau^* = 0.190$ is the fit that includes fiber bridging. The fiber bridging fit is non-linear because of the $F_B(\tau_B, a/W)$ factor in Eq. (6.11). To calculate G_{Lc} for this material we used a different master plot in which reduced crack density is redefined as

$$\text{reduced crack length:} \quad a_R \;=\; \frac{a}{4E_c^*W} S_L\left(\tfrac{a}{W}\right) F_B(\tau_B, a/W) \tag{6.14}$$

On this new master plot (figure not shown) the theoretical fit is linear and the slope gives $G_{Lc} = 221$ J/m^2.

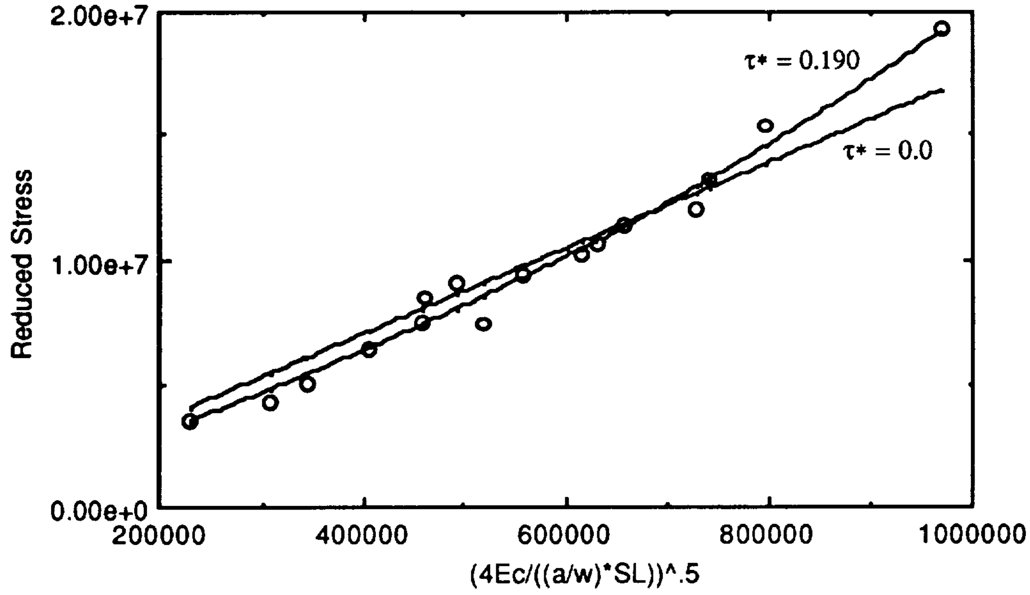

Figure 6.6: A master plot analysis of longitudinal splitting in AS4/3501-6 DEN, unidirectional laminates. The symbols are the experimental points. The line labeled $\tau^* = 0.0$ is the prediction of a shear-lag analysis that ignores fiber bridging. The curved line labeled $\tau^* = 0.190$ is the prediction of a shear-lag analysis that includes fiber bridging.

The fits in Fig. 6.6 show that the fit that includes fiber bridging gave a better fit. In particular it resolved the difficulties at both short and long crack lengths. The better fit, together with the observations that fibers clearly bridged the longitudinal split led us to accept the $G_{Lc} = 221$ J/m^2 from the fiber bridging analysis as the *true* material toughness of AS4/3501-6 composites.

An important result is that accounting for the effect of fiber bridging significantly alters one's interpretation of the material toughness. If we ignored fiber bridging we would claim $G_{Lc} = 330$ J/m^2. When we included fiber bridging, we concluded that G_{Lc} is actually 50% lower or 221 J/m^2. The dogma in the literature usually interprets fiber bridging as a mechanism for *increasing* fracture toughness. We claim that this interpretation is wrong. Fiber bridging may increase the load to cause failure, but it can only increase toughness if it increases the actual energy released during fracture or, in other words, increases the *true* toughness. If it only increases an *apparent* energy release rate in an analysis that ignores fiber bridging, then it is wrong to claim that fiber bridging increases toughness. We discuss this subject further in the discussion.

6.3.4 DuPont Avimid® K Polymer Splitting

A series of DuPont Avimid® K Polymer laminates were tested with various neat resin toughnesses, laminate thicknesses, and processing conditions. The data analysis results were similar to those for AS4/3501-6 laminates. In all samples, an analysis that included fiber bridging gave a better fit than an analysis that ignored fiber bridging. We claim that the analyses that included fiber bridging gave the most reliable measure of laminate toughnesses. Table 6.1 summarizes the experimental results for G_{Lc} and τ^*. In this section we discuss what the experiments told us about fiber bridging and about processing of Avimid® K Polymer laminates.

We investigated the effect of thickness on splitting toughness and fiber bridging stress. We tested three sets of K Polymer laminates with resin toughnesses of 990 J/m^2. They had 10, 20, and 32 plies, respectively. The first three lines of Table 6.1 give the G_{Lc} and τ^* values. G_{Lc} ranged from 252 J/m^2 to 308 J/m^2 or $G_{Lc} = 280 \pm 30$ J/m^2. As a *true* material toughness, G_{Lc} should be independent of laminate thickness. The small observed variation in G_{Lc} following large changes in thickness suggests that G_{Lc} is a *true* material toughness. In contrast, τ^* is a structural parameter that depends on the amount of fiber bridging. The results show that it increased as the laminate thickness increased. The thicker laminates had more plies and therefore had more opportunities to have misaligned plies or fibers that can easily bridge across longitudinal splits. We suggest that it is therefore reasonable for τ^* to increase with thickness. As a corollary, we observe that single ply laminates would have the lowest τ^*. Because the load to induce longitudinal splitting for a given G_{Lc} increases as τ^* increases, it is easier to cause longitudinal splitting in single plies than in multiple plies. In multi-axial laminates, we suggest that more longitudinal splitting damage will be

Table 6.1: Longitudinal splitting fracture results for K Polymer/IM6 laminates. G_{Lc} is the longitudinal splitting fracture toughness. τ^* is the fiber bridging stress.

Thickness (Plies)	Proc. Temp. (°F)	Matrix G_{Ic} J/m^2	G_{Lc} J/m^2	τ^*
10	650	990	308	0.182
20	650	990	265	0.260
32	650	990	252	0.395
32	650	320	486	0.160
32	650	440	423	0.320
32	650	760	321	0.287
32	650	990	252	0.395
32	650	1310	215	0.328
20	650	1780	257	0.165
20	665	1590	329	0.115
20	680	1450	414	0.125

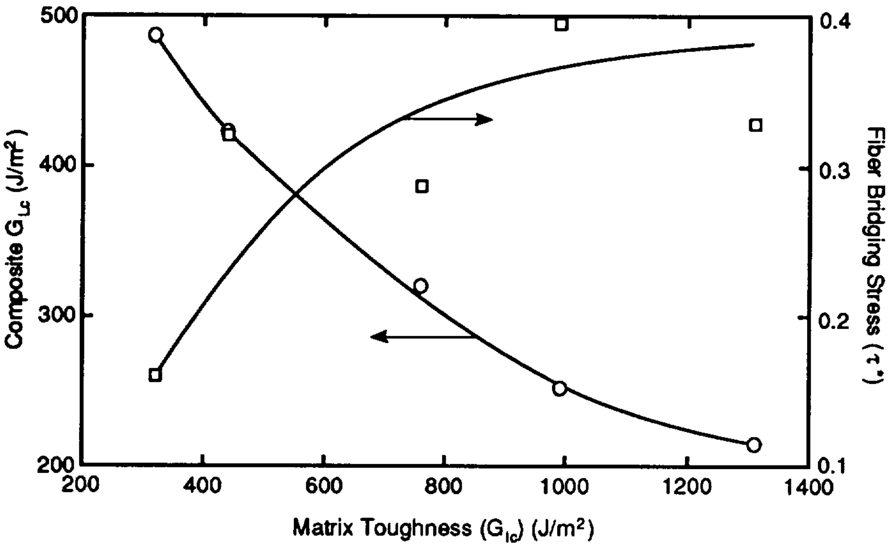

Figure 6.7: The Composite G_{Lc} (○) and fiber bridging stress (τ^*) (□) as a function of the neat matrix toughness for a series of K Polymer laminates.

observed in ply groups having single plies than in ply groups having multiple plies with the same fiber orientation.

By varying the molecular weight of K Polymer, it is possible to produce matrices with a range of neat matrix toughnesses [105]. We measured G_{Lc} and τ^* for laminates with various neat matrix toughnesses. The results are given in lines four to eight of Table 6.1 and plotted in Fig. 6.7. An increase in neat matrix toughness led to a *decrease* in composite G_{Lc}—and inverse correlation. Conversely, the fiber bridging stress was larger for neat resins with higher toughnesses. From Fig. 6.7, there is much more scatter in the τ^* data than in the G_{Lc} data. In general, τ^* is more sensitive to experimental errors in measured failure loads than is G_{Lc}. Besides experimental scatter, however, the variation in the τ^* values may represent real variations in the fiber bridging effect due to real variations in processing conditions, prepreg quality, *etc.*.

There are two possible explanations for the observed trend in G_{Lc}. First, the neat matrix toughnesses were measured in a mode I test. In longitudinal splitting failure, however, mode II failure is significant and perhaps the dominant failure mechanism. Unfortunately, we do not have neat matrix mode II fracture toughnesses that can be compared to the composite G_{Lc}. Second, the neat matrix toughness is controlled by molecular weight [105]. The higher toughness matrices have a higher molecular weight, but also have a higher melt viscosity at a given processing temperature. Because all laminates in Fig. 6.7 were processed at the same temperature, 650°F, it is possible that the lower toughness matrices with the lower melt viscosities gave laminates with better consolidation and better wet-out of the fibers. We suggest that it was consolidation that led to higher G_{Lc}'s in the composites with lower toughness matrices.

Wedgewood and Grant [106] showed that Avimid® K polymer laminates autoclave processed a 650°F with resin toughness of 1250 ± 40 J/m^2, have a significant amount of matrix cracking running normal to the ply direction. Because these cracks run in the same direction as the longitudinal splits, it is reasonable that they will reduce the value of G_{Lc}. The photomicrographs in Ref. [106] show that a reduction of resin viscosity by an increase in processing temperature eliminates these cracks and gives improved laminates. We suggest a similar mechanism applies to the increase in G_{Lc} that results from a decrease in resin viscosity effected by a decrease in molecular weight or resin toughness. The improved laminate quality may also imply less fiber bridging as suggested by the lowest value of τ^* for the lowest toughness resin.

To further study the hypothesis that lower resin viscosity leads to improved G_{Lc} and to reduced fiber bridging, we examined the effect of processing temperature. Wedgewood and Grant [106] showed that increasing the processing temperature from 650°F to 680°F eliminates the matrix cracks. We tested 20 ply laminates processed at 650°F, 665°F, and 680°F. The results for G_{Lc} and τ^* are given in the last three lines of Table 6.1. When the processing temperature increased from 650°F to 680°F, the longitudinal splitting toughness, G_{Lc}, increased from 257 J/m^2 to 414 J/m^2 and the fiber bridging stress, τ^*, decreased slightly. These results are consistent with the suggestion that lowering the resin viscosity leads to better consolidated laminates with a higher G_{Lc} and a lower τ^*.

The longitudinal splitting tests proved useful in studying processing of K Polymer laminates. We found that the best laminates were the ones that produced the highest value of G_{Lc}. For laminates with tough matrices, it was important to use a sufficiently high processing temperature to insure that the matrix penetrates into the intraply regions of all plies. Another way to characterize laminate toughness is the more common delamination fracture toughness test. We did delamination experiments that agreed with delamination results in Ref. [72]. They showed that the higher toughness resins always gave a higher delamination toughness. Furthermore increasing the processing temperature from 650°F to 680°F caused a *decrease* in delamination toughness. At first these results seem contradictory to the longitudinal splitting results because they indicate a lower processing temperature as the one that produces the best laminate. We suggest that the higher delamination toughness at the lower processing temperature is a results of a poorly consolidated laminate. Instead of penetrating into the plies, the matrix remains preferentially at the ply interface. The excess matrix at the ply interface improves the delamination toughness. However, this improvement comes at the expense of other laminate properties and at the expense of overall laminate quality. The clear picture is that characterizing the fracture toughness of advanced composites is a complex process. If the studies are limited to a single failure mode, such as delamination, it will be easy to reach invalid conclusions. A complete understanding of composite toughness can only follow from a battery of tests that examine various failure modes. For K Polymer laminates, it was important for that battery of tests to include longitudinal splitting experiments.

The τ^* parameter has a physical interpretations as the amount of fibers bridging the fracture surfaces in the test specimen. The K Polymer results suggest that it also an indicator of laminate quality. Other things being equal, a decrease in τ^* indicates an improvement in laminate quality. A lower τ^* can indicate better fiber alignment or a better fiber/matrix interface. Both of these factors tend to reduce the amount of fibers that can bridge across fracture surfaces. We therefore recommend longitudinal splitting experiments that measure τ^* as a method for evaluating composite processing. The only drawback is that τ^* is sometimes difficult to measure precisely and is prone to experimental scatter. Therefore, unless careful multi-specimen experiments are available, experimental variations in τ^* might mask real variations in τ^* resulting from laminate quality.

6.4 Mixed-Mode Longitudinal Splitting

Longitudinal splitting is an example of non-self similar crack propagation. The initial crack is perpendicular to the fibers. Loading causes the crack to change direction and propagate parallel to the fibers. In a general laminate having plies at angles other than 0°, we might expect to see longitudinal splitting running parallel to fibers in the off-axis plies. The general description of longitudinal splitting can be described as the general analysis of non-self similar crack growth in unidirectional laminates. To approach this general problem, we did mixed-mode longitudinal splitting experiments on Hercules AS4/3501-6 laminates. We studied the problem using two difference specimen geometries. The next two sections describe the results of those experiments.

6.4.1 Single-Edge Notched Specimens

We did simple tension tests on single edge notched (SEN) unidirectional samples with the fibers at an angle θ with respect to the loading direction. The sample geometry is shown in Fig. 6.2. The sample has an initial crack length a. Failure occurs by crack growth parallel to the fibers or at an angle θ with respect to the loading direction. As θ varies from 90° to 0°, the crack tip stress state varies from pure mode I to increasing amounts of mode II loading. In brief, we measured the load to initiate longitudinal splitting as a function of a/W and θ. To evaluate mixed-mode fracture toughness, we calculated G_I and G_{II} using finite element analysis.

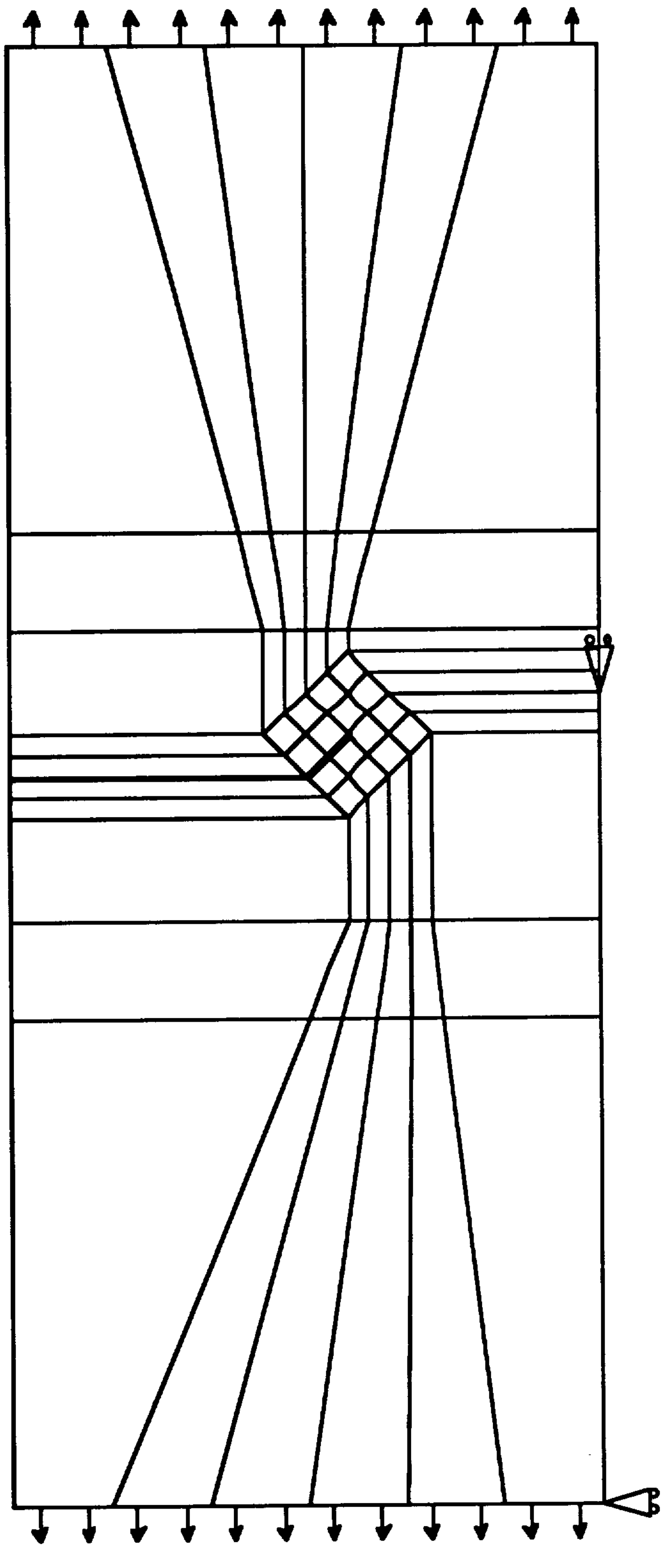

Figure 6.8: Typical coarse mesh for analysis of non-self-similar crack growth in single edge notched unidirectional laminates. The thick line is the initial crack; it consists of a machined in notch (horizontal portion) and an assumed initial bent crack (angled portion).

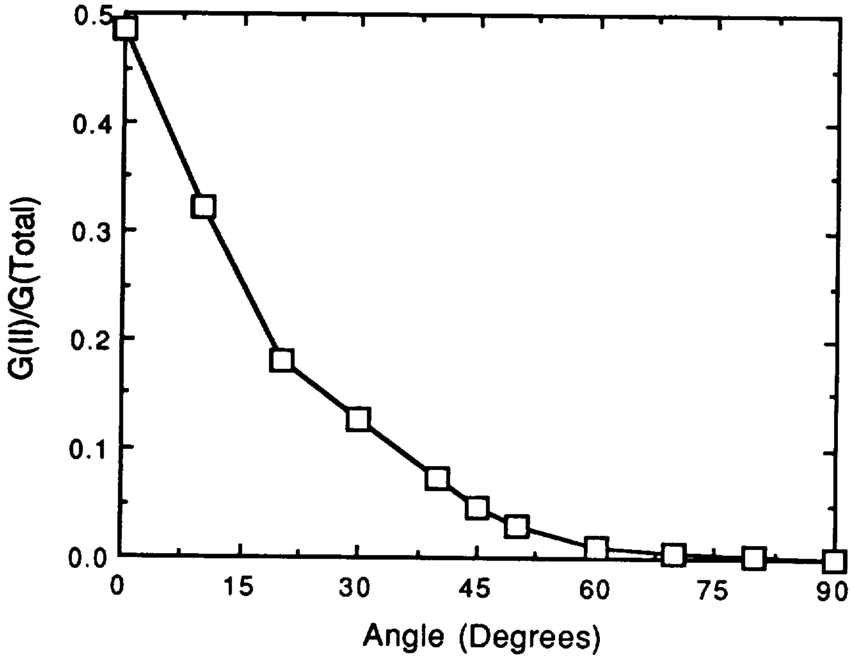

Figure 6.9: Fraction mode II component as a function of fiber angle for longitudinal splitting in single edge notched unidirectional laminates with initial $a/W = 0.5$.

A sample finite element mech for a $\theta = 45°$ sample is shown in Fig. 6.8. The mesh in Fig. 6.8 is a coarse mesh. Using convergence checks, we subdivided each element in Fig. 6.8 into many more elements. Final meshes of 2500-5000 nodes gave good results. We calculated G_I and G_{II} for growth of an assumed initial bent crack using crack closure methods [107]. Our experimental interest is in the initiation of bent crack growth and not in the propagation of an an existing bent crack. To find these energy release rates we calculated G_I and G_{II} as a function of assumed bent crack length and extrapolated the results to zero bent crack length. A plot of the fraction of the total G that is mode II is given in Fig. 6.9. As expected, the 0° sample gives the most mode II character—about 50% mode II. Spanning angles from 0° to 90° allows us to test longitudinal splitting under various amounts of mixed-mode loading. A limitation of the SEN test is that we could not do pure mode II tests, or even mostly mode II tests.

The experimental results were analyzed by the following methods. For each specimen, we used the initial crack length and calculated the mode I and mode II energy release rates for crack growth along the fiber direction for a sample under an arbitrary axial load. Denoting these energy release rates as $G_{I,FEA}$ and $G_{II,FEA}$ we converted each to a reduced energy release rates, $g_{I,FEA}$ and $g_{II,FEA}$, using

$$g_{I,FEA} = \frac{G_{I,FEA}}{\sigma^2 W} \qquad \text{and} \qquad g_{IIO,FEA} = \frac{G_{II,FEA}}{\sigma^2 W} \tag{6.15}$$

The reduced energy release rates depend on the dimensionless crack length or a/W. They have units of 1/modulus and will therefore depend on the mechanical properties of the composite material. As confirmed by calculations, the reduced energy release rates are independent of applied load and sample width and depend only weakly on sample length. After calculating $g_{I,FEA}$ and $g_{II,FEA}$ for each experimental crack length, we can calculate a G_I and G_{II} for each experiment using

$$G_I = \sigma_{exp}^2 W_{exp} g_{I,FEA} \qquad \text{and} \qquad G_{II} = \sigma_{exp}^2 W_{exp} g_{II,FEA} \tag{6.16}$$

where σ_{exp}^2 and W_{exp} are the experimental values for failure stress and sample width.

The G_I–G_{II} failure envelope for AS4/3501-6 laminates tested with SEN specimens is given in Fig. 6.10. Each point corresponds to a different specimen with various values of a/W and θ. We found a surprising result. As the amount of mode II loading increased the mode I toughness increased. These results are atypical for mixed-mode fracture. They agree with similar longitudinal splitting experiments by Wang *et. al.* [108], but we suspected something wrong with the SEN specimens. The next section discusses an alternative specimen geometry that can be used to measure the same mixed-mode fracture toughness data.

6.4.2 Asymmetric Four-Point Bending

There were two problems with the SEN specimens. First, SEN specimens are limited to mixed mode fracture that is at least 50% mode I. Second, as discussed above, the SEN results were atypically for mixed-mode fracture and we suspected them to be wrong. For an alternate specimen, we choose

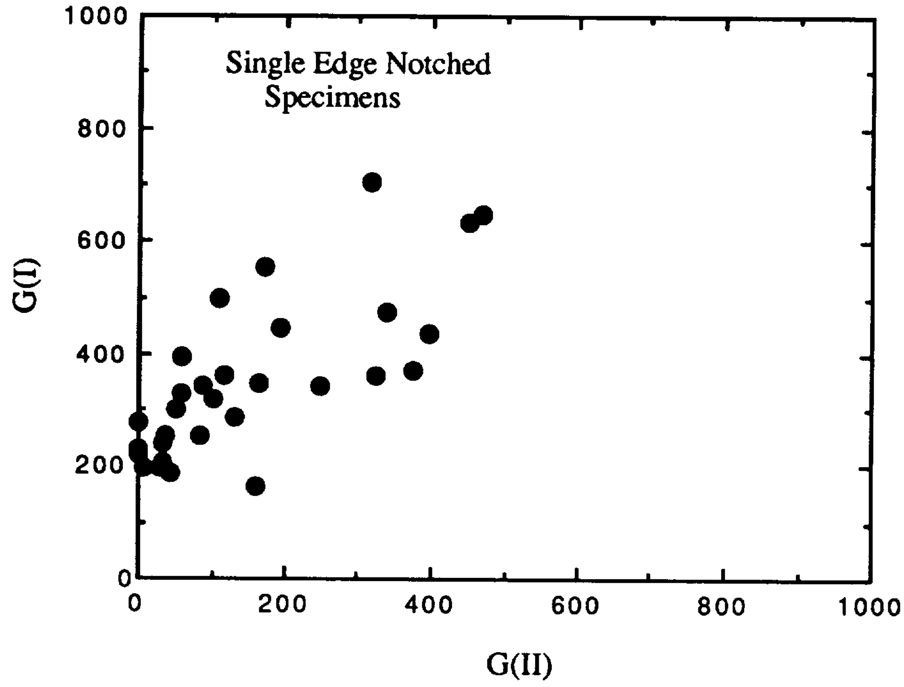

Figure 6.10: Mixed-mode fracture toughness of AS4/3501-6 unidirectional laminates of off-axis SEN specimens.

the asymmetric four point bending geometry in Fig. 6.11. By varying A, B, C, and D, the notch length a, and the fiber angle θ, it is possible to vary the ratio of mode I to mode II loading. The same specimen type can be used to vary the mixed mode loading from pure mode I loading to pure mode II loading.

The asymmetric four-point bending specimen was first proposed for mixed-mode testing of isotropic, homogeneous materials. A numerical stress analysis that gives the mixed-mode stress intensity factors in isotropic, homogeneous materials is available. Unfortunately, those results are not useful for analysis of composite fracture. We therefore used finite element analysis to interpret our experiments. In brief, we used the mesh in Fig. 6.8 except that the tensile loading was replaced by the bending loads shown in Fig. 6.11. Otherwise, the numerical analysis and the application of the numerical results to in interpretation of the four-point bending data were identical to the procedures described in the *Single Edge Notched Specimens* section.

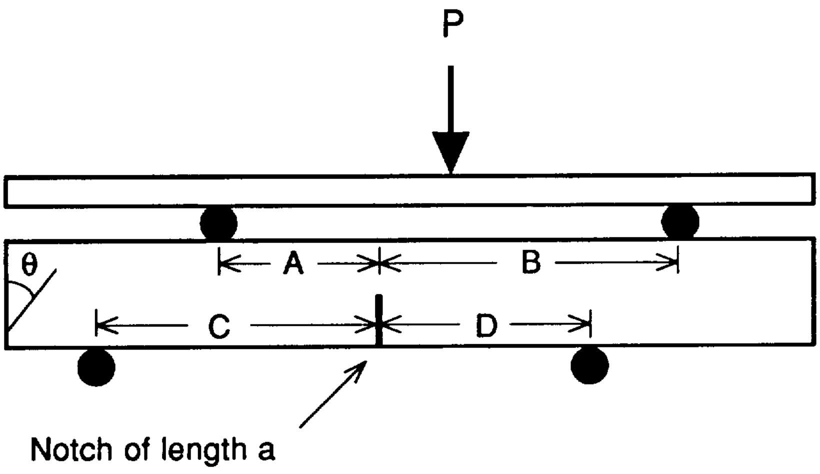

Figure 6.11: The asymmetric four-point bending test specimen. By varying A, B, C, and D, the notch length a, and the fiber angle θ, it is possible to vary the mixture of mode I and mode II loading.

The G_I–G_{II} failure envelope from experiments on asymmetric four-point bending AS4/3501-6 specimens is in Fig. 6.12 (open circles). Each data point corresponds to a different specimen with various values of a/W and θ; all specimens as θ equal to a small angle and most had θ =0°. This new mixed-mode failure envelope is more typical of mixed-mode fracture results. The G_I–G_{II} locus of failure roughly defines a quarter of an ellipse extending from pure mode I loading with G_{Ic} of about 300 J/m^2 to pure mode II loading with G_{IIc} of about 650 J/m^2. Superimposed on Fig. 6.12 are the the results from SEN specimens. The four-point bending experiments and the SEN specimens agreed for pure mode I testing, but as the amount of mode II loading increased the two specimens disagreed dramatically.

Although we cannot give a quantitative explanation of the differences between SEN specimens and four-point bending specimens, we qualitatively attributed the differences to fiber bridging effects. In all experiments, the energy release rate is calculated by an finite element analysis analysis that assumes that the fracture surfaces are stress free and therefore are not bridged by any load carrying fibers. If load is carried across the fracture surfaces, however, the finite element analysis will give the *wrong* energy release rate. Like the longitudinal splitting analysis discussed earlier in

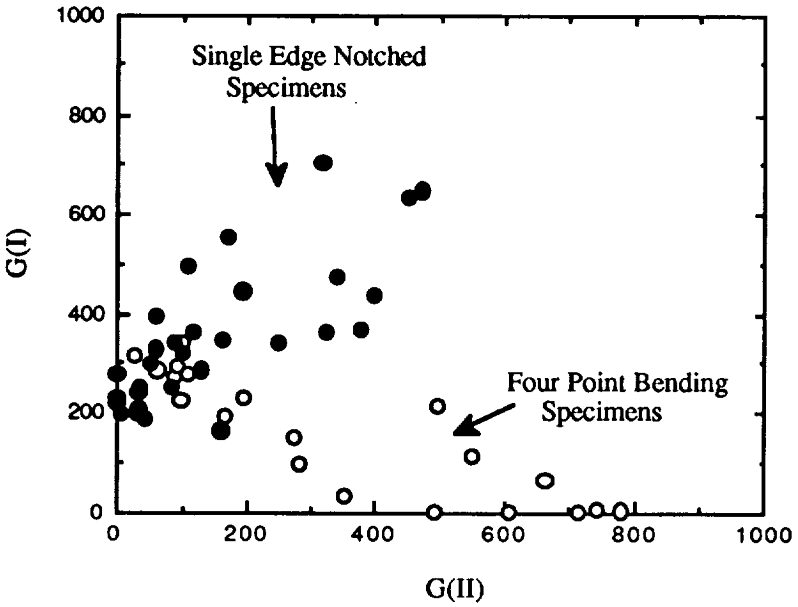

Figure 6.12: Mixed-mode longitudinal splitting of AS4/3501-6 laminates. The filled symbols are results from off-axis single-edge notched specimens. The open symbols are results from asymmetric four-point bending specimens.

this chapter, by ignoring the energy stored in the bridging fibers, the finite element analysis will give an energy release rate that is higher than the actual amount of energy released during the fracture event [72]. The magnitude of the error will depend on the amount of load carried by the bridging fibers. If the fibers carry much load, the error will be large. If the fibers carry little load, the error will be small.

We qualitatively interpret our results by considering the orientation of the fibers with respect to the applied loads. To make the analysis conceptually simple we considered the orientation of the main sample loads in the corresponding unnotched specimen. In the four-point bending specimens which had $\theta = 0$ or some other small angle, the main bending loads were parallel to the long axis of the specimen and thus perpendicular to the fibers. Any fibers that bridge a crack will be perpendicular to the main loads and thus carry only minimal loads. We therefore expect that a finite element analysis that ignores fiber bridging will give acceptable results. In other words we trust the four-point bending results and claim that they represent the *true* mixed-mode longitudinal splitting properties of AS4/3501-6 laminates. On the contrary, in SEN specimens, as θ goes from 90° to 0° the fibers become increasingly aligned with the applied load. The $\theta = 90°$ specimens corresponds to a pure mode I specimen. As θ goes from 90° to 0°, the amount of load II loading increase. Because increasing alignment with the applied load will cause increasing error in the finite element analysis calculation, we claim that the SEN specimen results are increasingly in error as the amount of mode II loading increases. We concluded that the observed increase in mode I toughness resulting from an increased level of mode II loading is an artifact of fiber bridging in the SEN specimens. In support of these conclusions we note that the SEN specimens and the four-point bending specimens give the same results for pure mode I loading. They agree because the pure mode I, SEN specimens have their fibers perpendicular to the applied load and are relatively unaffected by fiber bridging.

These new results show the importance of accounting for fiber bridging when interpreting fracture experiments on composite materials. Fiber bridging effects can produce results that are better classified as *effective* or *apparent* fracture toughnesses. A fundamental understanding of composite failure, however, involves measuring the *true* material toughness. In our experiments the SEN specimens gave an *effective* fracture toughness, while the four-point bending specimens gave a *true* material toughness. In the *Conclusions* section we further discuss the meaning of *true* material toughness.

6.5 Conclusions

We studied longitudinal splitting in unidirectional composites using double edge notched (DEN) specimens, single edge notched specimens (SEN), and asymmetric four-point bending specimens. The DEN specimens were analyzed by a shear-lag model; the other specimens were analyzing using finite element analysis. An important finding was that the experimental results had to be interpreted by accounting for fiber bridging. Equivalently, if one analyzes fracture data and ignores the possibility of fiber bridging, than one is likely to misinterpret the results. In the shear-lag analysis of DEN specimens, we accounted for fiber bridging by modifying the shear-lag analysis of Ref. [101] to include fiber bridging stresses on the fracture surface. In the mixed-mode longitudinal splitting experiments, we accounted for fiber bridging by choosing a specimen geometry, four-point bending, that appears to minimize the effect of bridging fibers.

In describing the results, we often referred to a material's *true* fracture toughness. We claim that it is always the *true* fracture toughness that characterized the fracture toughness of a composite. We therefore should define and discuss the concept of *true* material toughness. There is no ambiguity. The *true* fracture toughness by any composite damage mode is equal to the amount of energy released during the fracture event per unit damage area. Any other measure of fracture toughness cannot be a *true* fracture toughness.

In characterizing the fracture toughness of composites, we need techniques that can measure the *true* material toughness. The most direct method is the area method. Consider the load displacement diagram for a linear elastic material experiencing damage in Fig. 6.13A. The triangular area between the load-displacement curves at two levels of damage is exactly equal to the energy required to cause that damage. That area divided by the amount of new fracture area is unambiguously the *true* fracture toughness. Unfortunately there are several problems with the area method. First, measuring the area between two load-displacement curves is inherently prone to experimental error. The differential area, ΔA, is the difference of two similar numbers. Such differences are always difficult to measure precisely. Second, it can be difficult to precisely measure the new fracture surface area. The difficulties are compounded when the fracture surfaces are rough or when some of the damage is interior to the laminate (*e.g.* microcracking damage). Third, the area method cannot be used for fracture modes in which an increase in damage causes only a small increase in

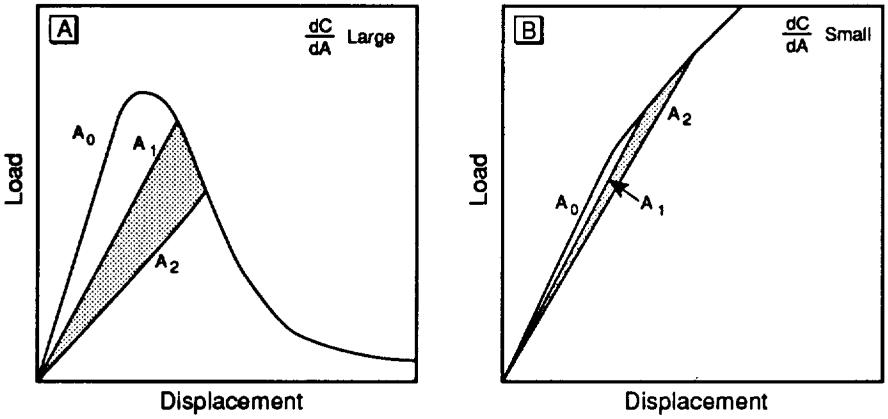

Figure 6.13: Two type of load-displacement curves for a material during crack propagation. A: Fracture experiment in which the compliance changes rapidly with fracture area growth. B: Fracture experiment in which the compliance changes slowing with fracture area. The lines labeled A_0, A_1, A_2 are loading lines for specimens with A_0, A_1, and A_2 total fracture area with $A_0 < A_1 < A_2$.

specimen compliance. As illustrated in Fig. 6.13B, when the slope of the load-displacement curve changes on slightly after an increase in damage area, a precise measurement of ΔA is impossible. The microcracking damage mode studied in Chapter 2, and the longitudinal splitting damage mode studied in this chapter are two examples of failure modes in which the damage has a small effect on specimen compliance. For these and other related damage modes, the area method cannot be used.

Because of difficulties in using the area methods, it is common to develop *hybrid* fracture analysis methods. By *hybrid* fracture analysis methods we mean methods that combine experimental measures of the failure load with a theoretical analysis of the energy release rate to measure the specimen toughness. In brief, the *hybrid* methods use theoretical results to convert measured failure loads, P_c, into critical energy release rates. A common example is delamination fracture in double cantilever beam specimens. If the crack initiates at a load of P_c, simple beam theory gives the fracture toughness as [78]:

$$G_c = \frac{12P_c^2a^2}{EB^2D^3} \tag{6.17}$$

where a is the delamination length, E is the modulus, B is the thickness, and D is the beam depth. This simple beam analysis is sometimes replaced by more advanced theories that account for effects such as nonlinear deformations or crack tip rotations [73]. Conceptually similar are the equations that give energy release rate for longitudinal splitting for a given load to cause that splitting. Equation (6.9) is an equation that ignores fiber bridging; Eq. (6.11) is one that includes the fiber bridging effect.

The success of the *hybrid* method is contingent on the accuracy in which the analysis converts the failure load to a fracture toughness. If the theory that give the G_c–P_c relation is overly simplistic or if it ignores real effects such as fiber bridging, it will give the wrong fracture toughness. By wrong fracture toughness we mean a fracture toughness that is not the *true* toughness or a fracture toughness that differs for the area method fracture toughness. The effect of fiber bridging on the analysis of DEN longitudinal splitting experiments is a good illustration of the care that must be taken in developing successful *hybrid* fracture analysis methods. If we ignored fiber bridging, we would use Eq. (6.9) and calculate the wrong energy release rate. As shown by the fiber bridging analysis, Eq. (6.9) overestimate the fracture toughness. The *true* fracture toughness is actually lower and is more accurately given by the fiber bridging analysis in Eq. (6.11).

Fiber bridging is often invoked as a mechanism for increasing the fracture toughness during crack propagation in composite materials. For example, consider a double cantilever beam specimen. If fibers bridge across the delamination front and if those fibers carry a significant amount of load, it is clear that the load required to cause delamination will be higher than it would be in the absence of fiber bridging. If the failure loads are then substituted into Eq. (6.17), or into more advanced beam theories, one could draw the erroneous conclusion that fiber bridging causes an increase in toughness. This conclusion is a misinterpretation of the experimental results. When fiber bridging becomes significant, Eq. (6.17), or related equations that also ignore fiber bridging, will give the *wrong* energy release rate. They can therefore not be used to draw conclusions about the effect of fiber bridging on fracture toughness. The correct interpretation of the results is that fiber bridging increases the load required to induce damage. Whether or not the fiber bridging also increases the fracture toughness can only follow from using analyses that account for fiber bridging.

The double cantilever beam specimen is an ideal specimen for area method measurements. The specimen compliance changes significantly as the delamination propagates and under favorable conditions accurate area method measurements can be made. By comparing area method results to beam theory results it is possible to see if the beam theory analyses give accurate fracture toughnesses or if important effects such as fiber bridging have been ignored. Williams *et. al.* [73] did such experiments. The measured load as a function of crack length and interpreted the results using an area method and various beam theory methods. They found that simple beam theory is in poor agreement with the area method and therefore gives the *wrong* energy release rate. In contrast a beam theory correct for non-linear displacement effect and crack tip rotations agrees well with area method. The implication is that using those theories in a *hybrid* method fracture analysis give the *true* energy release rate. A significant observation is that Williams *et. al.* [73] did not need to include fiber bridging to get good agreement be the area method and the *hybrid* method. The implication is that fiber bridging does not contribute significantly to the energy released during delamination. Although fibers can be observed to bridge across delaminations, they probably carry too little load to significantly affect the analysis.

Our longitudinal splitting results contrast to the delamination results. Fibers that bridge across longitudinal splits are aligned with the applied axial load and apparently significantly affect the energy released during longitudinal splitting. The fiber bridging effect is best demonstrated by the two stress analyses with and without fiber bridging. For a given applied load, the presence of fiber bridging leads to 50% or more reduction in the *true* energy release rate. In delamination it appears acceptable to ignore fiber bridging, In longitudinal splitting, the fiber bridging effect is large and cannot be ignored.

Our mixed-mode longitudinal splitting tests on SEN specimens and on four-point bending specimens are two more examples of the importance of being aware of fiber bridging effects. We analyzes the fracture results for these specimens using finite element analysis. Because it was very difficult to include fiber bridging in the finite element analysis, we used an analysis that ignored fiber bridging. When such an analysis is used to interpret experiments that are affected by fiber bridging, the analysis will give poor results no matter how accurate the finite element calculations might be. Like the longitudinal splitting experiments, the SEN specimens with $\theta \neq 90°$, were influenced by fiber bridging. We claim the observation that G_I increases as G_{II} increase is an artifact due to misinterpretation of the *true* energy release rate. We likewise conclude that similar results in the literature by Wang *et. al.* [108] were misinterpreted. In contrast, we claim that the fibers that bridge across the splits in the four-point bending specimens had little effect of the energy release rate and thus the analysis that ignores fiber bridging gives accurate results. In other words, the four-point bending specimen is similar to the double cantilever beam specimen in that bridging fibers have little influence of the energy release rate. We claim that the G_I–G_{II} failure envelop from the four-point bending specimens gives the *true* mixed-mode, longitudinal splitting fracture toughness of AS4/3501-6 laminates.

Characterizing the fracture toughness of composite structures is a complicated process. To get a complete characterization of any material it is necessary to analyze many different failure modes. This process will generally involve a battery of tests such as delamination tests, microcracking tests, longitudinal splitting tests, and more. Each fracture test most also be carefully studied to verify that is gives a *true* fracture toughness. Among other things the verification most account for fiber bridging or demonstrate that fiber bridging does not affect the results of its particular specimen. The toughest composite will generally be the one with the best overall balance of properties. Increasing the toughness by one failure mechanism (*e.g.* delamination) at the expense of other failure modes may lead to structure whose overall toughness performance is worse.

Bibliography

1 Z. Hashin, "Analysis of Cracked Laminates: A Variational Approach," *Mech. of Mat.*, **4**, 121 (1985).

2 Z. Hashin, "Analysis of Stiffness Reduction of Cracked Cross-Ply Laminates," *Eng. Fract. Mech.*, **25**, 771 (1986).

3 Z. Hashin, "Analysis of Orthogonally Cracked Laminates Under Tension," *J. Appl. Mech.*, **54**, 872 (1987).

4 Z. Hashin, "Thermal Expansion Coefficients of Cracked Laminates," *Comp. Sci. & Tech.*, **31**, 247 (1988).

5 J. A. Nairn, "The Strain Energy Release Rate of Composite Microcracking: A Variational Approach," *J. Comp. Mat.*, **23**, 1106 (1989). (see errata: *J. Comp. Mat.*, **24**, 233 (1990)).

6 S. Liu and J. A. Nairn, "The Formation and Propagation of Matrix Microcracks in Cross-Ply Laminates During Static Loading," *J. Reinf. Plast. & Comp.*, **11**, 158 (1992).

7 S. Hu and J. A. Nairn, "On the Thermally-Induced Residual Stresses in Thick Fiber-Thermoplastic Matrix (PEEK) Cross-Ply Laminated Plates," Presented at the 9th DoD/-NASA/FAA Conf. on Fibrous Composites in Structural Design, Lake Tahoe, NV, November 1991.

8 J. A. Nairn, S. Hu, S. Liu, and J. S. Bark, "The Initiation, Propagation, and Effect of Matrix Microcracks in Cross-Ply and Related Laminates," *Proc. of the* 1^{st} *NASA Advanced Composite Tech. Conf., NASA CP-3104*, **Part 2**, 497 (1991).

9 J. A. Nairn and S. Hu, "The Initiation and Growth of Delaminations Induced by Matrix Microcracks in Laminated Composites," *Int. J. Fract.*, **57**, No. 1 (1992).

10 J. A. Nairn and S. Hu, "The Formation and Effect of Outer-Ply Microcracks in Cross-Ply Laminates: A Variational Approach," *Eng. Fract. Mech.*, **41**, 203 (1992).

11 H. T. Hahn and S. W. Tsai, "On the Behavior of Composite Laminates After Initial Failures," *J. Comp. Mat.*, **8**, 299 (1974).

12 K. W. Garrett and J. E. Bailey, "Multiple Transverse Fracture in 90° Cross-Ply Laminates of a Glass Fibre-Reinforced Polyester," *J. Mat. Sci*, **12**, 157 (1977).

13 K. W. Garrett and J. E. Bailey, "The Effect of Resin Failure Strain on the Tensile Properties of Glass Fiber-Reinforced Cross-Ply Laminates," *J. Mat. Sci.*, **12**, 2189 (1977).

14 A. Parvizi, K. W. Garrett, and J. E. Bailey, "Constrained Cracking in Glass Fiber-Reinforced Epoxy Cross-Ply Laminates," *J. Mat. Sci.*, **13**, 195 (1978).

15 A. Parvizi and J. E. Bailey, "On Multiple Transverse Cracking in Glass-Fiber Epoxy Cross-Ply Laminates," *J. Mat. Sci.*, **13**, 2131 (1978).

16 J. E. Bailey, P. T. Curtis and A. Parvizi, "On the Transverse Cracking and Longitudinal Splitting Behavior of Glass and Carbon Fibre Epoxy Cross-Ply Laminates and the Effect of Poisson and Thermally Generated Strains," *Proc. R. Soc. Lond. A*, **366**, 599 (1979).

17 M. G. Bader, J. E. Bailey, P. T. Curtis, and A. Parvizi, "The Mechanisms of Initiation and Development of Damage in Multi-Axial Fibre-Reinforced Plastic Laminates," *Proc. 3rd Int'l Conf. on Mechanical Behavior of Materials*, **3**, 227 (1979).

18 J. E. Bailey and A. Parvizi, "On Fiber Debonding Effects and the Mechanism of Transverse-Ply Failure in Cross-Ply Laminates of Glass Fiber/Thermoset Composites," *J. Mat. Sci.*, **16**, 649 (1981).

19 F. R. Jones, A. R. Wheatley, and J. E. Bailey, "The Effect of Thermal Strains on the Microcracking and Stress Corrosion Behavior of GRP," in *Composite Structures*, pp. 415 (ed., I. H. Marshall, Appl. Sci. Publ, Barking, UK, 1981).

20 D. L. Flaggs and M. H. Kural, "Experimental Determination of the In Situ Transverse Lamina Strength in Graphite/Epoxy Laminates," *J. Comp. Mat.*, **16**, 103 (1982).

21 P. W. Manders, T. W. Chou, F. R. Jones, and J. W. Rock, "Statistical Analysis of Multiple Fracture in [0/90/0] Glass Fiber/Epoxy Resin Laminates," *J. Mat. Sci.*, **19**, 2876 (1983).

22 L. Boniface and S. L. Ogin, "Application of the Paris Equation to the Fatigue Growth of Transverse Ply Cracks," *J. Comp. Mat.*, **23**, 735 (1989).

23 A. L. Highsmith and K. L. Reifsnider, "Stiffness-Reduction Mechanisms in Composite Laminates," *ASTM STP*, **775**, 103 (1982).

24 M. G. Bader and L. Boniface, "Damage Development During Quasi-Static and Cyclic Loading in GRP and CFRP Laminates Containing 90° Plies," *Proc.* 5th *Int'l Conf. on Comp. Mat.*, 221 (1985).

25 M. Caslini, C. Zanotti, and T. K. O'Brien, "Fracture Mechanics of Matrix Cracking and Delamination in Glass/Epoxy Laminates," *J. Comp. Tech & Research*, **Winter**, 121 (1987).

26 A. S. D. Wang, P. C. Chou and S. C. Lei, "A Stochastic Model for the Growth of Matrix Cracks in Composite Laminates," *J. Comp. Mat.*, **18**, 239 (1984).

27 A. S. D. Wang, "Fracture Mechanics of Sublaminate Cracks in Composite Materials," *Comp. Tech. Rev.*, **6**, 45 (1984).

28 A. S. D. Wang, N. N. Kishore and C. A. Li, "Crack Development in Graphite-Epoxy Cross-Ply Laminates under Uniaxial Tension," *Comp. Sci. & Tech.*, **24**, 1 (1985).

29 A. S. D. Wang, "Fracture Analysis of Matrix Cracking in Laminated Composites," *Naval Air Development Center Report No. NADC 85118-60* (1985).

30 S. Yalvac, L. D. Yats, and D. G. Wetters, "Transverse Ply Cracking in Toughened and Untoughened Graphite/Epoxy and Graphite/Polycyanate Cross-Ply Laminates," *J. Comp. Mat.*, **25**, 1653 (1991).

31 K. C. Jen and C. T. Sun, "Matrix Cracking and Delamination Prediction in Graphite/Epoxy Laminates," *Proc. of the Amer. Soc. Comp, 5th Tech. Conf.*, 350 (1990).

32 P.W.M. Peters, "The Strength Distribution of 90° Plies in 0/90/0 Graphite-Epoxy Laminates," *J. Comp. Mat.*, **18**, 545 (1984).

33 L. Boniface, P. A. Smith, S. L. Ogin, and M. G. Bader, "Observations on Transverse Ply Crack Growth in a $[0/90_2]_s$ CFRP Laminate Under Monotonic and Cyclic Loading," *Proc 6th Int'l Conf. on Comp. Mat.*, **3**, 156 (1987).

34 S. E. Groves, C. E. Harris, A. L. Highsmith, and R. G. Norvell, "An Experimental and Analytical Treatment of Matrix Cracking in Cross-Ply Laminates," *Experimental Mechanics*, **March**, 73 (1987).

35 S. Yalvac, L. D. Yats, and D. G. Wetters, "Micromechanical Analysis of Fatigue of Toughened and Untoughened Graphite/Polycyanate Cross-Ply Laminates," *Proc. 8th Int'l Conf. on Comp. Mat.*, 38-J (1991).

36 K. L. Reifsnider, "Some Fundamental Aspects of the Fatigue and Fracture Response of Composite Materials," *Proc. 14th Annual Meeting of SES, Lehigh, PA, November*, 373 (1977).

37 F. W. Crossman, W. J. Warren, A. S. D. Wang, and G. E. Law, Jr., "Initiation and Growth of Transverse Cracks and Edge Delamination in Composite Laminates: Part 2. Experimental Correlation," *J. Comp. Mat Supplement*, **14**, 89 (1980).

38 A. S. D. Wang, "Growth Mechanisms of Transverse Cracks and Ply Delamination in Composite Laminates.," *Proc 3rd Int'l Conf. on Comp. Mat.*, 170 (1980).

39 F. W. Crossman and A. S. D. Wang, "The Dependence of Transverse Cracking and Delamination on Ply Thickness in Graphite/Epoxy Laminates," *ASTM STP*, **775**, 118 (1982).

40 W. W. Stinchcomb, K. L. Reifsnider, P. Yeung, and J. Masters, "Effect of Ply Constraint on Fatigue Damage Development in Composite Material Laminates," *ASTM STP*, **723**, 64 (1981).

41 S. Liu and J. A. Nairn, "Fracture Mechanics Analysis of Composite Microcracking: Experimental Results in Fatigue," *Proc. of the Amer. Soc. of Comp., 5th Tech. Conf.*, 287 (1990).

42 S. L. Ogin, P. A. Smith, and P. W. R. Beaumont, "Matrix Cracking and Stiffness Reduction during the Fatigue of a $[0/90]_s$ GFRP Laminate," *Comp. Sci. & Tech.*, **22**, 23 (1985).

43 S. L. Ogin, P. A. Smith, and P. W. R. Beaumont, "A Stress Intensity Approach to the Fatigue Growth of Transverse Ply Cracks," *Comp. Sci. & Tech*, **24**, 47 (1985).

44 D. S. Adams, D. E. Bowles, and C. T. Herakovich, "Thermally Induced Transverse Cracking in Graphite/Epoxy Cross-Ply Laminates," *J. Reinf. Plast. & Comp.*, **5**, 152 (1986).

45 R. G. Spain, "Thermal Microcracking of Carbon Fibre/Resin Composites," *Composites*, **2**, 33 (1971).

46 C. T. Herakovich, J. G. Davis, Jr., and J. S. Mills, "Thermal microcracking in Celion 6000/PMR-15 Graphite/Polyimide," *Thermal Stresses in Severe Environments*, 649 (1980).

47 C. T. Herakovich and M. W. Hyer, "Damage-Induced Property Changes in Composites Subjected to Cyclic Thermal Loading," *Eng. Fract. Mech.*, **25**, 779 (1986).

48 S. A. Salpekar and T. K. O'Brien, "Analysis of Matrix Cracking and Local Delamination in $[0/\theta/-\theta]_s$ Graphite Epoxy Laminates Under Tension Load," *Proc.* 8th *Int'l Conf. on Comp. Mat.*, 28-G (1991).

49 D. S. Adams and C. T. Herakovich, "Influence of Damage on the Thermal Response of Graphite-Epoxy Laminates," *J. Thermal Stresses*, **7**, 91 (1984).

50 D. E. Bowles, "Effect of Microcracks on the Thermal Expansion of Composite Laminates," *J. Comp. Mat.*, **17**, 173 (1984).

51 J. A. Nairn and S. Hu, "Micromechanics of Damage: A Case Study of Composite Microcracking," in *Damage Mechanics of Composite Materials*, (ed., Ramesh Talreja, Elsevier Science Publishers, England, 1992).

52 D. L. Flaggs, "Prediction of Tensile Matrix Failure in Composite Laminates," *J. Comp. Mat.*, **19**, 29 (1985).

53 H. Fukunaga, T. W. Chou, P. W. M. Peters, and K. Schulte, "Probabilistic Failure Strength Analysis of Graphite/Epoxy Cross-Ply Laminates," *J. Comp. Mat.*, **18**, 339 (1984).

54 Y. M. Han, H. T. Hahn, and R. B. Croman, "A Simplified Analysis of Transverse Ply Cracking in Cross-Ply Laminates," *Proc. Amer. Soc. of Comp.*, 2^{nd} *Tech. Conf.*, 503 (1987).

55 Y. M. Han, H. T. Hahn, and R. B. Croman, "A Simplified Analysis of Transverse Ply Cracking in Cross-Ply Laminates," *Comp. Sci. & Tech.*, **31**, 165 (198a).

56 N. Laws and G. J. Dvorak, "Progressive Transverse Cracking in Composite Laminates," *J. Comp. Mat.*, **22**, 900 (1988).

57 R. J. Nuismer and S. C. Tan, "Constitutive Relations of a Cracked Composite Lamina," *J. Comp. Mat.*, **22**, 306 (1988).

58 S. C. Tan and R. J. Nuismer, "A Theory for Progressive Matrix Cracking in Composite Laminates," *J. Comp. Mat.*, **23**, 1029 (1989).

59 Y. Korczynsky and J. G. Morley, "Constrained Cracking in Cross-Ply Laminates," *J. Mat. Sci.*, **16**, 1785 (1981).

60 G. P. Fang, R. A. Schapery, and Y. Weitsman, "Thermally-Induced Fracture in Composites," *Eng. Fract. Mech.*, **33**, 619 (1989).

61 A. S. D. Wang and R. W. Crossman, "Initiation and Growth of Transverse Cracks and Edge Delamination in Composite Laminates: Part 1. An Energy Method," *J. Comp. Mat Supplement*, **14**, 71 (1980).

62 S. A. Salpekar and T. K. O'Brien, "Combined Effect of Matrix Cracking and Stress-Free Edge Delamination," NASA TM 102591 (1990).

63 J.C. Fish and S. W. Lee, "Three-Dimensional Analysis of Combined Free-Edge and Transverse-Crack-Tip Delamination," *ASTM STP*, **1059**, 271 (1990).

64 H. Fukunaga, T. W. Chou, K. Schulte, and P. W. M. Peters, "Probabilistic Initial Failure Strength of Hybrid and Non-Hybrid Laminates," *J. Mat. Sci.*, **19**, 3546 (1984).

65 G. J. Dvorak and N. Laws, "Mechanics of First-Ply Failure in Composite Laminates," *Fracture of Fibrous Composites*, **AMD-Vol 74, ASME**, 59 (1985).

66 G. J. Dvorak and N. Laws, "Analysis of Progressive Matrix Cracking in Composite Laminates II. First Ply Failure," *J. Comp. Mat.*, **21**, 309 (1987).

67 H. T. Hahn and T. Johannesson, "Fracture Mechanics of Unidirectional Composites: Theory and Applications," in *Mechanics of Composites*, pp. 135 (ed., G. J. Dvorak, AMD-V58, ASME, 1983).

68 J. A. Nairn, "The Initiation of Microcracking in Cross-Ply Laminates: A Variational Mechanics Analysis," *Proc. of the* 3^{rd} *Tech. Conf. of the Amer. Soc. of Composites*, 472 (1988).

69 J. Varna and L. Berglund, "Multiple Transverse Cracking and Stiffness Reduction in Cross-Ply Laminates," *J. Comp. Tech. & Res.*, **13**, 97 (1991).

70 J. A. Nairn, S. Hu, and J. S. Bark, "Master Plot Analysis of Microcracking in Graphite/Epoxy and Graphite/PEEK Laminates," Presented at the 3^{rd} NASA Advanced Composite Tech. Conf., Long Beach, CA, June 1992.

71 D. L. Hunston, "Composite Interlaminar Fracture: Effect of Matrix Fracture Toughness," *Comp. Tech. Rev.*, **6**, 176 (1984).

72 J. A. Nairn, S. Liu, H. Chen, and A. R. Wedgewood, "Longitudinal Splitting in Epoxy and K-Polymer Composites: Shear-Lag Analysis Including the Effect of Fiber Bridging," *J. Comp. Mat.*, **25**, 1086 (1990).

73 S. Hashemi, A. J. Kinloch, and J. G. Williams, "The Analysis of Interlaminar Fracture in Uniaxial Fibre Reinforced Polymer Composites," *Proc. R. Soc. Lond.*, **A347**, 173 (1990).

74 P. Paris and F. Erdogan, "Critical Analysis of Crack Propagation Laws," *J. Bas. Eng. Trans. ASME, Ser. D*, **85**, 528 (1963).

75 T. K. O'Brien, "Analysis of Local Delaminations and Their Influence on Composite Behavior," *ASTM STP*, **876**, 282 (1985).

76 T. K. O'Brien, "Towards a Damage Tolerance Philosophy for Composite Materials and Structures," *ASTM STP*, **1059**, 7 (1990).

77 L. R. Dharani and H. Tang, "Micromechanics Characterization of Sublaminates Damage," *Int'l J. Fracture*, **46**, 123 (1990).

78 S. Mostovoy and E. J. Ripling, "Fracture Toughness of an Epoxy System," *J. Appl. Polym. Sci.*, **10**, 1351 (1966).

79 T. K. O'Brien, "Characterization of Delamination Onset and Growth in a Composite Laminate," *ASTM STP*, **775**, 140 (1982).

80 N. J. Wadsworth and I. Spilling, "Load Transfer from Broken Fibres in Composite Materials," *Br. J. Appl. Phys. (J. Phys. D.)*, **1**, 1049 (1968).

81 A. A. Fraser, F. H. Ancker, and A. T. DiBenedetto, "A Computer Modeled Single Filament Technique for Measuring Coupling and Sizing Effects in Fiber Reinforced Composites," *Proc. 30th Conf. SPI Reinforced Plastics Div.*, **Section 22-A**, 1 (1975).

82 L. T. Drzal, M. J. Rich, J. D. Camping, and W. J. Park, "Interfacial Shear Strength and Failure Mechanisms in Graphite Fiber Composites," *Proc. 35th Conf. SPI Reinforced Plastics Div.*, **Section 20-C**, 1 (1980).

83 W. D. Bascom and R. M. Jensen, "Stress Transfer in Single Fiber/Resin Tensile Tests," *J. Adhes.*, **19**, 219 (1986).

84 M. R. Piggott, P. S. Chua, and D. Andison, "Debonding and Friction at Fiber-Polymer Interfaces. I: Criteria for Failure and Sliding," *Comp. Sci. & Tech.*, **6**, 242 (1985).

85 U. Gaur and B. Miller, "Microbond Method for Determination of the Shear Strength of a Fiber/Resin Interface: Evaluation of Experimental Parameters," *Comp. Sci &. Tech.*, **34**, 35 (1989).

86 S. Hu, J. S. Bark, and J. A. Nairn, "On the Phenomenon of Curved Microcracks in $[(S)/90_n]_s$ Laminates: Their Shapes, Initiation Angles, and Locations," *Comp. Sci. & Tech.*, **2**, 641 (1992).

87 J. A. Nairn and S. R. Kim, "A Fracture Mechanics Analysis of Multiple Cracking in Coatings," *Eng. Fract. Mech.*, **42**, 195 (1992).

88 J. A. Nairn, "A Variational Mechanics Analysis of the Stresses Around Breaks in Embedded Fibers," *Mech. of Materials*, **13**, 131 (1992).

89 R. J. Scheer and J. A. Nairn, "Variational Mechanics Analysis of the Stresses in Microdrop Debond Specimens," *Proc. 8th Int'l Conf. on Comp. Mat.*, 29-C (1991).

90 R. J. Scheer and J. A. Nairn, "Variational Mechanics Analysis of the Stresses and Failure in Microdrop Debond Specimens," *Composites Engineering*, **2**, 641 (1992).

91 G. C. Sih, P. C. Paris, and G. R. Irwin, "On Cracks in Rectilinearly Anisotropic Bodies," *Int'l J. Fract. Mech*, **1**, 189 (1965).

92 J. M. Hedgepeth, "Stress Concentrations in Filamentary Structures," NASA TN D-882, Langley Research Center (1961).

93 J. M. Hedgepeth and P. Van Dyke, "Local Stress Concentrations in Imperfect Filamentary Composite Materials," *J. Comp. Mat.*, 1, 294 (1967).

94 P. Van Dyke and J. M. Hedgepeth, "Stress Concentrations from Single-Filament Failures in Composite Materials," *Textile Res. Journal*, **39**, 618 (1969).

95 W. B. Fichter, "Stress Concentration Around Broken Filaments in A Filament Stiffened Sheet," NASA TN D-5453 (1969).

96 S. V. Kulkarni, B. W. Rosen, and C. Zweben, "Load Concentration Factors for Circular Holes in Composite Laminates," *J. Comp. Mat.*, **7**, 387 (1973).

97 A. C. Eringren and B. S. Kim, "Stress Concentration in Filamentary Composites with Broken Fibers," *Letters in Applied and Engineering Sciences*, **2**, 69 (1974).

98 J. G. Goreeand R. S. Gross, "Stresses in a Three-Dimensional Unidirectional Composite Containing Broken Fibers," *Eng. Fract. Mech.*, **13**, 395 (1979).

99 J. G. Goree and R. S. Gross, "Analysis of a Unidirectional Composite Containing Broken Fibers and Matrix Damage," *Eng. Fract. Mech.*, **13**, 563 (1979).

100 J. M. Wolla and J. G. Goree, "Experimental Evaluation of Longitudinal Splitting in Unidirectional Composites," *J. Comp. Mat.*, **21**, 49 (1987).

101 J. A. Nairn, "Fracture Mechanics of Unidirectional Composites Using the Shear-Lag Model II: Theory," *J. Comp. Mat.*, **22**, 561 (1988).

102 J. A. Nairn, "Fracture Mechanics of Unidirectional Composites Using the Shear-Lag Model II: Experiment," *J. Comp. Mat.*, **22**, 589 (1988).

103 M. A. Wright and F. A. Ianuzzi, "The Application of the Principles of Linear Elastic Fracture Mechanics to Unidirectional Fiber Reinforced Composite Materials," *J. Comp. Mat.*, **7**, 430 (1973).

104 *Plain-Strain Fracture Toughness of Metallic Materials*, ASTM E399-83 (1983).

105 A. R. Wedgewood, K. B. Su, and J. A. Nairn, "Toughness Properties and Service Performance of High Temperature Thermoplastics and their Composites," 19th *Int'l SAMPE Tech. Conf.*, **19**, 4 54 (1987).

106 A. R. Wedgewood and D. C. Grant, "Autoclave Processing of Condensation Polyimide Composites Based on Prepregs of Avimid® K," 34th *Int'l SAMPE Symp. and Exhibition*, **34**, 1 (1989).

107 E. F. Rybicki and M. F. Kanninen, "A Finite Element Calculation of Stress Intensity Factors By a Modified Crack Closure Integral," *Eng. Fract. Mech.*, **9**, 931 (1977).

108 A. S. D. Wang, N. N. Kishore, and W. W. Feng, "On Mixed Mode Fracture in Off-Axis Unidirectional Graphite-Epoxy Composites," *Proc.* 4th *Int'l Conf. on Comp. Mat.*, 559 (1982).

REPORT DOCUMENTATION PAGE	*Form Approved* *OMB No. 0704-0188*

1. AGENCY USE ONLY *(Leave blank)*	2. REPORT DATE November 1992	3. REPORT TYPE AND DATES COVERED Contractor Report

4. TITLE AND SUBTITLE **Microcracking, Microcrack-Induced Delamination, and Longitudinal Splitting of Advanced Composite Structures**	5. FUNDING NUMBERS C NAS1-18833 WU 505-63-50
6. AUTHOR(S) John A. Nairn	
7. PERFORMING ORGANIZATION NAME(S) AND ADDRESS(ES) University of Utah Department of Materials Science and Engineering Salt Lake City, UT 84112	8. PERFORMING ORGANIZATION REPORT NUMBER
9. SPONSORING/MONITORING AGENCY NAME(S) AND ADDRESS(ES) National Aeronautics and Space Administration Langley Research Center Hampton, VA **23681-0001**	10. SPONSORING/MONITORING AGENCY REPORT NUMBER NASA CR-4472

11. SUPPLEMENTARY NOTES

Langley Technical Monitor: John H. Crews, Jr.
Final Report

12a. DISTRIBUTION/AVAILABILITY STATEMENT Unclassified - Unlimited Subject Category 39	12b. DISTRIBUTION CODE

13. ABSTRACT *(Maximum 200 words)*

A combined analytical and experimental study was conducted to analyze microcracking, microcrack-induced delamination, and longitudinal splitting in polymer matrix composites. Strain energy release rates, calculated by a variational analysis, were used in a failure criterion to predict microcracking. Predictions and test results were compared for static, fatigue, and cyclic thermal loading. The longitudinal splitting analysis accounted for the effects of fiber bridging. Test data are analyzed and compared for longitudinal splitting and delamination under mixed-mode loading. This study emphasizes the importance of using fracture mechanics analyses to understand the complex failure processes that govern composite strength and life.

14. SUBJECT TERMS Composite laminates; Fracture mechanics; Matrix cracking; Splitting; Variational analysis	15. NUMBER OF PAGES 164
	16. PRICE CODE A08

17. SECURITY CLASSIFICATION OF REPORT Unclassified	18 SECURITY CLASSIFICATION OF THIS PAGE **Unclassified**	19. SECURITY CLASSIFICATION OF ABSTRACT	20. LIMITATION OF ABSTRACT

NSN 7540-01-280-5500

Standard Form 298 (Rev 2-89)
Prescribed by ANSI Std Z39-18
298-102

NASA-Langley, 1992

National Aeronautics and
Space Administration
Code JTT
Washington, D.C.
20546-0001
Official Business
Penalty for Private Use, $300